

Gas Kinematics in the Haloes of Nearby Irregular Dwarf Galaxies



Dissertation

zur
Erlangung des Grades
„Doktor der Naturwissenschaften“
in der Fakultät für Physik und Astronomie
der Ruhr-Universität Bochum

von
Janine van Eymeren
aus
Essen

Bochum 2008

1. Gutachter: Prof. Dr. Ralf-Jürgen Dettmar (AIRUB)
2. Gutachter: Priv. Doz. Dr. Dominik J. Bomans (AIRUB)
3. Gutachter: Dr. Bärbel Koribalski (ATNF)

Tag der Disputation: 30.06.2008



To

my godfather († 11.01.2008)

and

my grandmother († 21.01.2008)

Contents

1	Introduction	1
1.1	Motivation	1
1.2	The sample	4
1.3	Organisation of the thesis	5
2	Fabry-Perot Interferometry	7
2.1	Multiple-beam interference	7
2.1.1	Interference at plane-parallel plates	7
2.1.2	Finesse, peak transmission and the contrast factor	10
2.1.3	Resolution and the free spectral range	10
2.1.4	The FP etalon as a wavelength filter	11
2.2	A scanning Fabry-Perot interferometer	11
2.3	The detector	12
2.3.1	Photon-counting systems vs. CCDs	12
2.3.2	An overview over the Image Photon Counting System	12
2.4	Observations and data reduction	13
2.5	Technical issues of the observations and the data reduction	16
3	Spiral structure in NGC 2366	19
3.1	Introduction	19
3.2	Observations and data reduction	20
3.2.1	Optical imaging	20
3.2.2	Fabry-Perot interferometry	20
3.3	Results	22
3.3.1	General morphology	22
3.3.2	H α velocities	22
3.4	Discussion of the peculiarities in NGC 2366	22
3.4.1	The GALEX view	22
3.4.2	HI ring	23
3.4.3	Satellite galaxy to the west	24
3.4.4	Properties of (dwarf) spirals	24
3.5	Conclusions	24
4	A comparison of the gas kinematics in NGC 2366	27
4.1	Introduction	27
4.2	Observations and data reduction	29
4.2.1	Optical imaging	29

4.2.2	The Fabry-Perot data	30
4.2.3	The H I data	30
4.3	General morphology	30
4.4	Kinematic analysis	32
4.4.1	The H α velocity field	33
4.4.2	The H I velocity field	35
4.4.3	A comparison of the neutral and ionised gas	37
4.5	Discussion	40
4.5.1	The outflows	41
4.5.2	Supperbubble blowout in NGC 2366?	41
4.5.3	Spiral arm structure revisited	42
4.5.4	Outflow or galactic wind?	42
4.6	Summary	43
4.A	Appendix: H α image and extension of the catalogue of ionised gas structures	44
5	A comparison of the gas kinematics in NGC 4861	45
5.1	Introduction	45
5.2	Observations and data reduction	46
5.2.1	The Fabry-Perot data	46
5.2.2	Optical imaging	47
5.2.3	The H I data	48
5.3	General morphology	48
5.4	Kinematic analysis	51
5.4.1	H α velocity field	51
5.4.2	H I velocity field	52
5.5	Discussion	54
5.5.1	Comparison of the neutral and ionised gas	54
5.5.2	Outflow or galactic wind?	57
5.5.3	Comparison with NGC 2366	58
5.5.4	H I cloud to the east	58
5.6	Summary	60
5.A	Appendix: H α image and extension of the catalogue of ionised gas structures	61
6	The Local Volume HI Survey: Gas kinematics in IC 4662 and NGC 5408	63
6.1	Introduction	63
6.2	Observations and Data Reduction	64
6.2.1	ATCA radio data	64
6.2.2	Optical data	66
6.3	General morphology	69
6.3.1	IC 4661	70
6.3.2	NGC 5408	70
6.3.3	Star Formation rates	71
6.4	Kinematic analysis	74
6.4.1	The kinematics of the neutral gas – the H I velocity fields	74
6.4.2	The kinematics of the neutral gas – the H I rotation curves	74
6.4.3	The kinematics of the ionised gas – long-slit spectroscopy of the H α line	77
6.4.4	A comparison of the H I with the H α kinematics	80

6.5	Outflow or galactic wind?	82
6.6	Summary	83
6.A	Appendix: $H\alpha$	84
7	Dark matter in dwarf galaxies	87
7.1	Introduction	87
7.2	The data	88
7.3	Rotation curves	89
7.3.1	H I rotation curves	89
7.3.2	$H\alpha$ rotation curves	89
7.4	Mass models	93
7.4.1	Dynamical components	93
7.4.2	Dark matter halo models	93
7.4.3	Fitting process	94
7.5	Discussion	96
7.5.1	NGC 2366	96
7.5.2	NGC 4861	98
7.5.3	IC 4662	99
7.5.4	NGC 5408	99
7.6	Summary	99
8	Summary and Outlook	101
8.1	Summary	101
8.1.1	Outflows of neutral and ionised gas in dwarf galaxies	102
8.1.2	The cusp-core discrepancy	103
8.1.3	H I cloud in NGC 4861 – did we find a dark galaxy?	103
8.2	Outlook	104
A	The Gaussian decomposition	105
B	Adaptive filtering	109
C	Deriving the rotation curves	111
C.1	H I rotation curves	111
C.2	$H\alpha$ rotation curves	112
	Bibliography	115

List of Figures

1.1	The chimney model by Norman & Ikeuchi (1989).	3
1.2	Superbubble model by Mac Low & Ferrara (1999).	3
2.1	The Fabry-Perot etalon.	8
2.2	The transmission function I_t/I_i of a Fabry-Perot etalon.	9
2.3	Typical fringe patterns of monochromatic light sources.	10
2.4	Schematic view of an IPCS (Gach et al. 2002).	13
2.5	The FP interferometer attached to the 1.93 m telescope at the OHP.	14
2.6	The most important steps of the Fabry-Perot data reduction.	15
2.7	Schematic representation of the FP's scanning process.	16
2.8	Artefacts on the H α velocity field of NGC 2366.	17
3.1	<i>R</i> -band image and continuum-subtracted H α image of NGC 2366.	21
3.2	The H α velocity field of NGC 2366.	21
3.3	The GALEX FUV contours overlaid onto the continuum-subtracted H α image.	23
3.4	Statistical properties of dwarf spirals.	23
4.1	<i>R</i> -band image and continuum-subtracted H α image of NGC 2366.	29
4.2	H I channel maps of NGC 2366 (contours) superposed on the <i>R</i> -band image.	31
4.3	The H I moment maps of NGC 2366.	33
4.4	A comparison of the H α and H I morphology.	34
4.5	The H α velocity field of NGC 2366.	35
4.6	The H I kinematics of NGC 2366.	37
4.7	A comparison of the neutral and ionised gas.	38
4.8	Gaussian decomposition of the H I.	39
4.9	Some example H I line profiles.	39
4.10	An enlargement of the central region of NGC 2366.	40
4.11	A comparison of the escape and expansion velocities.	43
4.12	Continuum-subtracted H α image of NGC 2366.	44
5.1	<i>R</i> -band and H α image of NGC 4861.	47
5.2	H I channel maps of NGC 4861 (contours) superposed on the <i>R</i> -band image.	49
5.3	The H I moment maps of NGC 4861.	50
5.4	A comparison of the H α and the H I morphology.	51
5.5	The H α velocity field of NGC 4861.	52
5.6	The H I rotation curve of NGC 4861.	54
5.7	A comparison of the neutral and ionised gas.	55
5.8	Gaussian decomposition of the H I.	56
5.9	Some example H I line profiles.	56

5.10	A comparison of the escape and expansion velocities.	58
5.11	Deep R -band and V -band images of the surroundings of NGC 4861.	59
5.12	A kinematic study of the H I cloud NGC 4861 B.	60
5.13	Baryonic Tully-Fisher relation.	61
5.14	Continuum-subtracted $H\alpha$ image of NGC 4861.	62
6.1	H I channel maps of IC 4662 (contours) superposed on our R -band image.	67
6.2	H I channel maps of NGC 5408 (contours) superposed on the R -band image.	68
6.3	R -band images of IC 4662 and NGC 5408.	69
6.4	H I moment maps of IC 4662.	71
6.5	$H\alpha$ images of IC 4662 and NGC 5408 with H I contours overlaid.	72
6.6	Continuum-subtracted $H\alpha$ images of IC 4662 and NGC 5408.	72
6.7	H I moment maps of NGC 5408.	73
6.8	The kinematics of IC 4662.	76
6.9	The kinematics of NGC 5408.	77
6.10	Example spectra of IC 4662 and NGC 5408.	78
6.11	Pv diagrams of IC 4662.	79
6.12	Pv diagrams of NGC 5408.	80
6.13	Gaussian decomposition of the H I in IC 4662.	81
6.14	Gaussian decomposition of the H I in NGC 5408.	81
6.15	Outflow or galactic wind?	83
6.16	Continuum-subtracted $H\alpha$ images of IC 4662 and NGC 5408.	85
7.1	A comparison of the H I and the $H\alpha$ rotation curve.	90
7.2	A comparison of the H I and the $H\alpha$ rotation curve.	90
7.3	A comparison of the H I and the $H\alpha$ rotation curve.	91
7.4	Mass decomposition of NGC 2366.	96
7.5	Mass decomposition of NGC 4861.	97
7.6	Mass decomposition of IC 4662.	97
7.7	Mass decomposition of NGC 5408.	98
A.1	The interface of the Gaussian fitting routine <i>splot</i>	107
B.1	The adaptive filter technique in practice.	110
C.1	Deriving the rotation curve of NGC 5408: The iterative approach.	113
C.2	Deriving the rotation curve of NGC 5408: The free approach.	114
C.3	The resulting H I rotation curves of NGC 5408.	114

List of Tables

1.1	The phases of the interstellar medium.	4
1.2	The basic parameters of the galaxy sample.	5
4.1	The basic parameters of NGC 2366.	29
4.2	H I properties measured from the THINGS data.	36
4.3	The most prominent structures and their sizes in NGC 2366 – an extension –.	44
5.1	The VLA H I observations.	48
5.2	H I properties as measured from the VLA data.	53
5.3	The most prominent structures and their sizes in NGC 4861 – an extension –.	61
6.1	The basic properties of IC 4662 and NGC 5408.	65
6.2	ATCA radio observations.	65
6.3	Imaging – Some observational parameters.	66
6.4	Long-slit spectroscopy – some details.	70
6.5	Star formation rates from FIR and 20 cm radio continuum measurements.	73
6.6	ATCA H I properties.	75
7.1	The main observational parameters.	89
7.2	Parameters for the exponential disk fitting.	95
7.3	The basic parameters of the mass decomposition.	100
C.1	NGC 5408: Parameter sets for the three different approaches.	113

Introduction

1.1 Motivation

The gravity of the baryonic matter is not sufficient to explain the observed structures in and the evolution of the Universe. Therefore, cosmological models predict the existence of an additional, collisionless matter, the so-called Cold Dark Matter (CDM). A first indication for large amounts of unseen matter was given by Oort (1932) who studied vertical motions of stars in the solar neighbourhood and derived a surface density which was about two times higher than expected from the visible matter. This discovery was heavily disputed in later years (e.g., Bienayme et al. 1987) and only little evidence seems to be left for the existence of large amounts of dark matter in the Milky Way. However, studies by, e.g., Zwicky (1933, 1937) of the velocity dispersions of galaxies in clusters and their conclusion that the clusters contain up to two orders of magnitude more mass than visible were confirmed many times (e.g., Rood et al. 1972; Łokas & Mamon 2003). In recent years, it has become clear that dark matter dominates the mass budget of the Universe also on cosmological scales.

Although it is now widely accepted that dark matter exists and is strongly influencing the structure and evolution of the Universe, little is known about its nature, yet. CDM simulations have been very successful in describing the observed large- and intermediate-scale structures, but less successful on galactic scales. One of the most important contradictions is the cusp-core problem. Numerical simulations of CDM haloes predict a cuspy density slope in the inner few kpc (Navarro et al. 1996), whereas observations of dark matter dominated low surface brightness and dwarf galaxies show a density profile with a flat core (e.g., de Blok & Bosma 2002). Another discrepancy is the missing satellite problem. CDM simulations predict an excess of small satellite galaxies around more massive objects like the Milky Way, which is higher by a factor of 10 or even more than observed (Moore et al. 1999).

Furthermore, an excess of hot gas in the cores of galaxy clusters is detected (Ponman et al. 1999), which is also inconsistent with cosmological models. It is widely believed that the structure in the Universe evolves hierarchically, which means that primordial density fluctuations supported by gravity collapse and merge to form progressively larger systems. However, X-ray clusters do not show the predicted relations between luminosity, temperature and redshift. The entropy near the centre of the clusters is higher than achievable through gravitational collapse alone. A possible solution is the “pre-heated intracluster medium” (ICM) model, where the entropy is raised by supernovae explosions from the forming galaxies, which pollute the ICM with metals prior to the cluster collapse (Kaiser 1991). Therefore, stellar feedback on the interstellar medium (ISM) and – depending on the gravitational

potential well of the galaxies – on the intergalactic medium (IGM) is one of the most important processes in the evolution of galaxies, galaxy clusters and the Universe.

Altogether, the ISM consists of eight phases, which are the Molecular Medium (MM), the Cold Neutral Medium (CNM), the Warm Neutral Medium (WNM), the Diffuse Ionised Gas (DIG), the Hot Ionised Gas (HIM), dust grains, cosmic rays and magnetic fields (see Table 1.1, Dettmar 1992). Massive stars transfer energy and momentum into the ISM by stellar winds and supernovae (SN) explosions. The ambient gas is shock-heated and accelerated, which leads to the formation of bubbles or shell-like structures detectable on optical emission line images. At distinct points along the disk, a superbubble blowout can happen where the shells fragment (due to Rayleigh-Taylor instabilities) and the hot gas is transported through tunnel-like features into the halo (Fig. 1.1, Norman & Ikeuchi 1989). On its way into the halo and in the halo itself, the hot gas radiatively cools down and eventually falls back onto the disk as cool clouds. This is the well-known *Galactic Fountain* scenario (Shapiro & Field 1976), which might explain the high-velocity clouds in the halo of the Milky Way as former outflows of hot gas. In some cases, the gas has enough energy to escape from the gravitational potential of the host galaxy and to enrich the IGM by forming a freely flowing galactic wind. Especially dwarf galaxies are important laboratories to study superbubble “blow-away” as their low escape velocities facilitate the removal of the gas (Mac Low & Ferrara 1999). However, the simulations by Mac Low & Ferrara (1999) show that the fraction of the gas which is really lost in an outflow is low and depends on the galaxy mass and the energy input. In Fig. 1.2, the state of expansion after 50 Myr is displayed. The total galaxy mass and the energy input vary, the metallicity is fixed. A superbubble blowout, which would increase the probability of a blow-away, only occurred in galaxies of lower mass and/or higher energy input, Mac Low & Ferrara (1999) also modelled the state of expansion after 75, 100, and 200 Myr (their Figs. 2b-d). Although the superbubble is more evolved, blow-away of hot gas is still unlikely and only possible in galaxies of lower mass and with high kinetic luminosities. However, metal-enriched material from stellar winds and SN ejecta is more easily accelerated to velocities beyond the escape velocity of the host galaxy than the ambient gas. Thus, the fraction of blown away metals rises, in case of galaxy masses of $10^6 - 10^7 M_{\odot}$ even to unity. The reason for this is that the metals produced by the massive stars remain within the hot, shocked cavity gas, which has a high sound speed, and can therefore easily escape the galaxy. It is much more difficult to accelerate the dense, cool shells of the swept-up ambient gas so that usually, the gas stays gravitationally bound. Nevertheless, the existence of fragmented cool shell structures close to the disk as visible on optical images also indicates the existence of hot gas that left these shells behind during the blowout process (Mac Low & Ferrara 1999). Considering that the hot gas expands into the surrounding neutral gas means that these ionised gas filaments can also be explained by turbulent mixing between the hot and the neutral gas (Slavin et al. 1993).

In this thesis, two components of the ISM are examined, which are the WNM with H I emission as a tracer and the DIG with H α emission as a tracer. In order to understand the properties of superbubble blowout, the behaviour of all phases in the ISM have to be studied and to be compared. According to Mac Low & Ferrara (1999), it is the hot gas that has the highest probability to escape from the gravitational potential of a galaxy. However, as mentioned above, the ionised gas can be used as a tracer for the hot gas. Additionally, the densities of the DIG are a factor of 100 higher than the densities of the HIM so that it is easier to trace outflowing gas by looking at H α . And last but not least the performance of optical observations is much more developed. The neutral gas is first used as a reference for the true kinematics of the galaxy. Additionally, its kinematics are examined which also includes a search for outflowing structures.

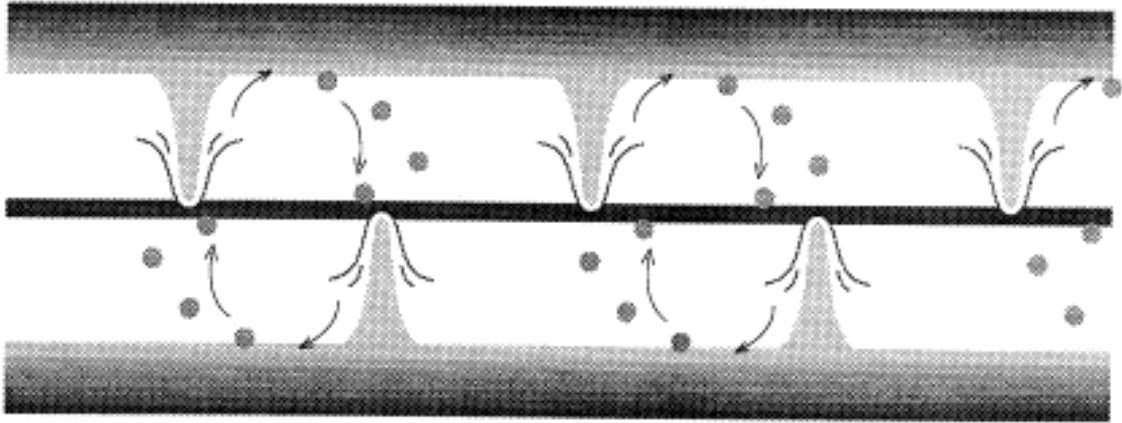


FIG. 1.1: The chimney model by Norman & Ikeuchi (1989). At distinct point along the disk, hot gas is transported into the halo, cools down and eventually falls back onto the disk.

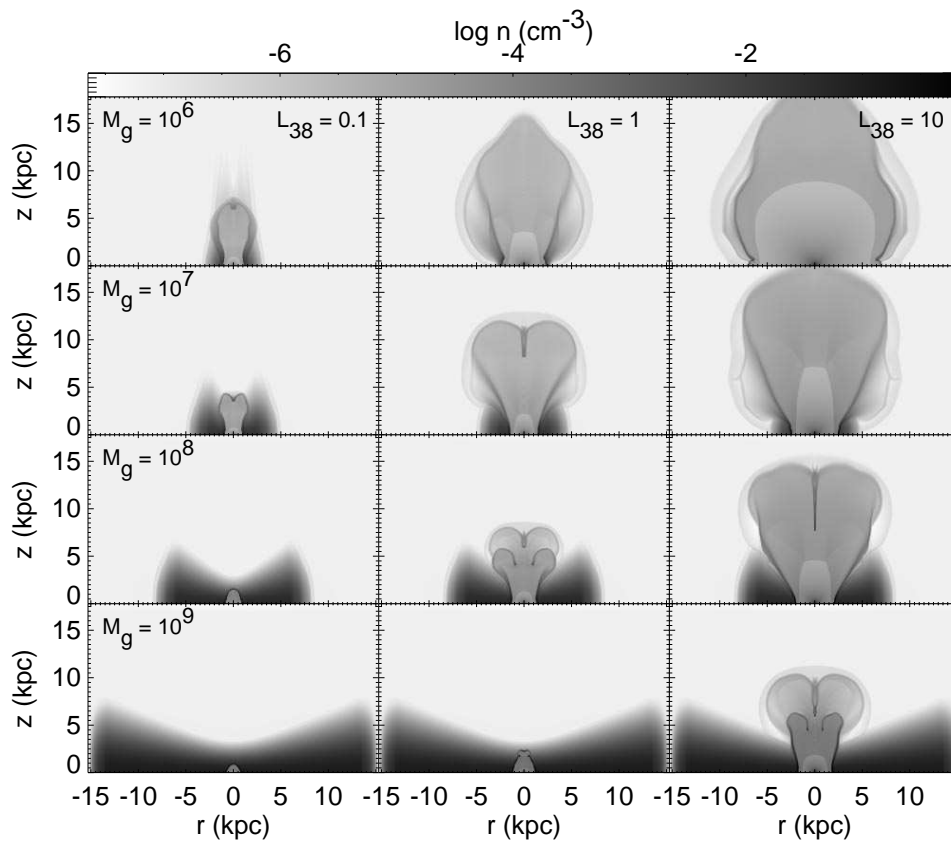


FIG. 1.2: Superbubble model by Mac Low & Ferrara (1999). The state of expansion after 50 Myr is shown for different galaxy masses and energy inputs and a constant metallicity. Only in case of a low galaxy mass and/or a high energy input a blowout has already occurred, which increases the probability of a blow-away.

TABLE 1.1: The phases of the interstellar medium.

	MM	CNM	WNM	DIG	HIM
T [K]	20	135	6000	8000	5×10^5
n [cm^{-3}]	$10^2 - 10^5$	20	0.5	0.4	6×10^{-3}

1.2 The sample

As dwarf galaxies harbour regions of strong star formation and generally have a lower gravitational potential, they have a higher probability to show galactic winds. Therefore, the sample presented in this thesis consists of four nearby (up to a distance of 10 Mpc) irregular dwarfs, which are all classified as barred Magellanic-type galaxies. Two of them (NGC 2366 and NGC 4861) have already been studied before by performing high-resolution long-slit echelle spectroscopy (van Eymeren et al. 2007). Several outflows have been found and their expansion velocities have been compared with the escape velocities of the galaxies. In all cases the expansion velocities were lower than the escape velocities ruling out a possible galactic wind. However, it has to be noted that only bright filaments close to the main star forming regions were detected on the echelle spectra due to missing sensitivity.

The very distant and faint structures are more promising as they are already far away from ionising stars, but still ionised, and the influence of the gravitational potential is already lower at this distance from the dynamical centre. In order to measure the expansion velocities of these distinct low surface brightness filaments and to describe their morphology, Fabry-Perot interferometry was performed. The field of view was large enough to assure a full spatial coverage of both galaxies in comparison to the few long-slit spectra analysed so far. Similar to NGC 2366 and NGC 4861, IC 4662 and NGC 5408 were chosen because deep $\text{H}\alpha$ images also show faint kpc-scale filaments. They were observed by performing deep medium-resolution long-slit spectroscopy to detect even the faintest structures. For all galaxies, HI synthesis data were used as well as 20 cm radio continuum data for IC 4662 and NGC 5408. The main properties of the galaxies are given in Table 1.2.

- **NGC 2366:** The distance of NGC 2366 and its position on the sky place this galaxy into the M 81 group. Nevertheless, it can be regarded as an isolated galaxy. Its appearance in $\text{H}\alpha$ is dominated by the Giant Extragalactic H II region (GEHR) NGC 2363 in the south-western end of the galaxy. This GEHR harbours two large OB associations, one in the core with an age of 1 Myr and one in the eastern part of the core with an age of 3-5 Myr (Drissen et al. 2001).
- **NGC 4861:** NGC 4861 is very similar to NGC 2366 concerning its optical shape. It is also dominated by a GEHR in the south-west, I Zw 49, where most of the star formation occurs. A chain of small H II regions extends to the north-east. Although the galaxy shows almost no evidence for the existence of spiral structures (Wilcots et al. 1996), it is classified as SB(s)m. Its distance is more than twice the distance of NGC 2366 (see Table 1.2). HI data reveal the existence of an HI cloud at a deprojected distance of 4 kpc east of the main body, which appears to have no optical counterpart (Wilcots et al. 1996; Thuan et al. 2004).
- **NGC 5408:** NGC 5408 was first studied in 1972 by Bohuski et al. (1972). Its nucleus consists of several bright H II regions and appears to be undergoing a violent burst of star formation (Bohuski et al. 1972). Since then it was observed many times as it harbours an ultra-luminous

TABLE 1.2: The basic parameters of the galaxy sample.

Object	α (J2000)	δ (J2000)	Hubble Type (1)	m_B [mag] (2)	D [Mpc] (3)	v_{sys} [km s ⁻¹] (4)
NGC 2366	07 ^h 28 ^m 54.6 ^s	+69° 12' 57''	IB(s)m	-16.63	3.44	97
NGC 4861	12 ^h 59 ^m 02.3 ^s	+34° 51' 34''	SB(s)m	-16.62	7.5	835
NGC 5408	14 ^h 03 ^m 20.9 ^s	-41° 22' 40''	IB(s)m	-15.84	4.81	502
IC 4662	17 ^h 47 ^m 08.8 ^s	-64° 38' 30''	IBm	-14.84	2.44	310

References: Column (1): de Vaucouleurs et al. (1991). Column (2): NGC 2366 and NGC 4861: Bomans (2001), NGC 5408 and IC 4662: Lauberts & Valentijn (1989). Column (3): NGC 2366: Tolstoy et al. (1995), NGC 4861: de Vaucouleurs et al. (1991), NGC 5408: Karachentsev et al. (2002), IC 4662: Karachentsev et al. (2006). Column (4): Systemic velocities derived in this thesis.

X-ray source very close to the concentration of H II regions. Its distance of $D_{\text{TRGB}} = 4.81$ Mpc was obtained by Karachentsev et al. (2002). Its position on the sky puts NGC 5408 in the Centaurus A group, but its distance differs from the medium value of Cen A members by more than 1 Mpc.

- **IC 4662:** The distance of IC 4662 of $D_{\text{TRGB}} = 2.44$ Mpc was obtained by Karachentsev et al. (2006) and makes it therefore to be the nearest known representative of blue compact dwarfs (Karachentsev et al. 2006). It seems to be a rather isolated galaxy, belonging to no known groups. de Vaucouleurs (1975) describes IC 4662 as a foreground galaxy in the direction of the NGC 6300 group. Its appearance in H α is dominated by bright compact H II regions, but it additionally shows a complex web of filamentary structure in the eastern part. An interesting feature is a cluster of stars with associated H α emission that appears to be detached from the main body of the galaxy. It is located 1.5 or 1.1 kpc to the south-east of the centre. Whether this is a small companion galaxy or an unusually placed OB association is not clear, yet. Hidalgo-Gómez et al. (2001) point out that this H II region differs significantly from the main galaxy in oxygen abundance.

1.3 Organisation of the thesis

This thesis is organised as follows: This introduction is followed by a chapter including information about the basic principles of multi-beam interference, about the Fabry-Perot observations and the data reduction process, and about technical issues which came up during the work with the Fabry-Perot data. Chapter 3 describes the detection of spiral arm structure in NGC 2366, which was a result of the analysis of the Fabry-Perot data, but is not directly connected to the aim of this thesis. This will be followed by the three main chapters, Chaps. 4 to 6, in which the morphology and the kinematics of the ionised and neutral hydrogen in the four sample galaxies are compared. Chapter 7 is an extension of the kinematic analysis to the cusp-core discrepancy described above. For all galaxies, mass models are derived and the results are compared for the two most common haloes, the NFW halo and the pseudo-isothermal halo. Last, but not least a summary and an outlook can be found in Chapter 8.

Fabry-Perot Interferometry

Abstract

Performing long-slit spectroscopy, the field of view is always limited by the slit size, which has the consequence that especially nearby extended objects have to be observed more than once in order to get a full spatial coverage. Therefore, the demand for an observational method combining a sufficient spatial coverage with a certain spectral coverage was rising. Fabry-Perot interferometry is the oldest technique which allows the exposure of a 3-dimensional image within a reasonable time. Its invention dates back to the end of the 19th century and the first reported use of a scanning Fabry-Perot was in 1914. Since two decades, the so-called 3d spectroscopy using new instruments and techniques is getting more and more popular.

In this chapter, the basic principles of multiple-beam interference are explained as well as the observations and the data handling, including a description of old and new problems that had to be faced.

2.1 Multiple-beam interference

When a beam of light is incident on a transparent plate, there are multiple reflections at the plate surfaces, with the result that a series of beams of diminishing amplitude emerges on each side of the plate. In the following, the interference effects that are produced by such plates are discussed, based on the book “Principles of optics” by Born & Wolf (2000).

2.1.1 Interference at plane-parallel plates

Figure 2.1 shows two highly-reflective plane-parallel glass plates which are spaced by a distance l and filled with gas of a refraction index n . The spacing between the two glass plates can, e.g., electrically be varied by applying a precise voltage on piezoelectrics. This form of an interferometer is called Fabry-Perot (FP) etalon.

When monochromatic light is shining on the etalon, the transmitted and reflected intensity can be calculated. For each member of either the reflected or the transmitted set of waves, the variable

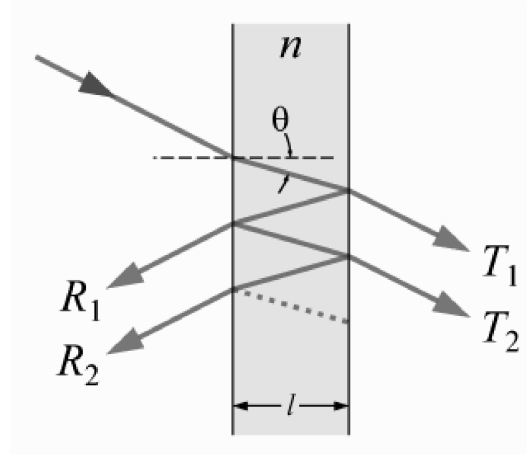


FIG. 2.1: The Fabry-Perot etalon. Two highly reflective, flat glass plates are spaced by a distance l and filled with a gas of a refractive index n . The spacing between the two glass plates can be varied in order to scan the desired wavelength range.

part of the phase of the wave function differs from that of the preceding member by an amount which corresponds to a double traversal of the plate. This phase difference is given by

$$\delta = \frac{4\pi}{\lambda_0} n l \cos \theta \quad (2.1)$$

where λ_0 is the wavelength in vacuum and θ the refraction angle in the gas. For a wave travelling from the surrounding medium into the etalon, r is defined as the reflection coefficient (ratio of reflected and incident amplitudes), and t as the transmission coefficient (ratio of transmitted and incident amplitudes). r' and t' are the corresponding coefficients for a wave travelling from the plate to the surrounding medium. This leads to

$$r = -r'; r^2 = r'^2 = R; tt' = T; R + T = 1 \quad (2.2)$$

The absorption of the etalon material should be negligible.

The reflective amplitude is calculated by summing up all reflected waves. Different waves m differ in phase due to the optical path difference $2mdn$ and in amplitude due to reflection and transmission by $tt' r'^{2m-1}$. The first reflected wave has to be treated with care as here the reflectance for the out-in direction $-r$ has to be used. Putting all this together, the reflected amplitude is

$$A_r = A_i r + A_i \exp(jk2dn) tt' r' \sum_{m=0}^{\infty} r'^{2m} \exp(jk2mdn) \quad (2.3)$$

$$= A_i r - A_i \exp(j\delta) T r \sum_{m=0}^{\infty} (R \exp(j\delta))^m, \delta = 2kdn \quad (2.4)$$

$$= A_i r - A_i \exp(j\delta) T r \frac{1}{1 - R \exp(j\delta)} \quad (2.5)$$

$$= A_i r \frac{1 - R \exp(j\delta) - T \exp(j\delta)}{1 - R \exp(j\delta)} = A_i r \frac{1 - \exp(j\delta)}{1 - R \exp(j\delta)} \quad (2.6)$$

With the intensity of the incident light

$$I_r = A_r \times A_r^* \quad (2.7)$$

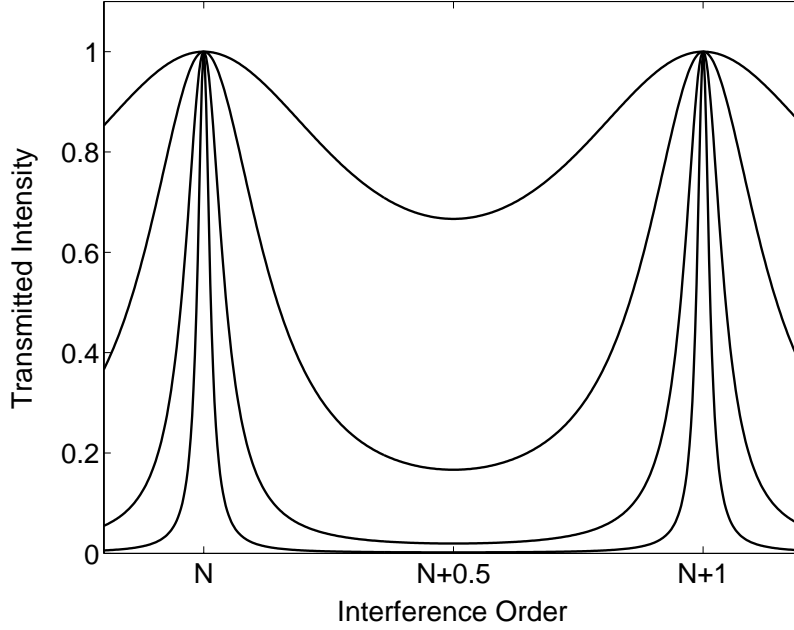


FIG. 2.2: The transmission function I_t/I_i of a Fabry-Perot etalon for different reflectivities (R of 0.1, 0.42, 0.75 and 0.91) as a function of interference order. With increasing reflectivity the intensity maxima become narrower and the suppression of the light throughput between the maxima rises.

this leads to

$$\frac{I_r}{I_i} = \frac{2R(1 - \cos \delta)}{1 - 2R \cos \delta + R^2} = \frac{4R \sin^2 \frac{\delta}{2}}{(1 - R)^2 + 4R \sin^2 \frac{\delta}{2}} \quad (2.8)$$

The transmitted light is given by

$$A_t = A_i t t' \sum_{m=0}^{\infty} r'^{2m} \exp(jk2mdn) \quad (2.9)$$

$$= A_i T \sum_{m=0}^{\infty} R^m \exp(j\delta) \quad (2.10)$$

$$= A_i \frac{T}{1 + R \exp(j\delta)} \quad (2.11)$$

and

$$\frac{I_t}{I_i} = \frac{T^2}{1 - 2R \cos \delta + R^2} = \frac{T^2}{(1 - R)^2 + 4R \sin^2 \frac{\delta}{2}} \quad (2.12)$$

Eqs. 2.8 and 2.12 are known as Airy's formulae.

Figure 2.2 shows the ratio of transmitted and incident intensities – the transmission – function, for different reflectivities as a function of interference order. The two characteristic properties for each of the transmission functions are the width of the maxima and the suppression of light throughput between the maxima, which are described in the following subsection.

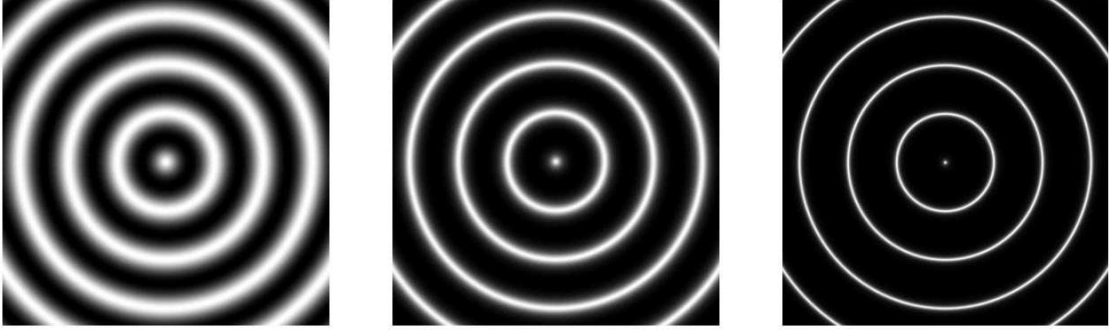


FIG. 2.3: Typical fringe patterns of monochromatic light sources with a finesse of 1, 10, and 100 (from the left to the right).

2.1.2 Finesse, peak transmission and the contrast factor

The pattern of the transmitted light consists of narrow bright fringes on an almost completely dark background (see Fig. 2.3). If R is increased, the intensity of the minima of the transmitted pattern falls and the maxima become sharper until, when R approaches unity, the intensity of the transmitted light is small except in the immediate neighbourhood of those maxima. This sharpness of the intensity maxima can be measured by their half-intensity width, usually called half-width, which is the width between the points on either side of the maximum where the intensity has fallen to half its maximum value. The finesse F is now defined as the ratio of the separation of the fringes L and the half-width l

$$F = \frac{L}{l} \quad (2.13)$$

The other two important characteristics of a FP are the peak transmission given by

$$\tau = \left(\frac{I_t}{I_i} \right)_{max} \quad (2.14)$$

and the contrast factor given by

$$C = \left(\frac{I_t}{I_i} \right)_{max} / \left(\frac{I_t}{I_i} \right)_{min} \quad (2.15)$$

Typically, the plate coatings are either metal films (silver, aluminium) or dielectric films (alternate layers of an optical thickness of $\lambda_0/4$). R increases with increasing thickness of the metal film or increasing number of layers in case of the dielectric films. At high values of R , which are desired as mentioned above, and therefore a high finesse, the fraction of the absorbed light increases. This, however, means that the peak transmission decreases – the contrast factor is proportional to the finesse – and that in practise a compromise between both parameter values has to be found.

2.1.3 Resolution and the free spectral range

So far, the infall of a single monochromatic wave has been assumed. In case of two monochromatic components of similar intensity and gradually increased wavelength difference, two mutually displaced sets of maxima in the interference pattern are expected. The resolving power $\lambda_0/\Delta\lambda_0$ is the measure for two wavelengths at $\lambda_0 \pm \frac{1}{2}\Delta\lambda_0$ that are just resolved. Rayleigh was the first to define a

resolution criterion which says that two components of equal intensity are just resolved when the principal intensity maximum of one component coincides with the first intensity minimum of the other. The relationship between the resolving power and the above mentioned finesse is given by

$$\frac{\lambda_0}{\Delta\lambda_0} \sim \frac{2Fnl}{\lambda_0} \quad (2.16)$$

This equation shows that the resolution of a FP plate can be increased by increasing nl , the optical path difference between the two reflective surfaces. This also leads to an increase of the interference order, which means more problems with overlapping orders. As a measure for a useful working range without overlapping orders, the free spectral range is defined. It is inversely proportional to the order and given by

$$\frac{\Delta\lambda_0}{\lambda} = \frac{1}{m} \quad (2.17)$$

The FP that was used for obtaining the data analysed in this thesis was centred on the $H\alpha$ line at an interference order of 798. Following Eq. 2.17, this leads to a free spectral range of 376 km s^{-1} . The finesse is 12, the FP therefore scanned through 24 steps (Shannon sampling theorem) leading to a velocity sampling of 15 km s^{-1} . According to Fig. 7.61 in Born & Wolf (2000), a finesse of 12 at $H\alpha$ gives a high peak transmission of about 0.7.

2.1.4 The FP etalon as a wavelength filter

Remembering the transmitted fringe pattern, the intensity at wavelengths on either side of the interference maxima falls sharply to low values. This implies that the FP etalon is working as a wavelength filter with multiple transmission bands. If the optical thickness of the etalon is only a few half-wavelengths of the visible light, the transmission bands are of low order and widely separated in wavelength. Thus, it is possible to suppress the light in all bands but the desired one, which can, e.g., be done with interference filters. For the below described observations an interference filter with a typical width of 1.5 to 2 nm was used to pre-select the $H\alpha$ line by taking into account the red-shift of the galaxies.

2.2 A scanning Fabry-Perot interferometer

The observations were performed with a scanning FP interferometer. As described above, the wavelength range was pre-selected by an interference filter. By changing the spacing between the two glass plates of the etalon, the interferometer was scanned through all 24 channels while every channel was observed for ten seconds. Having scanned the whole wavelength range, a cycle was finished and the scanning sequence was repeated. A total exposure time of, e.g., 4 hours therefore means that the exposure time of each channel is only a $1/24$, i.e., 10 min. Additionally, it becomes obvious that this method is not simultaneously producing a 3d data set. A complete spatial coverage is given in every exposure, but to obtain the whole wavelength range, 24 exposures have to be taken. The advantage of this rapid scanning is that the whole wavelength range is observed under the same conditions, which are, e.g., the weather conditions (seeing) or the airmass of the object. As the data are stored in separate files, bad data can easily be removed.

2.3 The detector

Because of the short integration times, CCDs are not the appropriate detectors for a scanning FP. Therefore, an Image Photon Counting System (IPCS) was used.

2.3.1 Photon-counting systems vs. CCDs

CCDs have very high quantum efficiencies up to 95% and a very low readout noise down to 2 to 3 electrons. Nevertheless, the maximal signal to noise ratio (S/N) that can be achieved by an ideal CCD is described by

$$S/N = \frac{N}{\sqrt{N + \sigma^2 + T}} \quad (2.18)$$

where N is the number of photons collected per pixel during the exposure time, σ is the reading noise of the CCD in electrons, and T the thermal noise in electrons/pixels. In newer CCDs or IPCSs the contribution of the thermal noise is negligible. However, other effects constrain the usage of a CCD like, e.g., cosmic rays in long-term exposures, which means that a long exposure has to be split into several shorter exposures. This changes Eq. 2.18 to

$$S/N = \frac{N}{\sqrt{N + n\sigma^2 + T}} \quad (2.19)$$

with n being the number of exposures. When N is small and n gets larger, the S/N decreases significantly as it is the case in scanning instruments like the FP. Therefore, CCDs were replaced by an IPCS which has a S/N of

$$S/N = \frac{N}{\sqrt{N + T}} \sim \sqrt{N} \quad (2.20)$$

This means that these systems do not have any reading noise and are less affected by cosmic rays because one event is seen as one photon only. Although the quantum efficiency is lower than in CCDs, they are more appropriate for multiplex systems like the FP.

For a multiplex system, the S/N is defined as the quadratic sum of the S/N s of each channel as there is no noise correlation between the channels. This leads to

$$S/N_m = \sqrt{n \left(\frac{N/n}{\sqrt{N/n + \sigma^2}} \right)^2} = \frac{N}{\sqrt{N + n\sigma^2}} \quad (2.21)$$

where N is the number of photons expected during the whole exposure, n the number of channels, and σ the readout noise of the CCD. Usually, the emission appears only in a few channels, which can be different ones for different pixels depending on the gas structures. In the worst case, the emission is only detected in two channels, which lowers the ideal S/N_m to

$$S/N_m = \sqrt{2 \left(\frac{N/n}{\sqrt{N/n + \sigma^2}} \right)^2} = \frac{2N/n}{\sqrt{2N/n + n\sigma^2}} \quad (2.22)$$

2.3.2 An overview over the Image Photon Counting System

Figure 2.4 shows a schematic view of an IPCS. The camera head is composed of a GaAs proximity-focused two-stage microchannel plate image-intensifier tube, fibre-coupled to a CCD. The cathode is cooled down to -25°C . Each photon interacting with the photocathode is amplified up to 10^6 - 10^7 times by the image intensifier, producing a signal that is much larger than the internal noise of the CCD. For a more detailed description see Gach et al. (2002).

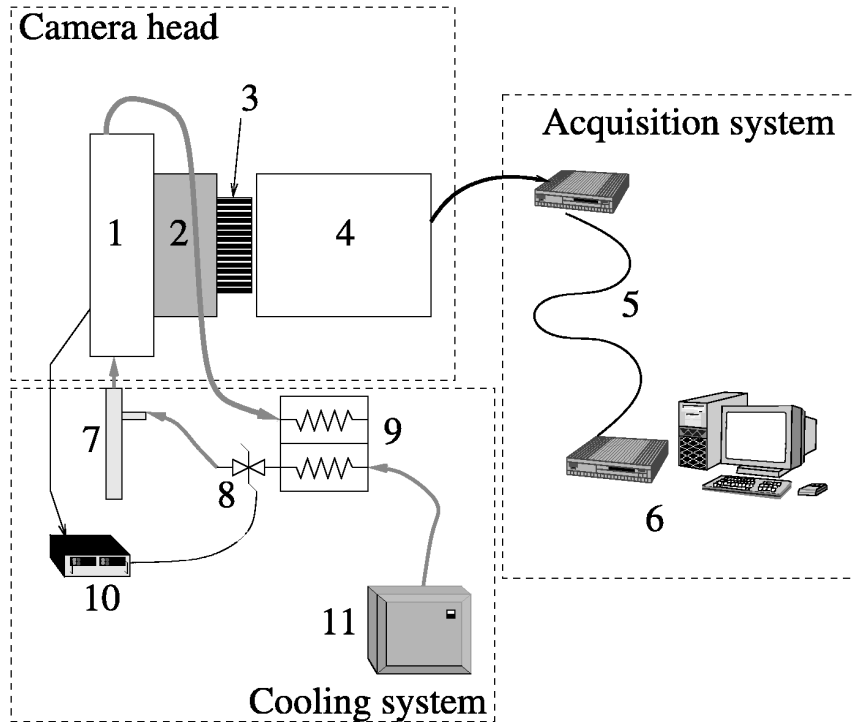


FIG. 2.4: Schematic view of an IPCS (Gach et al. 2002). (1) Cold finger, (2) GaAs tube, (3) fibre coupling, (4) CCD camera, (5) fibre link, (6) host centring computer, (7) vortex tube, (8) proportioning valve, (9) heat exchanger, (10) temperature controller, (11) air compressor and air dryer.

2.4 Observations and data reduction

The FP observations took place in February/March 2006 at the Observatoire de Haute-Provence, France. The 1.93 m telescope equipped with the Marseille's scanning FP interferometer and the new IPCS (Gach et al. 2002) was used. As already mentioned in Sect. 2.1.3, the velocity sampling was 15 km s^{-1} , which is comparable to the resolution of a high-resolution echelle spectrograph.

The IPCS has 512×512 pixels, each $24 \mu\text{m}$ in size, giving a field of view of $5'.8 \times 5'.8$ and therefore a pixel size of $0''.68$. This is similarly high as the spatial resolution achieved when performing imaging. Due to the size of the interference filters, the field of view was slightly limited to $5'.5 \times 5'.5$. This large field of view is one of the major advantages of a FP in comparison to the new fibre spectrographs which usually cover less than 1 arcmin^2 . As the galaxies presented in this thesis are all nearby galaxies, they typically cover several arcmin^2 on the sky, which would result in at least ten pointings with a fibre spectrograph. Using the FP, the main optical parts of all galaxies that were observed for the purpose of this work lie within the field of view.

The observations were taken under non-photometric conditions leading to a seeing of less than $3''$, which made it necessary to bin the data. This does not significantly affect the quality of the data as changes in velocity (e.g., due to outflowing gas) are not expected to take place on such small scales. The night sky lines give a velocity resolution of 50 to 60 km s^{-1} , which causes a bit more trouble than the bad seeing. The outflows found in dwarf galaxies typically have expansion velocities in the range from 20 to 60 km s^{-1} (e.g., van Eymeren et al. 2007). Having a velocity resolution of 50 to 60 km s^{-1}

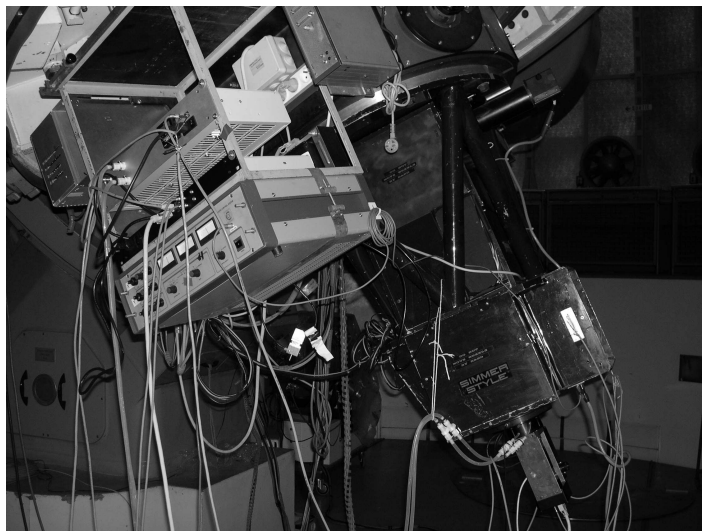


FIG. 2.5: The Marseille's scanning Fabry-Perot interferometer attached to the 1.93 m telescope at the Observatoire de Haute-Provence. The picture was taken during the observing run in March 2006 by M. Marcelin.

could therefore mean that low-velocity outflows, especially when they are of low intensity, are only seen as an asymmetry in the line profile, which makes them difficult to fit, or even remain undetected.

The data reduction was performed using the ADHOCw¹ software which is online available and was written by Jacques Boulesteix (CNRS, Marseille). This software is exclusively written for FP data and includes tools for the whole data reduction procedure as well as analysis and display tools. Additionally, a package exists that allows a conversion of the data from the ADHOCw format to more conventional formats like, e.g., the fits format.

A short overview about the standard data reduction process is given in Fig. 2.6. First of all, the cycles have to be checked and cycles which were obtained under bad conditions are sorted out. Afterwards, the data are added channel per channel. In a next step, the phase map has to be created, which forms the basis for the wavelength calibration. Therefore, an exposure of a calibration lamp, in this case a neon lamp, had to be taken during the observations. Fig. 2.7 visualises why a phase calibration is needed: only one single wavelength of the neon lamp was chosen and scanned through all channels, which should lead to the same intensity distribution in every pixel of the whole field of view. Looking at one pixel and following it over all channels, an intensity distribution can be plotted (bottom part of Fig. 2.7). Although only one single line was observed, the channel where the intensity peaks varies from pixel to pixel. Therefore, an “origin” channel has to be defined, for which all the pixels have their intensity peaking at maximum, which means that the intensity maxima of many pixels have to be shifted to other channels in order to get the same wavelength origin for all pixels of the observed field. This so-called phase map, which contains the information about every pixel, is then used to perform a wavelength calibration of the scientific data.

Spectral and spatial smoothing as well as the subtraction of the night sky lines are the final steps of the data reduction. In this case, the subtraction of the night sky was not possible as no flatfield correction could be applied due to a not sufficient number of flatfield exposures. The consequences are described in more detail in Sect. 2.5.

¹Analyse et Dépouillement Homogène des Observations Cigale, <http://www.oamp.fr/adhoc/>

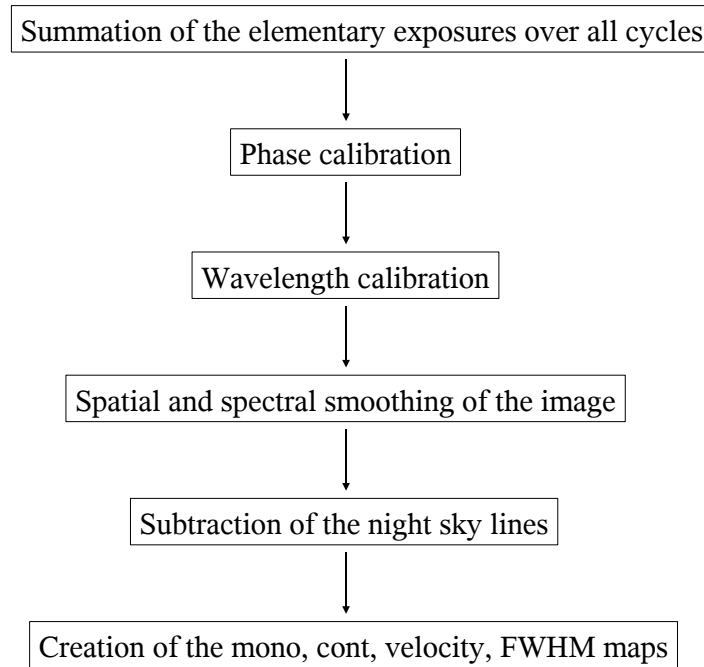


FIG. 2.6: The most important steps of the Fabry-Perot data reduction.

In the end, the monochromatic and the continuum image as well as the velocity and the Full Width at Half Maximum (FWHM) maps can be computed.

For a detailed kinematic analysis, the ADHOCw software was proved to be not sufficient. Therefore, the data had to be converted into the standard fits format and were analysed with a mixture of radio and optical astronomy software, in particular MIRIAD² and IRAF³. As IRAF cannot handle 3d data very well, the spectra are extracted pixel by pixel with the MIRIAD task *gaufit*. In IRAF, the resulting ASCII-files, containing two columns (wavelength and intensity), are then converted into a spectrum by summing over 3×3 pixels to improve the S/N ratio and to match the seeing (see above).

As the field of view is quite large, an automatic fitting routine for the Gaussian decomposition is desired. MIRIAD, IRAF and also ADHOCw all offer such a task and they were all tested during this work. These tasks work well on spectra containing a single, symmetric and well-resolved emission line. As soon as the spectrum shows an asymmetry in the emission line (indicating a second superimposed component) or a second, clearly separated component, the fits are not reliable any longer. In order to perform a Gaussian decomposition, initial estimates of the peak velocity, the FWHM and the intensity are needed. This is difficult as no prior knowledge of the outflows is available. Therefore, an automatic fitting routine is not recommended for the purpose of this work. In the end, the Gaussian decomposition task *splot* in IRAF was taken, and all lines were measured interactively. The whole procedure is described in App. A.

²Multichannel Image Reduction, Image Analysis and Display

³Image Reduction and Analysis Facility

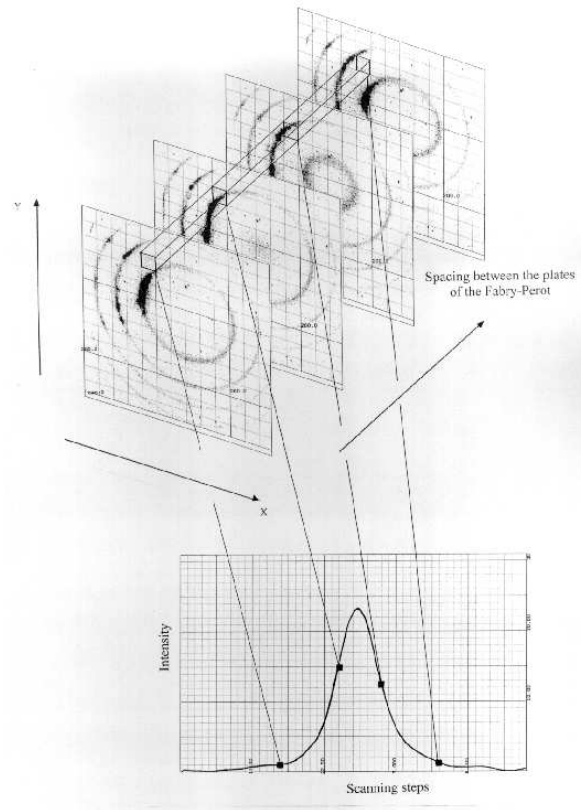


FIG. 2.7: Schematic representation of the FP's scanning process. The interference pattern of four channels is shown in the upper part. Looking at one pixel, an intensity distribution of the observed emission line over all channels can be plotted (lower part).

2.5 Technical issues of the observations and the data reduction

Fig. 2.8 shows the velocity map of NGC 2366 created by ADHOCw. A comparison of this map with the corresponding $H\alpha$ image (see Chap. 3, Fig. 3.1 right panel) reveals emission in some areas of the velocity map which cannot be seen on the $H\alpha$ image. The black circles surround so-called ghosts which are reflections from bright emission line regions between the interference filter and the interferometer itself. The black cross marks the position of the centre of reflection which coincides with the optical axis. These artefacts have already been described in detail by Georgelin (1970).

The upper ghost in Fig. 2.8 was caused by the bright Giant Extragalactic H II Region (GEHR) in the south of the galaxy, the reflection on the right side by the arm-like feature to the east of the galaxy. Note that the small H II region in the very south of the GEHR is real. A comparison of the intensity revealed that the intensity of the ghost is typically a factor of 40 lower than the intensity of the real emission. Therefore, all ghosts could immediately be ruled out either by looking at the $H\alpha$ images or by looking for the bright real counterpart taking into account the difference in intensity.

The black arrows in Fig. 2.8 indicate a different kind of artefacts caused by blurring inside the detector, which leads to an artificial velocity gradient on very bright emission line regions. These artefacts have not been mentioned in the literature, yet. The blurring within the detector can only be seen when the detected emission is very bright. This is the case for the GEHRs in NGC 2366 and NGC 4861. NGC 2366 has been observed before within the ‘‘Gassendi $H\alpha$ Survey of Spirals’’

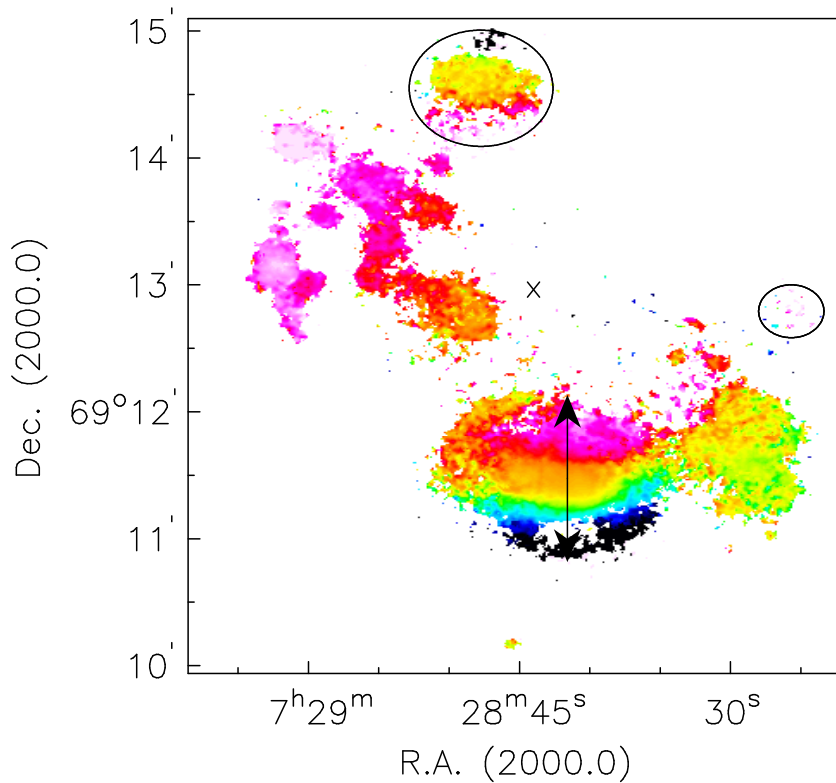


FIG. 2.8: Artefacts on the $H\alpha$ velocity field of NGC 2366 as created with ADHOCw. A comparison with the corresponding $H\alpha$ image shows areas of emission which cannot be seen on the $H\alpha$ image. The black circles surround so-called ghosts which were caused by the FP interferometer and are reflections from bright emission line regions. The black cross marks the position of the centre of reflection (optical axis). The black arrows indicate a different kind of artefacts caused by the detector, which leads to an artificial velocity gradient on very bright emission line regions (in this case on the luminous H II region in the south).

(GHASP⁴), but the exposure times were much shorter so that no reflection is visible on the old velocity field. However, Section 4.5.2 will show that this problem has already existed before, but was not recognised as such. For the data presented in this thesis, the gradient could successfully be removed and all detected velocities were checked by comparing the FP data with the already analysed and published echelle spectra (see van Eymeren et al. 2007).

A completely different problem came up during the data reduction process: a standard data reduction usually includes a flatfield correction which is necessary because of the varying night sky brightness. Another important factor is the correction of artefacts caused by defects or dust grains on the filter. The transmission of the interference filters used for these observations depends on the wavelength and on the position. A flatfield could correct for the uncertainties, but the integration times have to be very long when using a photon counting system. As only eight cycles per filter were obtained for these observations, the signal per channel was far too low, but as the main purpose of the data was the performance of a kinematic analysis and not photometry, this problem was not severe. On the other hand, the spectra are affected by the night sky lines, not only from the ones of the observed free spectral range, but also from neighbouring ones as the interference filters did not completely suppress neighbouring wavelengths. The intensity of all these lines varied over the field of

⁴<http://www.oamp.fr/interferometrie/GHASP/ghasp.html>

view without an identifiable order. The flatfield correction might have helped to bring the intensities to one level and to successfully subtract the lines. Instead, a median night sky profile was subtracted from every pixel leading to residuals and over-subtraction in many pixels. Especially the data of NGC 4861 were strongly affected by several night sky lines. Therefore, a new detected outflow was always cross-checked with a list of night sky lines from the desired and the neighbouring free spectral ranges.

Spiral structure in NGC 2366*

Abstract

NGC 2366, classified so far as an IB(s)m dwarf galaxy, shows at several wavelengths indications for spiral arm structure. A look at the $H\alpha$ morphology and kinematics shall give further evidence.

Fabry-Perot interferometry of NGC 2366 centred on the $H\alpha$ line was performed with the Marseille's scanning Fabry-Perot. Additionally, a deep $H\alpha$ image that also includes the outer regions of NGC 2366 was obtained and compared with the FUV GALEX image.

Our $H\alpha$ velocity field in combination with the $H\alpha$ and GALEX images reveals that NGC 2366 has two weak spiral arms traced by chains of small H II regions, one emanating from the northern tip to the south, the other one emanating from the H II region west of the Giant Extragalactic H II Region to the north. The upper part of the eastern arm shows the typical wiggles indicating a density wave action.

3.1 Introduction

A dwarf galaxy is a system having $M_B^0 > -18$ and an isophotal diameter $D_0 < 5$ kpc. The presence and especially the detection of spiral structure in dwarf galaxies is a particularly rare phenomenon. Ferguson & Sandage (1991) wrote that “dwarf spiral galaxies do not appear to exist”. First evidence for their existence was given by Schombert et al. (1995). Even then, they concluded that dwarf spiral galaxies only exist in the field. The harsh environment in a cluster – due to galaxy mergers, interaction with each other or with the intracluster medium, and/or strong gravitational tidal interactions – is commonly thought to have led to the destruction of the delicate spiral patterns in dwarf galaxies.

During the last decade more dwarf galaxies with faint spiral structure were found (e.g., Jerjen et al. 2000; Barazza et al. 2002; Graham et al. 2003), although they all belong to the class of dwarf elliptical galaxies. As they lack HI gas and star formation, the nature of this spiral structure may be different. Concerning the nature and probability of classical spiral patterns in gas-rich dwarf galaxies, there has been little research beyond morphological classification.

*van Eymeren, J., Marcelin, M., Bomans, D.J., & Dettmar, R.-J. 2008, *subm. to A&A*

NGC 2366 was classified up to now as a barred Magellanic-type irregular (IB(s)m) dwarf galaxy (de Vaucouleurs et al. 1991, hereafter RC3). Its appearance in $H\alpha$ is dominated by the Giant Extragalactic H II Region (GEHR) NGC 2363 in the south-west with a luminosity twice as bright as 30 Doradus (Chu & Kennicutt 1994). The distance of 3.44 Mpc was adopted by Tolstoy et al. (1995) and places NGC 2366 in the M81 group. Tikhonov & Galazutdinova (2008) measured a new TRGB distance of 3.13 ± 0.25 Mpc, which is still in good agreement with the value derived by Tolstoy et al. (1995). In the subsequent analysis the value of Tolstoy et al. (1995) is used. The nearest neighbour of NGC 2366 is the spiral galaxy NGC 2403 at a projected distance of 290 kpc.

NGC 2366 shows several peculiarities. The photometric HST observations by Tikhonov & Galazutdinova (2008) reveal an overdensity of blue stars at a galactocentric distance of 0.9 kpc against the overall decrease in the young-star number density with galactocentric distance. At the same distance H I observations by Hunter et al. (2001) and Thuan et al. (2004) show the presence of two parallel ridges running along the major axis, which they interpret as a deprojected H I ring. A third peculiarity is the H II complex west of the GEHR, which is often referred to as a satellite galaxy interacting with NGC 2366 (e.g., Drissen et al. 2000), despite its similarity with the Shapley constellation III in the LMC (Nail & Shapley 1953).

Tikhonov & Galazutdinova (2008) suggest from their results of the stellar photometry that the H I ridges found by Hunter et al. (2001) and Thuan et al. (2004) could be weak spiral arms. This chapter gives further evidence for the existence of spiral arm structure in NGC 2366 from deep optical and UV images and Fabry-Perot interferometry.

3.2 Observations and data reduction

3.2.1 Optical imaging

A 900 s R -band image and a deep – 3600 s – $H\alpha$ image were obtained with the Calar Alto 3.5m telescope. After the standard data reduction with the software package IRAF, the continuum image was subtracted from $H\alpha$ to produce an image of the pure $H\alpha$ line emission. In order to emphasise weaker structures and to differentiate them from the noise, we used adaptive filters based on the H-transform algorithm (Richter et al. 1991, see App. B). Both images are shown in Fig. 3.1.

3.2.2 Fabry-Perot interferometry

Fabry-Perot (FP) interferometry of NGC 2366 was performed at the 1.93m telescope at the Observatoire de Haute-Provence, France. We used the Marseille’s scanning FP and the new photon counting camera (Gach et al. 2002). The field of view is $5'.8 \times 5'.8$ on the 512×512 pixels of the camera and is slightly limited by the interference filter to $5'.5 \times 5'.5$ giving a spatial resolution of $0''.68$ per pixel. The $H\alpha$ line was observed through an interference filter centred at the galaxy’s rest wavelength of 6564.53 \AA with a FWHM of 10 \AA . The free spectral range of the interferometer – 376 km s^{-1} – is scanned through 24 channels with a sampling step of 15 km s^{-1} . The seeing was about $3''$ to $4''$. The spectral resolution is about 50 km s^{-1} .

In total, 60 cycles were observed with an integration time of 10 sec per channel and per cycle. After removing bad cycles, a total integration time of 232 min remained. We used a neon lamp for the wavelength calibration. The data reduction was done with the software package ADHOCw¹, written by Jacques Boulesteix.

¹<http://www.oamp.fr/adhoc/>

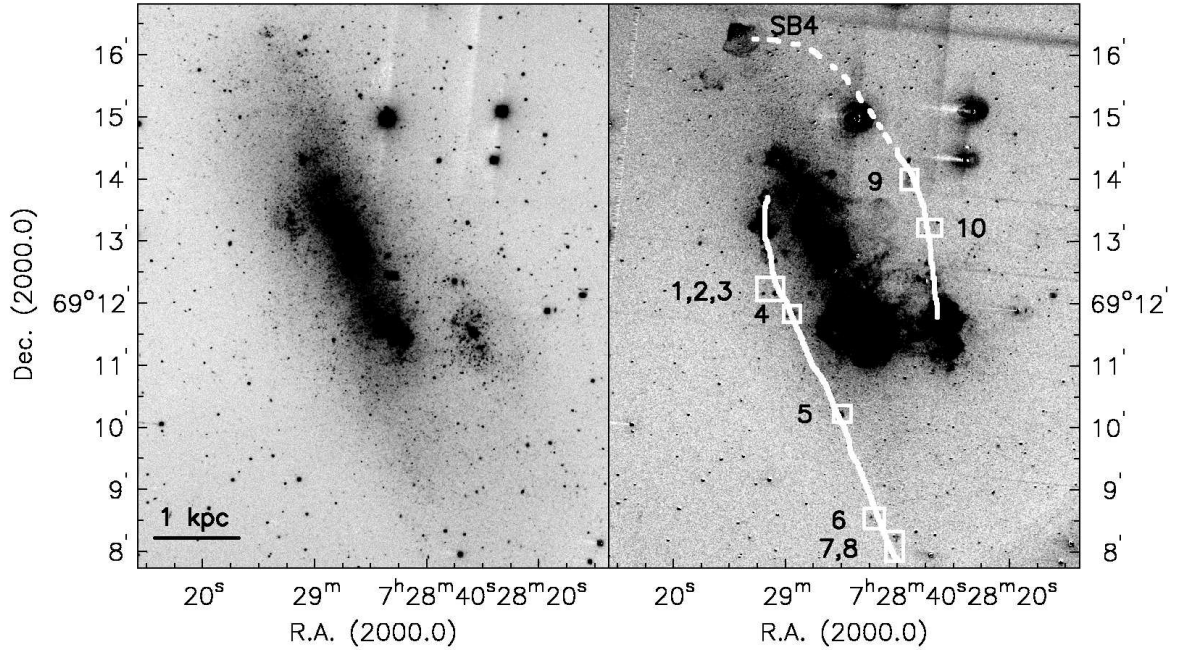


FIG. 3.1: R -band image (left panel) and continuum-subtracted $H\alpha$ image (right panel) of NGC 2366. In order to stress weaker structures and to differentiate them from the noise, we used adaptive filters based on the H-transform algorithm (Richter et al. 1991, see App. B). The extraplanar H II regions are marked by white boxes and numbered in black, the spiral arms are indicated by white lines.

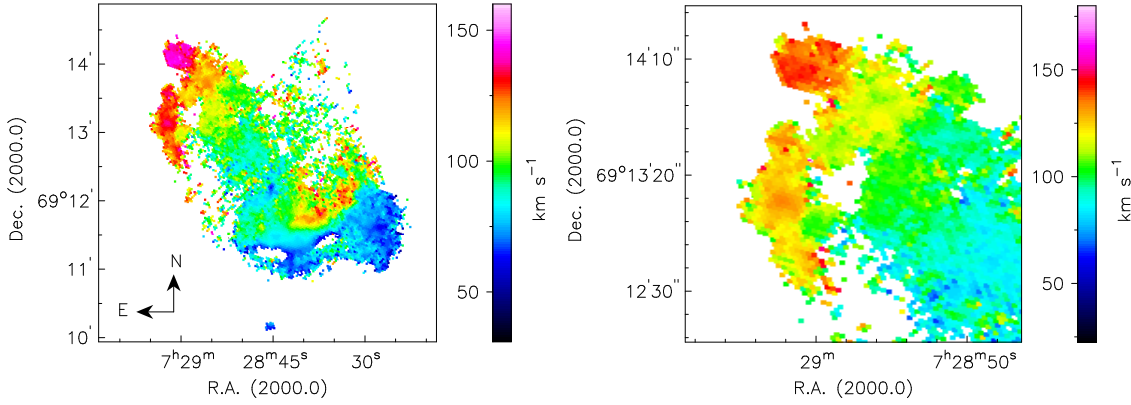


FIG. 3.2: The $H\alpha$ velocity field of NGC 2366. The left panel shows the whole velocity field, the right panel is a zoom into the upper part of the eastern spiral arm showing wiggles of the isovelocity lines.

The $H\alpha$ velocity field is shown in Fig. 3.2. We performed a Gaussian decomposition by interactively fitting the emission (IRAF task *splot*, see App. A). Only detections above a 3σ limit were considered. In order to improve the signal to noise ratio, we summed over 3×3 pixels. All given velocities are heliocentric velocities measured along the line of sight.

3.3 Results

3.3.1 General morphology

The R -band and $H\alpha$ images (Fig. 3.1) cover the stellar extent of the galaxy including the outer regions. The disk is elongated from the south-west to the north-east with the GEHR and its western companion in the south. The R -band image shows two components in the luminosity distribution, an inner luminous and bar-like feature and an outer weaker component. NGC 2366 is strongly inclined with an inclination angle of 65° derived from H I observations (e.g., Hunter et al. 2001). The existence of a bar has been discussed in several publications (e.g., Elmegreen et al. 1996; Hunter et al. 2001). In $H\alpha$, many small and faint H II regions are scattered along both sides of the disk (Fig. 3.1, right panel), the southernmost ones, numbered 7 and 8, at a distance of 2.7 and 3 kpc from the disk (Hunter et al. 2001). On the eastern side of the disk, H II regions can be traced all along the disk from the arm-like structure at a declination of $69^\circ 13'$ via a bright small blob south of the GEHR (H II region number 5) to the two southernmost H II regions mentioned above. On the western side of the disk, this trend is not as obvious, although there are a few H II regions extending from the western large H II region to the north (numbers 9 and 10). A very prominent $H\alpha$ feature is visible at a distance of at least 2 kpc north of the main body of the optical galaxy (SB4, see Fig. 3.1, the numbering follows van Eymeren et al. 2007, their Table A.1). It looks like an expanding superbubble of 500 pc in diameter with a sharply edged half pointing to the north and a more roundish part heading south. The R -band image shows a stellar concentration in the middle. A second faint shell structure can be seen at a distance of 1 kpc from SB4 to the south-east.

3.3.2 $H\alpha$ velocities

The $H\alpha$ velocity field (Fig. 3.2, left panel) only shows the main body of NGC 2366. Nevertheless, the eastern distinct H II regions are clearly visible. The overall velocity gradient runs from the south-west with velocities of about 60 km s^{-1} to the north-east with velocities of about 140 km s^{-1} , which is consistent with H I observations by, e.g., Thuan et al. (2004). The arm emanating from the north-eastern part of NGC 2366 to the south shows broad and smooth wiggles in the upper part (see Fig. 3.2, right panel). The velocity of the arm is offset in comparison to the overall velocity gradient by 30 km s^{-1} red-shifted. Some of the tiny H II regions also show higher velocities than expected from the gradient. The H II region number 5 fits well into the overall velocity pattern.

3.4 Discussion of the peculiarities in NGC 2366

Based on our data and by taking into account other analyses of NGC 2366, we discuss in the following subsections that this galaxy appears to show a two-armed spiral pattern.

3.4.1 The GALEX view

The GALEX FUV image of NGC 2366 (see also Gil de Paz et al. 2006) is taken for a comparison with the $H\alpha$ image. The UV emission allows us to trace the slightly longer-lasting stars (e.g., B-type stars) in comparison to $H\alpha$, which gives us primarily the O-type stars. This facilitates our search for the spiral arm structure as the star distribution is more pronounced on the UV image.

Superimposing the GALEX contours onto the $H\alpha$ image (see Fig. 3.3) shows that the small extra-planar H II regions coincide very well with some knots on the GALEX image. The GALEX contours

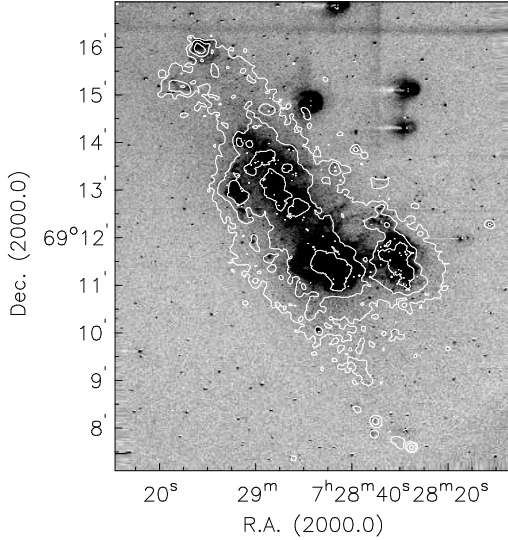


FIG. 3.3: The GALEX FUV contours overlaid onto the continuum-subtracted $H\alpha$ image.

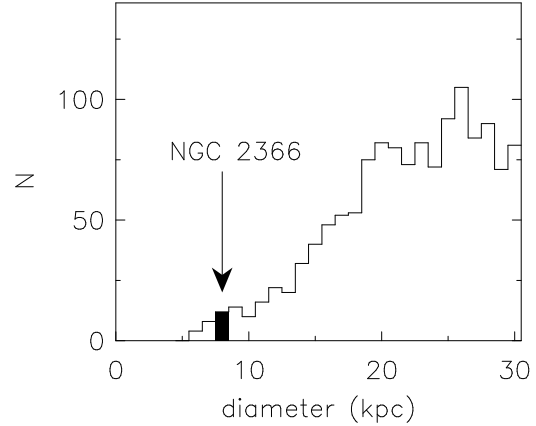


FIG. 3.4: Statistical properties of dwarf spirals. The distribution of optical diameters in kpc shown for all spirals in the UGC with HI detection (Schombert et al. 1995). The position of NGC 2366 is marked.

already give the impression of an arm-like structure along the eastern side to the south. As stated from the $H\alpha$ image (see Sect. 3.3.1), the western arm is not as pronounced as the eastern arm.

The UV emission is very extended to the north. Similar to the R -band image, the luminosity drops, but the connection between the main body and the shell structures is more obvious (due to the above mentioned reason). The UV image even shows several smaller knots of high intensity at the positions of both shell structures, clearly marking the stellar complexes driving the shells.

3.4.2 H I ring

The classification by RC3 implies some weak s-shaped structure, but the publications of the last decade all discussed against spiral structure in NGC 2366 (e.g., Hunter et al. 2001; Thuan et al. 2004). Thuan et al. (2004) present H I synthesis maps of NGC 2366. In their Fig. 5 they show a grid of individual H I line profiles. Most of the profiles show a single emission line, but on the edges they found double profiles. Compared to our $H\alpha$ or the GALEX image, the regions of double profiles coincide with the positions of the spiral arms. These are even visible on Thuan's H I channel maps in Fig. 3. Hunter et al. (2001) found the same H I morphology, but all authors exclude the possibility of a spiral arm pattern and interpret the structure as a deprojected H I ring. Our analysis reveals that NGC 2366 shows evidence for spiral structure in the optical, the UV and the radio.

Interestingly, an offset becomes obvious when comparing the position of the double profiles and the spiral arm structure on the channel maps with the ionised gas shells. This means that most probably the shells are not connected to the western spiral arm.

3.4.3 Satellite galaxy to the west

The $H\alpha$ velocity field (Fig. 3.2) shows that the velocity gradient of the western H II region is consistent with the overall velocity gradient. Additionally, it marks the site where the western spiral arm comes out of the bar. This gives evidence against the statement by, e.g., Drissen et al. (2000) that the western H II region may not belong to NGC 2366, but is a satellite galaxy. The region is therefore most likely a superassociation or stellar complex (e.g., Elmegreen & Efremov 1996; Braun et al. 1997), much like the Shapley constellation III in the LMC.

3.4.4 Properties of (dwarf) spirals

Schombert et al. (1995) show in a histogram the number density of all spirals in the UGC catalogue (Nilson 1973) versus their optical diameter. This distribution peaks at large diameters of 20 to 30 kpc, whereas only few galaxies are found below diameters of 6 kpc. The dwarf galaxies found by Schombert et al. (1995) are all at the lower end of the distribution with diameters of less than 5 kpc and luminosities of $M_V > -17$ mag. Figure 3.4 shows the same histogram. The position of NGC 2366 is marked. As the galaxy has a large major to minor axis ratio in the optical, we take the diameter of the major axis (about 8 kpc) as an upper limit. Although this value is almost twice as high as the diameters of the dwarf spirals detected by Schombert et al. (1995), NGC 2366 is still at the lower end of the distribution. With a luminosity of $M_V = -17.27$ mag (RC3) and applying a distance of 3.44 Mpc, it fits well to the dwarf spirals. These results place NGC 2366 in a greyzone between the dwarf spirals found by Schombert et al. (1995), which are all low surface brightness galaxies, and normal spiral galaxies.

3.5 Conclusions

From our observations we suggest that NGC 2366, which is classified as an irregular dwarf galaxy with weak spiral structure, has indeed two spiral arms which can be traced in the shape of small H II regions outside the disk on our $H\alpha$ velocity field and the $H\alpha$ image and are consistently visible on the GALEX FUV image. Their positions coincide with the previously detected H I ring by Hunter et al. (2001) and Thuan et al. (2004). Additionally, we detect wiggles in the $H\alpha$ velocity contours, which is a commonly observed phenomenon when the material crosses spiral arms. The western large H II region seems to belong to the western spiral arm and is most probably not a satellite galaxy as suggested before. A comparison with the properties of classical spirals and the dwarf spirals found by Schombert et al. (1995) shows that NGC 2366 lies between both kinds of galaxies. The detection of the spiral pattern in NGC 2366 opens the question how many star forming irregular dwarf galaxies show density wave driven spiral arms and where the limiting parameters for a density instability in disks really are.

Assuming a density wave that produces the spiral arms implies an offset of the spiral pattern from H I to $H\alpha$ (Roberts 1969). A comparison of the H I data by Thuan et al. (2004) with our $H\alpha$ image shows no significant deviations. Still, this offset is small and therefore difficult to detect. A clear measurement is up to now only possible in extreme grand-design spiral galaxies like M 51. Therefore, an analysis of deep H I data and a comparison with the optical and UV data is necessary to look which parameters allow the formation of spiral arms in NGC 2366.

Acknowledgements. The authors would like to thank Jean-Luc Gach and Philippe Balard for settling the new detector and their technical support. This work was partly supported by the Deutsche Forschungsgesellschaft (DFG) under the SFB

591. Our results are partly based on observations collected at the Centro Astronómico Hispano Alemán (CAHA) at Calar Alto, operated jointly by the Max-Planck Institut für Astronomie and the Instituto de Astrofísica de Andalucía (CSIC). GALEX (Galaxy Evolution Explorer) is a NASA Small Explorer, launched in April 2003. We gratefully acknowledge NASA's support for construction, operation, and science analysis for the GALEX mission, developed in cooperation with the Centre National d'Etudes Spatiales (CNES) of France and the Korean Ministry of Science and Technology.

A comparison of the neutral and ionised gas kinematics in the irregular dwarf galaxy NGC 2366

Abstract

Star-forming irregular dwarf galaxies provide a perfect environment to study feedback processes because their gas kinematics support the long-term survival of shells, filaments and holes. In order to perform a comparison between the neutral and ionised gas kinematics, H I and H α observations of the nearby irregular dwarf galaxy NGC 2366 were performed.

A deep H α image, Fabry-Perot as well as VLA H I data of NGC 2366 were obtained. In addition to a comparison of the morphology of the neutral and ionised gas, we searched for line-splitting in H α and H I by performing a Gaussian decomposition.

A huge red-shifted outflow north-west of the Giant Extragalactic H II Region with an expansion velocity of up to 50 km s⁻¹ is found in H α , but not in H I, as well as an underlying blue-shifted component in the northern part both in H α and H I with an expansion velocity of up to 30 km s⁻¹. A comparison of the expansion velocities of these outflows and the escape velocities of NGC 2366, calculated by modelling a pseudo-isothermal halo, reveals that the gas has not enough kinetic energy to leave the gravitational potential.

4.1 Introduction

Irregular dwarf galaxies are known to be the sites of giant star formation regions. The feedback between massive stars and the interstellar medium (ISM), on larger scales also the intergalactic medium (IGM) is one of the most important processes in the evolution of these galaxies. Massive stars are strong sources of radiation and mechanical energy. Photoionisation is the most probable mechanism, but also shocks that are produced by stellar winds and supernova (SN) explosions inject energy into the ISM, which leads to numerous ionised structures in and around the galactic plane (e.g., Bomans et al. 1997; van Eymeren et al. 2007). However, ionised gas also exists at kpc distances away from

any place of current star formation (Hunter et al. 1993). These structures might be fragmented cool shell structures that were left behind by the expanding hot gas (Mac Low & Ferrara 1999), but they can also be explained by turbulent mixing between the hot and the neutral gas (Slavin et al. 1993).

In order to explain the observations, theoretical models were developed in which the gas is shock-heated by collective supernovae and accelerated into the ISM forming a thin shell of swept-up ambient gas. Due to Rayleigh-Taylor instabilities the shell can rupture and the hot gas is expelled through tunnel-like features, called chimneys, into the halo of the host galaxy (Norman & Ikeuchi 1989). Depending on the strength of the gravitational potential, the hot gas might be able to fall back onto the galactic disk as cool clouds, which is described in the *Galactic Fountain* scenario (Shapiro & Field 1976). In some cases, the gas can even be accelerated to velocities beyond the escape velocity of the host galaxy.

Especially the relatively low escape velocity of dwarf galaxies will facilitate the removal of substantial amounts of interstellar matter. Therefore, the question comes up whether the gas stays gravitationally bound to the galactic disk (outflow) or whether it can escape from the gravitational potential by becoming a freely flowing wind (galactic wind). Numerical simulations by Mac Low & Ferrara (1999) model superbubble blowout and blow-away in dark matter dominated dwarf galaxies of different mass and with different kinetic luminosities. Their models show that only a little fraction of the gas can escape from the gravitational potential, but that the metals, produced by massive stars and released during a SN explosion, have a high probability to be blown away (see also Sect. 1.1). Low mass dwarfs ($< 10^7 M_{\odot}$) can even lose their complete metal-enriched material.

Therefore, star-forming irregular dwarf galaxies provide a perfect environment to study feedback processes and to hunt for galactic winds. A number of studies concentrated on the kinematics of ionised gas structures (e.g., Hunter & Gallagher 1997; Martin 1998; van Eymeren et al. 2007), others on the distribution and kinematics of the neutral gas (e.g., Thuan et al. 2004). Only few studies address both components together in an extensive analysis. Additionally, most authors use a small number of long-slit spectra for their examination of the ionised gas component and try to extrapolate from these few spatial information to the whole galaxy. Only during the last years, the so-called 3d spectroscopy has become more popular which allows to observe large parts of a galaxy or even the whole galaxy together with sufficient spectral information in one exposure (e.g., Wilcots & Thurrow 2001).

In this paper we present a study of the neutral and ionised gas component in the nearby irregular dwarf galaxy NGC 2366. The ionised gas was observed with a Fabry-Perot interferometer centred on the $H\alpha$ line that provides us with a complete spatial coverage of the stellar disk and relevant spectral information.

NGC 2366 is classified as a barred Magellanic-type irregular (IB(s)m) dwarf galaxy (de Vaucouleurs et al. 1991). Its appearance in $H\alpha$ is dominated by the Giant Extragalactic H II Region (GEHR) NGC 2363 in the south-west with a luminosity twice as bright as 30 Doradus (Chu & Kennicutt 1994). Recent observations by van Eymeren et al. (2007) revealed the existence of numerous ionised gas structures up to kpc-size, especially close to the GEHR where most of the current star formation activity takes place. Several of them have been shown to expand. The expansion velocities, however, were in all cases much smaller than the escape velocities of the galaxy. We adopt a distance of 3.44 Mpc from Tolstoy et al. (1995) that places NGC 2366 in the M81 group. The nearest neighbour is NGC 2403 at a projected distance of 290 kpc, which makes any kind of interaction unlikely.

This chapter is organised as follows: The observations and the data reduction are described in § 4.2. Sect. 4.3 is a comparative description of the $H\alpha$ and H I morphology. § 4.4 presents a kinematic analysis of both $H\alpha$ and H I data. The results are subsequently discussed in § 4.5, which will be followed by a short summary in Sect. 4.6.

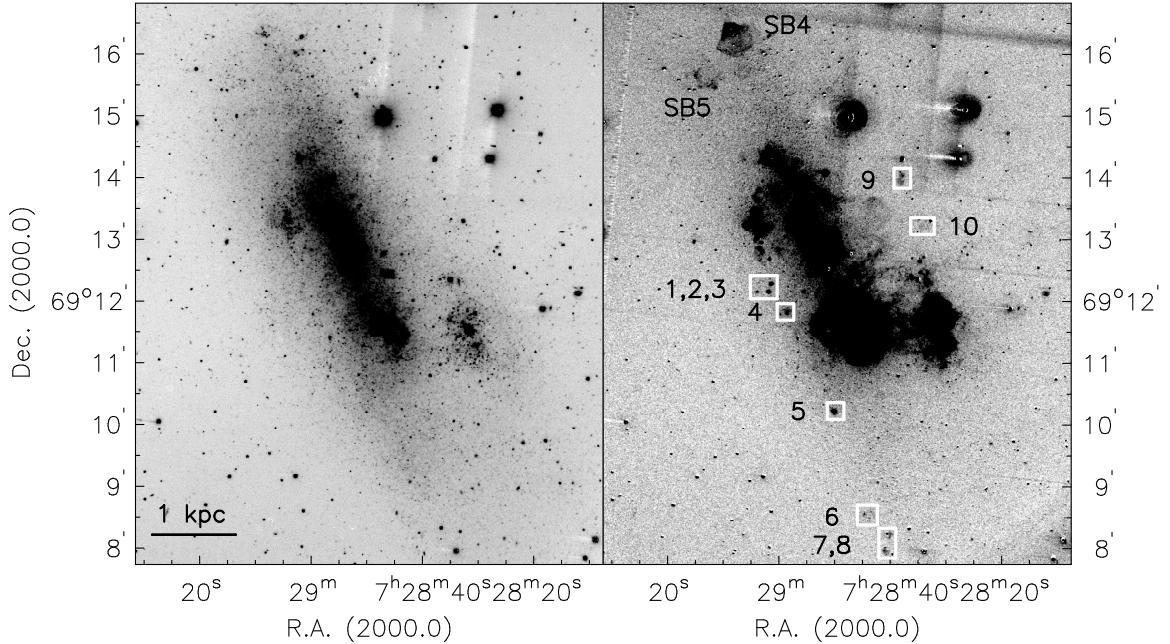


FIG. 4.1: R -band image (left panel) and continuum-subtracted $H\alpha$ image (right panel) of NGC 2366. In order to stress weaker structures and to differentiate them from the noise, we used adaptive filters based on the H-transform algorithm (Richter et al. 1991, see App. B). The extraplanar H II regions are marked by white boxes and numbered in black. Additionally, the two northern superbubbles are numbered following van Eymeren et al. (2007).

TABLE 4.1: The basic parameters of NGC 2366.

Parameters [Unit]	NGC 2366	References
α (J2000)	$07^{\text{h}} 28^{\text{m}} 54.6^{\text{s}}$	
δ (J2000)	$+69^{\circ} 12' 57''$	
Hubble Type	IB(s)m	(1)
m_B [mag]	-16.63	(2)
D [Mpc]	3.44	(3)

References: (1) de Vaucouleurs et al. (1991), (2) Bomans (2001), (3) Tolstoy et al. (1995)

4.2 Observations and data reduction

4.2.1 Optical imaging

A 900 s R -band image and a deep -3600 s $-H\alpha$ image were obtained on the 16th of October 2007 with the Calar Alto 3.5m telescope equipped with MOSCA, the Multi Object Spectrograph for Calar Alto. After the standard data reduction with the software package IRAF, the continuum image was subtracted to produce an image of the pure $H\alpha$ line emission. In order to emphasise weaker structures and to differentiate them from the noise, we used adaptive filters based on the H-transform algorithm (Richter et al. 1991, see App. B). Both images are shown in Fig. 4.1.

4.2.2 The Fabry-Perot data

Fabry-Perot (FP) interferometry of the irregular dwarf galaxy NGC 2366 was performed on the 1st of March 2006 at the 1.93m telescope at the Observatoire de Haute-Provence, France. We used the Marseille’s scanning FP and the new photon counting camera (Gach et al. 2002). The field of view is $5'.8 \times 5'.8$ on the 512×512 pixels of the detector and is slightly limited by the interference filter to $5'.5 \times 5'.5$, which gives a spatial resolution of $0''.68$ per pixel. The $H\alpha$ line was observed through an interference filter centred at the galaxy’s rest wavelength of 6564.53 \AA with a FWHM of 10 \AA . The free spectral range of the interferometer – 376 km s^{-1} – was scanned through 24 channels with a sampling step of 15 km s^{-1} . The final spectral resolution as measured from the night sky lines is about 50 km s^{-1} . The seeing was about $3''$ to $4''$.

60 cycles were observed with an integration time of 10 sec per channel and per cycle. After removing bad cycles, a total integration time of 232 min remained. We used a neon lamp for the phase and the wavelength calibration. The data reduction was done with the software package ADHOCw¹, written by Jacques Boulesteix. Afterwards, a Gaussian decomposition was performed by interactively fitting the emission (IRAF task *splot*, see App. A). Only detections above a 3σ limit were considered. In order to match the seeing and to improve the signal to noise ratio, we summed over 3×3 pixels. All given velocities are heliocentric velocities measured along the line of sight.

Further details about the FP technique, the observations, and the data reduction process can be found in Chap. 2.

4.2.3 The H I data

We work on a fully-reduced data cube from “The H I Nearby Galaxy Survey” (THINGS, de Blok et al. 2005; Walter et al. 2005), a high spectral and spatial resolution survey of H I emission in 34 nearby galaxies obtained with the VLA in its B, C, and D configuration. The synthesised beam size is $13'' \times 12''$ using a “natural” weighting. The spectral resolution is 2.6 km s^{-1} . For more details see Walter et al. (2008).

Figure 4.2 shows the H I channel maps of the cube after applying a standard Hanning smoothing, superimposed on a greyscale presentation of our *R*-band image. The white cross in the first channel marks the optical centre of the galaxy. The beam is placed into the lower left corner of the same channel. The corresponding heliocentric velocities are indicated in the upper right corner of each channel.

In order to create the moment maps (for a more detailed description see App. C) and to analyse the H I data, the software GIPSY² was used.

4.3 General morphology

In addition to the *R*-band and the $H\alpha$ images presented in Fig. 4.1, a second grey-scale presentation of the $H\alpha$ image with a different contrast in order to emphasise the small-scale structures is given in Fig. 4.12 of App. 4.A. The galaxy has a bar-like appearance. The main star-forming complex is located at the southern end and appears as a GEHR on the $H\alpha$ image. The H II region west of the GEHR is sometimes referred to as a satellite galaxy (e.g., Drissen et al. 2000). Whether an own system or not, this H II region is connected to the stellar disk by diffuse, filamentary gas structures. Following the western edge of the GEHR to the north, further filamentary material is visible. A very interesting

¹<http://www.oamp.fr/adhoc/>

²The Groningen Image Processing System

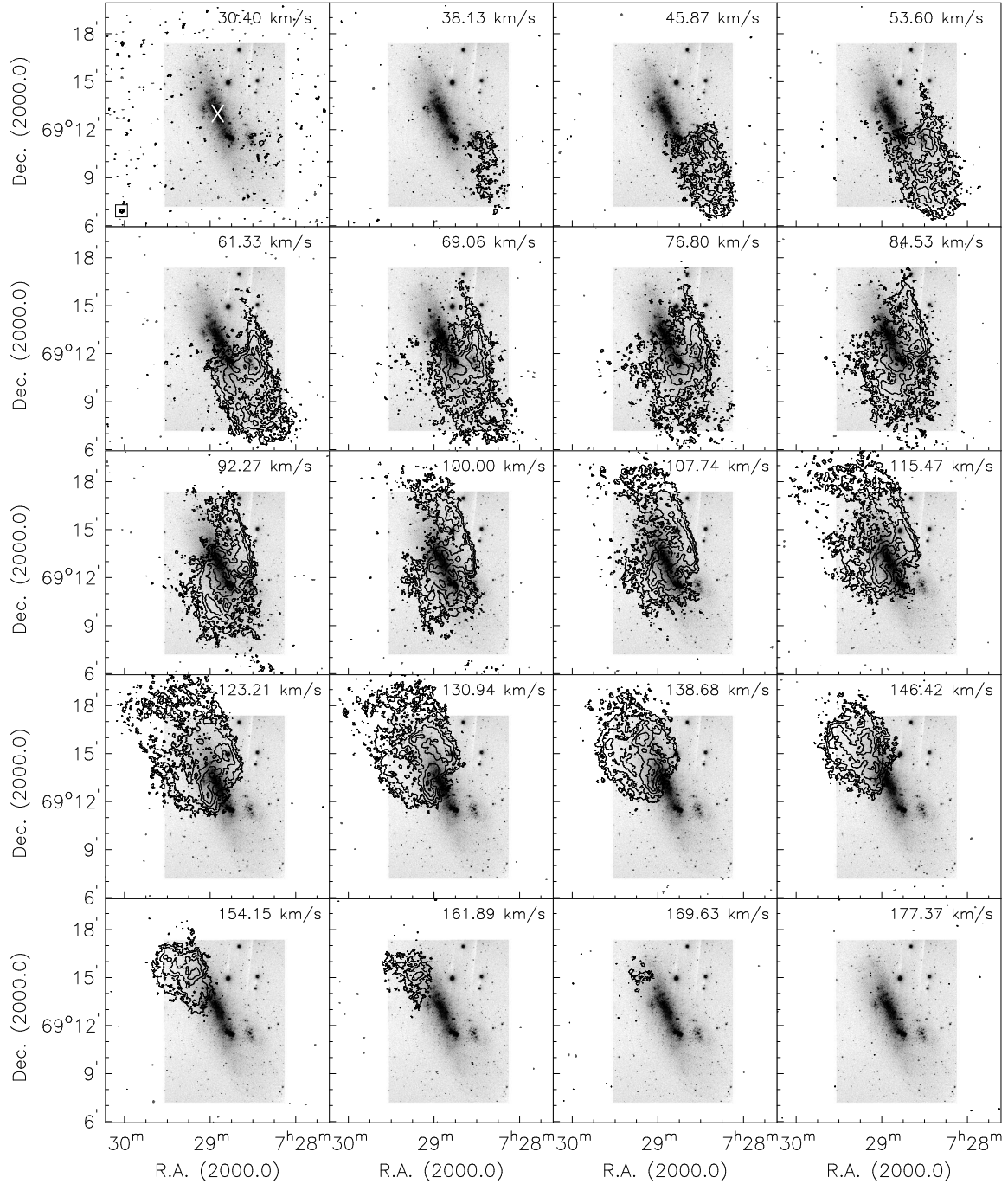


FIG. 4.2: HI channel maps of NGC 2366 (contours) as obtained from the VLA using “natural” weighting of the data, superposed on the *R*-band image. Contours are drawn at -1.5 (-3σ), 1.5 (3σ), 3 , 6 , 12 , and 24 mJy beam^{-1} . The synthesised beam is displayed in the lower left corner of the first channel map. The optical centre of the galaxy is marked by a white cross in the same channel map. The corresponding heliocentric velocities are indicated in the upper right corner of each channel. A standard Hanning smoothing was applied to the cube. The original channel spacing is 2.6 km s^{-1} .

structure is the superbubble (SB4) to the very north of the main body. At the same position, the *R*-band image shows a small cluster of stars. This bubble is remarkable concerning its morphology because it consists of a sharply edged shell heading to the north and a smooth shell heading south. Additionally, there is a second shell, SB5 heading south-east at a distance of 1 kpc in comparison to SB4 without an ionising star cluster nearby. A catalogue of all structures can be found in van Eymeren et al. (2007). The northern structures (SB4, SB5) are new detections as the field of view of the $H\alpha$ image used by van Eymeren et al. (2007) did only cover the main part of the stellar disk. Another peculiarity in NGC 2366 are the very small and faint H II regions that are scattered along the disk on both eastern and western side with no apparent connection to it.

Figure 4.3 shows the H I moment maps of NGC 2366 as well as the global intensity profile. The H I intensity distribution (upper left panel, 0th moment map) is a factor of 2 larger than the optical content of NGC 2366. It looks very patchy with several intensity maxima in the inner parts and a more diffuse filamentary structure in the outer parts. On a larger scale, the H I forms two bright elongated structures or ridges, both parallel to the major axis that are embedded in fainter and smoother gas (see also Hunter et al. 2001; Thuan et al. 2004). The total H I mass derived from the 0th moment map is $6.02 \times 10^8 M_{\odot}$, which lies between the values measured by Thuan et al. (2004) of $3.9 \times 10^8 M_{\odot}$ and by Hunter et al. (2001) of $8 \times 10^8 M_{\odot}$. For all three measurements, a distance of 3.44 Mpc (Tolstoy et al. 1995) was adopted.

Figure 4.4 shows a comparison of the ionised and neutral gas distribution in NGC 2366. In the left panel, the H I contours are overlaid over the continuum-subtracted $H\alpha$ image. The optical galaxy lies in the centre of the H I distribution, i.e., in the area of highest H I intensity. One H I maximum coincides with the GEHR, the region of currently the strongest star formation in NGC 2366. For a more detailed study, Fig. 4.4, right panel shows an enlargement of the main optical part of NGC 2366. Overlaid in white are the H I intensity contours. First, it can be seen that the H I maximum coinciding with the GEHR is slightly offset from the centre of the $H\alpha$ emission. The shift is of the order of one beam size or even more and therefore not a resolution effect. Other examples of such offsets can be found in the literature (e.g., Hodge et al. 1994).

Additionally, the arm-like feature in the north-east as well as the western H II region show an H I intensity maximum. And finally, several smaller H I intensity peaks can be found in the northernmost part of NGC 2366, close to but offset from SB4. SB5 seems to be in a kind of H I hole, which gives rise to the assumption that it expands into the neutral medium by working like a snowplough. The neutral gas in front of the shell is compressed and maybe shock-heated. In the back, a cavity of low densities evolves visible as an H I hole. This phenomenon cannot be observed in the vicinity of SB4, but the filamentary structures north-west of the GEHR are all found in an area of low H I column density.

4.4 Kinematic analysis

The comparison of the neutral and the ionised gas reveals that the distribution of both components is in good agreement. The H I intensity maxima all coincide with the optical extent of the galaxy. Additionally, we found filamentary and shell-like structures in $H\alpha$ which often come along with a low column density in H I. In this section, the kinematic analysis shall give some information about the behaviour of the gas.

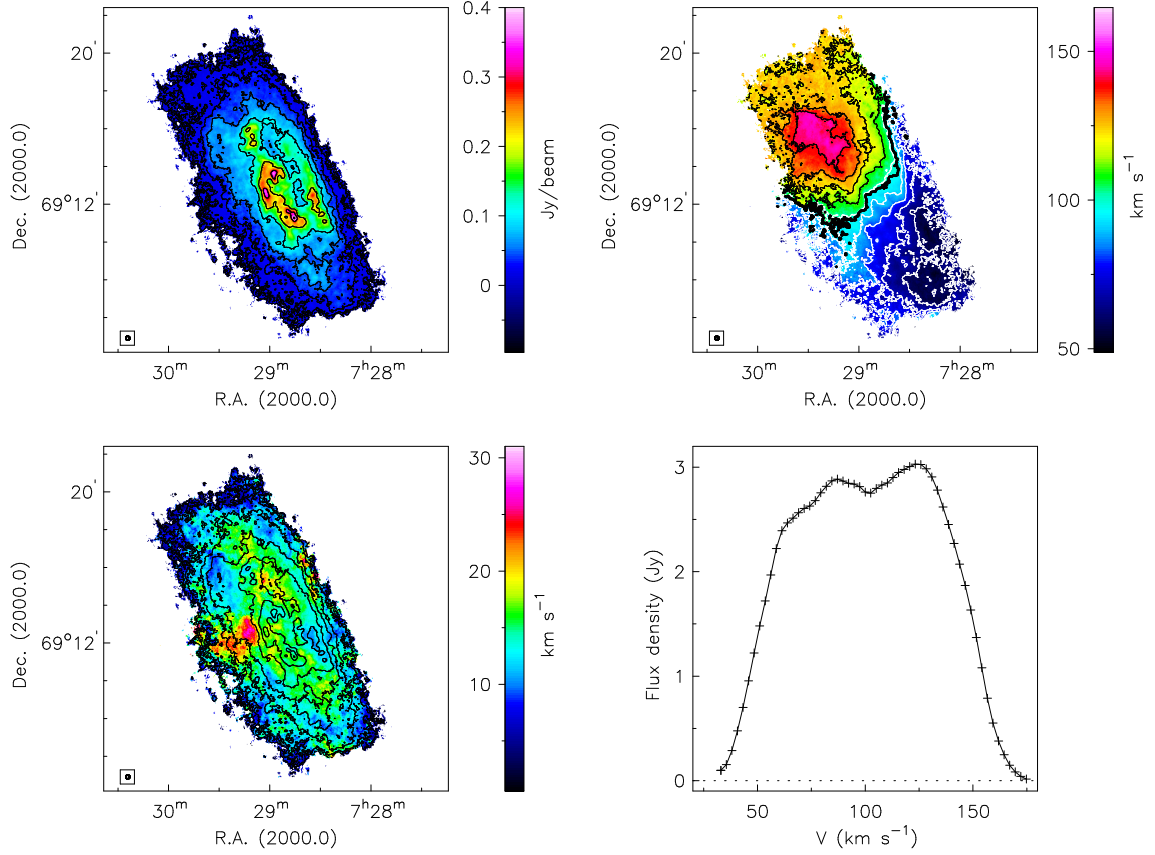


FIG. 4.3: The H I moment maps of NGC 2366 using “natural” weighting, which leads to a synthesised beam of $13'' \times 12''$. **Top left:** The H I intensity distribution (0th moment). Contours are drawn at 0.005, 0.01, 0.025, 0.05, 0.1, 0.2, 0.3, 0.4, 0.5, 0.6, and 0.7 Jy beam^{-1} where 5 mJy beam^{-1} correspond to a column density of $3.6 \times 10^{19} \text{ atoms cm}^{-2}$. **Top right:** The H I velocity field (1st moment). Contours are drawn from 40 to 160 km s^{-1} in steps of 10 km s^{-1} . The systemic velocity of 97 km s^{-1} is marked in bold. **Bottom left:** The velocity dispersion (2nd moment), overlaid are the same H I intensity contours as on the 0th moment map. **Bottom right:** The global intensity profile of the galaxy. The short-dashed line marks zero intensity.

4.4.1 The $\text{H}\alpha$ velocity field

The Gaussian decomposition reveals that at several places, the $\text{H}\alpha$ line consists of more than one component, which is an indication for expanding gas structures. The left panel of Figure 4.5 shows the resulting velocity field with the component of highest intensity plotted. The overall velocity gradient runs from the south-west with velocities of about 65 km s^{-1} to the north-east with velocities of about 120 km s^{-1} . The major deviations from the rotation are now shortly summarised:

- A huge red-shifted outflow north-west of the GEHR is visible on the $\text{H}\alpha$ velocity field with velocities of up to 130 km s^{-1} in comparison to the rotation velocity of 80 km s^{-1} .
- An underlying blue-shifted component can be seen north of the GEHR with velocities of 60 to 70 km s^{-1} in comparison to the general velocities of 90 to 100 km s^{-1} , which is discussed in more detail in Sect. 4.5.1.

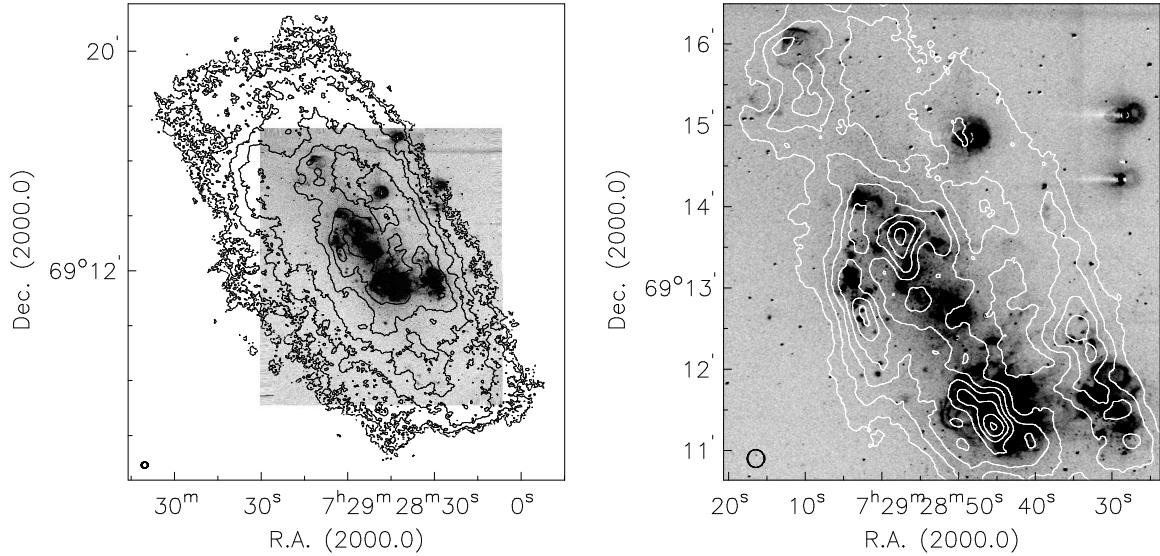


FIG. 4.4: A comparison of the H α and HI morphology. The left panel shows the continuum-subtracted H α image. Overlaid in black are the HI intensity contours at 0.005, 0.01, 0.025, 0.05, 0.1, 0.2, 0.3, 0.4, 0.5, 0.6, and 0.7 Jy beam⁻¹. The right panel displays an enlargement of the optical part. The HI intensity contours are overlaid in white.

- In the northern part of the galaxy, a lot of the emission is much redder than expected from the rotational gradient.
- The western H II region (west of the GEHR) shows the same velocity pattern than the GEHR, which is something to consider in the discussion about this H II region being part of NGC 2366 or a satellite galaxy interacting with NGC 2366.

Part of these peculiarities have already been discussed in Chapter 3. The red-shifted parts in the north belong to a spiral arm that can be traced along the small and distinct H II regions to the south (see Fig. 3.1). The western H II region seems to be part of a second spiral arm that goes to the north and can also be traced by small H II regions.

The most prominent feature is the huge outflow to the north-west of the GEHR, which has been detected before by Roy et al. (1991) also using a FP, and by Martin (1998) and van Eymeren et al. (2007) performing long-slit echelle spectroscopy. Whereas Roy et al. (1991) were strongly limited by the field of view, Martin (1998) and van Eymeren et al. (2007) were limited by the slit size. The new FP exposure now shows the complete size of the outflow. Assuming a distance of 3.44 Mpc, we estimated a total length of 1.4 kpc, which is two times larger than measured by van Eymeren et al. (2007) and even four times larger than observed by Roy et al. (1991). This length makes it one of the largest outflows ever detected in a dwarf galaxy. The gas expands with a velocity of up to 50 km s⁻¹ red-shifted in comparison to the rotational gradient, which is almost a factor of 2 higher than the detections of Roy et al. (1991) and van Eymeren et al. (2007). In case of the observations by Roy et al. (1991), the difference in velocity is most probably due to the fact that they only detected the edge of the outflow where the velocities are indeed lower. The slit position of van Eymeren et al. (2007) intersects the whole outflow. Here the discrepancy could be due to their very limited field of view, which did not give them a true H α rotation curve, or due to their imprecise HI velocity measurements, which they used as a reference value for outflowing gas. The comparison with the HI data will show that the expansion velocity is indeed higher than measured so far (see Sect. 4.4.3).

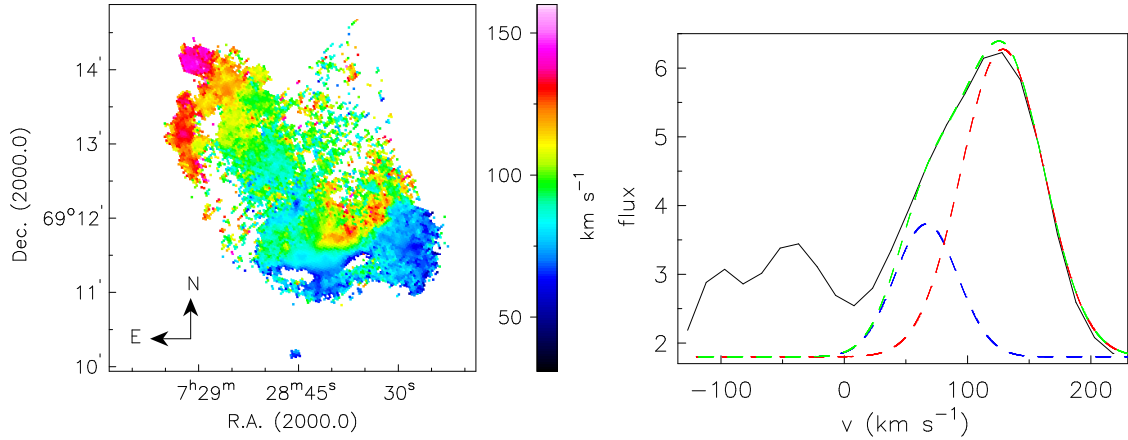


FIG. 4.5: The $H\alpha$ velocity field of NGC 2366. The left panel shows the velocity distribution of the strongest component. The right panel displays one example spectrum (black solid line) at the position of the huge red-shifted outflow which was extracted from the FP data cube. The $H\alpha$ line is split into a component at 70 km s^{-1} (blue long-dashed line) and one at 130 km s^{-1} (red long-dashed line). The sum of both Gaussian fits is plotted in green and is in good agreement with the observed spectrum.

On the right panel of Fig. 4.5, we present as an example one of the spectra extracted from the FP data cube (black solid line). The $H\alpha$ line is split into two components, one at 70 km s^{-1} (blue long-dashed line) and one at 130 km s^{-1} (red long-dashed line). The sum of both Gaussian fits is plotted in green and is in good agreement with the observed spectrum. This is one of the spectra extracted from the area of the huge red-shifted outflow. As can be seen, the outflow dominates the spectrum regarding its intensity, whereas the main component is only visible as a wing on the left side. The lines to the left side of the $H\alpha$ line are night sky lines which could not properly be removed (see Sect. 2.5).

4.4.2 The H I velocity field

The H I velocity field (1st moment map), displayed on the upper right panel of Fig. 4.3, is fairly regular in the inner parts, but quite disturbed in the outer parts. The velocity gradient is rising from the south-west with velocities of about 60 km s^{-1} to the north-east with velocities of about 145 km s^{-1} , which is similar to the $H\alpha$ velocity gradient. The isovelocity contours close at both ends of the galaxy, which is an indication for a declining rotation curve. Especially the north-western part shows a completely different kinematic behaviour than expected from a regularly rotating galaxy.

The velocity dispersion map (Fig. 4.3, lower left panel, 2nd moment) varies between 10 km s^{-1} in the outer parts and 17 km s^{-1} in the inner parts of NGC 2366. The dispersion peaks in an area east of the intensity maxima and in an area clearly offset from them with values up to 28 km s^{-1} . Close to the $H\alpha$ shell in the north, a very small H I peak can be seen with a maximum value of 25 km s^{-1} . The high H I velocity dispersions on the western and eastern edges of the galaxy have to be treated with care. A closer look at the H I velocities in these areas will show that this is an effect of low signal to noise (see Section 4.4.3).

None of these H I velocity dispersion maxima coincides with the optical galaxy. The overlay of the H I intensity contours reveals that the H I maxima are clearly offset from the regions of high velocity dispersion. Figure 4.6, upper left panel shows the H I rotation curve of NGC 2366, which was derived by fitting a tilted-ring model to the observed velocity field (see App. C). Initial estimates (see Table 4.2) for the relevant parameters are the output of an ellipse fitting task (GIPSY task *ellfit*)

TABLE 4.2: HI properties measured from the THINGS data.

Parameters [Unit]	NGC 2366	
	initial estimates	best-fitting values
centre:		
α (J2000.0)	07 ^h 28 ^m 56.2 ^s	07 ^h 28 ^m 55.4 ^s
δ (J2000.0)	+69° 12' 29"	+69° 12' 27"
v_{sys} [km s ⁻¹]	101	97
i [°]	61	64
PA [°]	30	45
v_{rot} [km s ⁻¹]		50
F_{HI} [Jy km s ⁻¹]		147
M_{HI} [10 ⁸ M _⊙]		6.02
HI diameter [']		15 × 7
" [kpc]		15 × 7
HI / opt. ratio		1.9 × 2.8
$\langle \sigma \rangle$ [km s ⁻¹]		10 / 17
σ_{Peak} [km s ⁻¹]		28.2
$r_{\text{HI,max}}$ [kpc]		7.5
M_{dyn} [10 ⁹ M _⊙]		4.3

and are used as an input for the tilted-ring fits (GIPSY task *rotcur*). The width of the rings is chosen to be half the spatial resolution, i.e., 6'' in this case. The black symbols represent the best-fitting parameters derived in an iterative approach from the initial estimates and combining both sides, the error bars define receding and approaching side. A fit with the initial estimates kept fixed is indicated by the green symbols (fixed approach), a fit with the best-fitting parameters kept free is shown by the red symbols (free approach). The green symbols are in very good agreement with the black ones over the whole range of 450''. The red symbols follow the black and green ones up to a radius of 200'' very nicely. From a radius of 300'' on, the deviation is of the order of 30 to 40 km s⁻¹ and also the differences between receding and approaching side become larger. The reason for this is that the filling factors of the rings drop from about 1 to about 0.5 at a radius of 300'', which leads to a higher uncertainty in calculating the rotation velocity. Therefore, all values above this radius have to be treated with care.

In the inner 100'' the velocity gradient is very steep and linear, indicating solid body rotation, which is a characteristic sign of dwarf galaxies. From 100'' to 200'' the curve is still linear, but less steep coming to a plateau at 220''. From 320'' on, the rotation curve declines, which has already been implied by the closing velocity contours in the 1st moment map (Fig. 4.3, upper right panel).

The best-fitting parameters are given in Table 4.2. The systemic velocity of 97 km s⁻¹ is in good agreement with the values measured by Hunter et al. (2001) and Thuan et al. (2004) (99 and 101 km s⁻¹, respectively). We derived an inclination of 64° and a position angle of 45° in comparison to $i = 65^\circ$ and $PA = 46^\circ$ published by Hunter et al. (e.g., 2001). Our derived rotation velocity of 50 km s⁻¹ is also in very good agreement with the values measured, e.g., by Hunter et al. (2001) of 47 km s⁻¹.

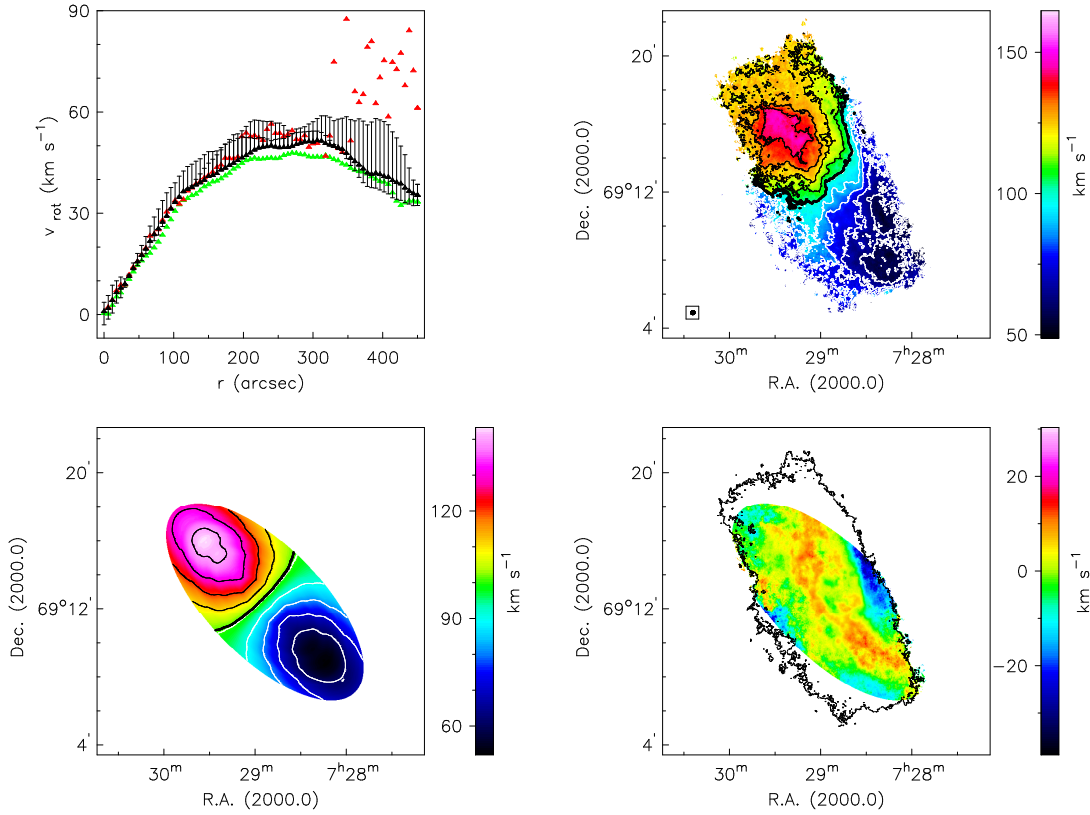


FIG. 4.6: The H I kinematics of NGC 2366. **Top left:** Different approaches were chosen for deriving the rotation curve. The black symbols represent the best-fitting parameters, the error bars indicate receding and approaching side, respectively. The green curve was derived by taking the initial estimates and keep them fixed, the red curve by taking the best-fitting parameters and let them vary. **Top right:** The observed H I velocity field. **Bottom left:** The model velocity field, based on the best-fitting parameters. **Bottom right:** The residual map after subtracting the model from the original velocity map. The outermost H I intensity contour at $0.005 \text{ Jy beam}^{-1}$ is overlaid in black.

In order to prove the reliability of the derived parameters, a model velocity field with the best-fitting parameters was created using the GIPSY task *velfi* (Fig. 4.6, lower left panel) and subtracted from the original velocity map (upper right panel). The residual map can be seen in Fig. 4.6 lower right panel. Overlaid in black is the outermost H I intensity contour. The overall velocity field is well represented by our derived parameters except for the outer parts in the north-west and south-east. Here, the residuals reach values of more than 20 km s^{-1} in comparison to a general value of $\pm 10 \text{ km s}^{-1}$. The north-western part could not be fitted with this model.

4.4.3 A comparison of the neutral and ionised gas

The H α velocity field (see Fig. 4.5) shows two major deviations from the overall rotation velocity, a red-shifted component in the north-west of the GEHR and a blue-shifted one north of the GEHR.

As a next step, the H I image is subtracted from the H α velocity field. Therefore, the FP data were smoothed to fit the H I spatial resolution of $13'' \times 12''$. The residual map is shown in Fig. 4.7, left panel. At most positions, the velocities of the neutral and ionised gas are in good agreement with offsets of less than $\pm 10 \text{ km s}^{-1}$. The huge red-shifted outflow clearly stands out with an expansion velocity of

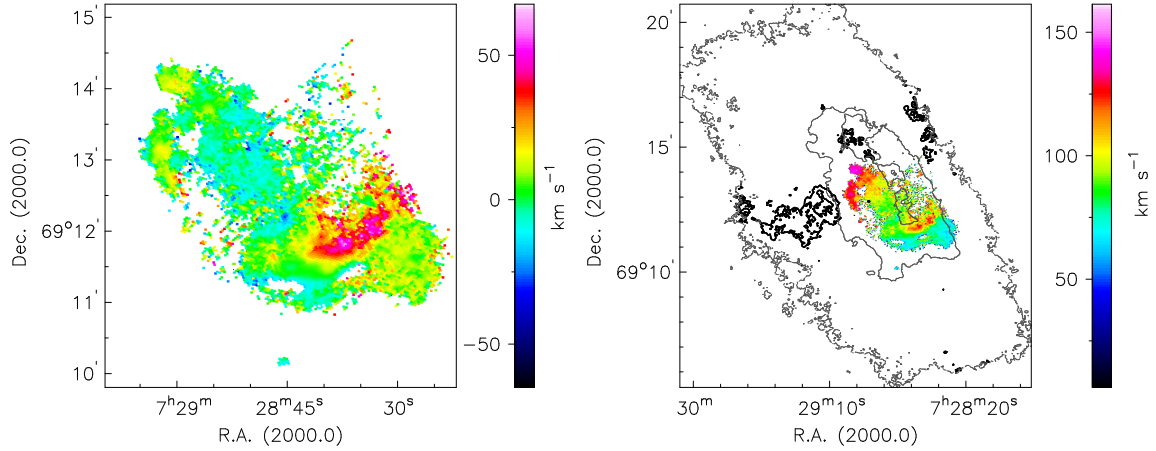


FIG. 4.7: A comparison of the neutral and ionised gas. The left panel shows the residuals after subtracting the H I velocity map from the H α velocity map. The right panel is a representation of the H α velocity map with the H I dispersion of 20 and 25 km s⁻¹ shown as black contours. In grey two contours of the H I intensity distribution are shown to indicate the H I extent.

up to 50 km s⁻¹. In comparison to the H II regions in the south, the whole northern part except for the spiral arm seems to have an underlying blue-shifted component with an offset maximum of 30 km s⁻¹ and a medium offset of 15 km s⁻¹. This expanding gas could already be seen on the original H α velocity map. It coincides with an area of diffuse and filamentary emission between the GEHR and the northern tail (see Fig. 4.4 right panel). For a detailed catalogue of the single filaments see van Eymeren et al. (2007), their Fig. A.1 and Table A1.

The H I velocity dispersion contours are overlaid over the H α velocity field in Fig. 4.7, right panel. Bold lines represent a velocity dispersion of 20 and 25 km s⁻¹, respectively. For better visualisation, two H I intensity contours at 0.005 and 0.1 Jy beam⁻¹ are drawn in grey. The areas of high H I velocity dispersion are clearly offset from the H α emission.

In order to look closer at the H I kinematics in the area of the expanding ionised gas and to check the regions of high H I velocity dispersion, we performed a Gaussian decomposition (see App. A). The result is shown in Fig. 4.8 and some example spectra extracted from the H I cube are given in Fig. 4.9 together with the fitted Gaussian profiles for the single components (long-dashed blue and red lines) and the resulting sum (long-dashed green lines). The velocities were averaged over one beam size, which is in this case 12'' in both spatial directions. The strongest components are presented in the middle panel. Overlaid in white are the H I velocity dispersion contours at 20 and 25 km s⁻¹ and the outer H α intensity contour in black. For a comparison, the blue- and red-shifted components are shown on the left and right panel. Note that regions where we did not find a blue- or redshifted component were filled with the main component. An enlargement of SB4 and the GEHR shows Fig. 4.10. Overlaid over the three H I velocity components are some of the H α intensity contours. The superbubble SB4, the supergiant shell SGS1 (see van Eymeren et al. 2007) and the outflow OF are marked.

As already mentioned in Sect. 4.3, the huge outflow north-west of the GEHR expands into an area of low column density. The H I velocity maps in Fig. 4.10, lower row show no line-splitting, which can also be seen by looking at a spectrum in this area (Fig. 4.9, panel d). Only close to the origin

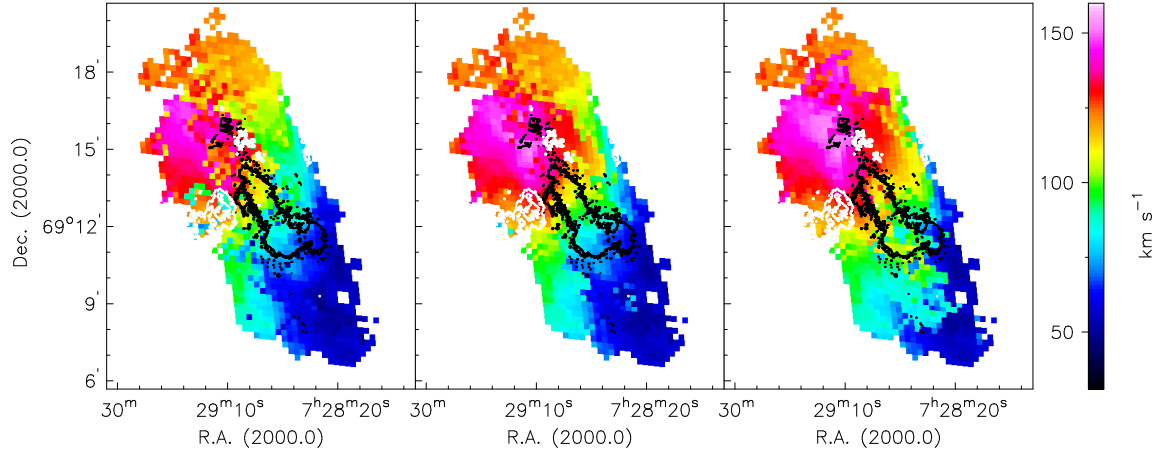


FIG. 4.8: Gaussian decomposition of the HI. Blue-shifted (left panel), main (middle panel) and red-shifted (right panel) components of the HI velocities are shown. Overlaid in white are the HI velocity dispersion contours at 20 and 25 km s^{-1} as well as the outermost $\text{H}\alpha$ intensity contour in black.

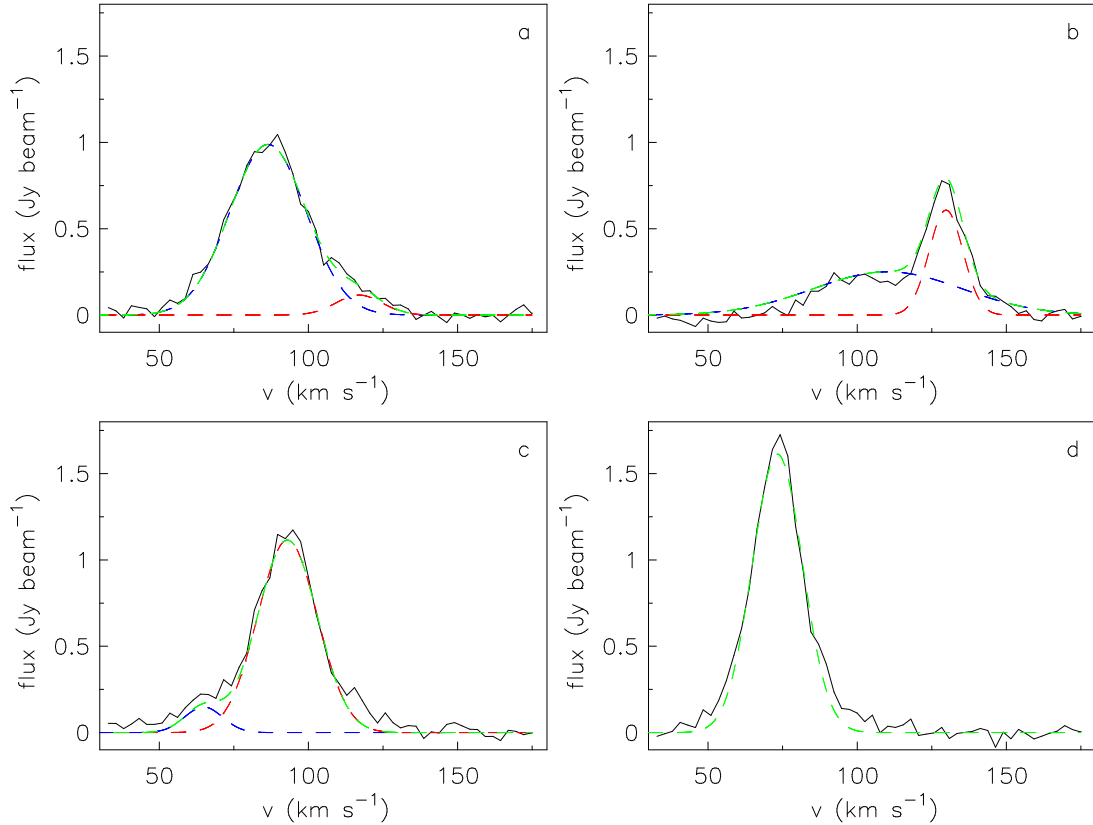


FIG. 4.9: Some example HI line profiles. **(a)** The eastern ridge with an additional red-shifted component. **(b)** The western ridge with an additional blue-shifted component. **(c)** A hint of the blue-shifted component north of the GEHR with $v_{\text{helio}} = 65 \text{ km s}^{-1}$. **(d)** The red-shifted outflow north-west of the GEHR with $v_{\text{helio}} = 130 \text{ km s}^{-1}$ cannot be detected in HI. The Gaussian profiles fitted to the single components are plotted in blue and red, the resulting sum of the profiles is overlaid in green.

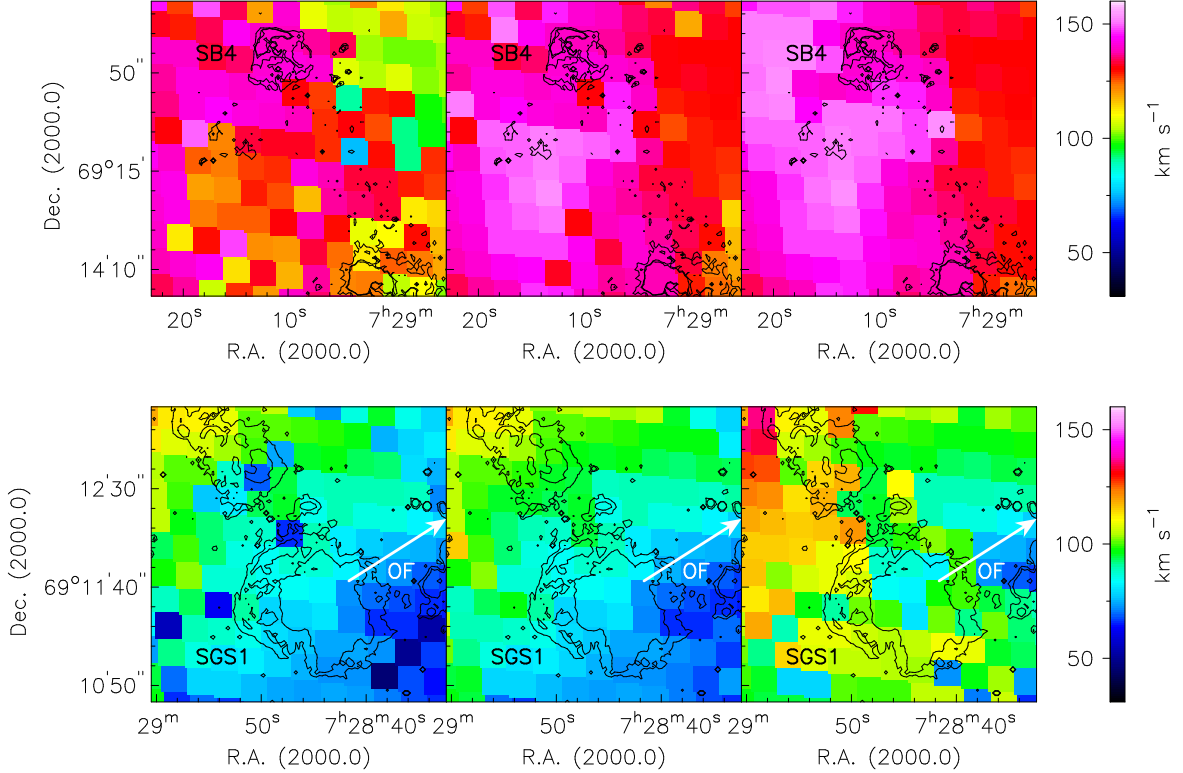


FIG. 4.10: An enlargement of the central region of NGC 2366. The upper row shows the superbubble SB4 and its surroundings, the lower row presents the GEHR and the onset of the northern tail. Again the three H I velocity components are plotted. Overlaid in black are the $H\alpha$ intensity contours. SB4, the supergiant shell SGS1 (see van Eymeren et al. 2007) and the outflow OF are marked.

of the outflow, a second component appears in the H I line profile. With a velocity of 100 km s^{-1} in comparison to the outflow velocity of 130 km s^{-1} , it is most probably not connected to the outflow.

SB4 has also no counterpart in H I (see Fig. 4.10, upper row). The same is true for SGS1 (lower row). Line-splitting of the H I emission takes place in the north-eastern part of the GEHR going to the south, which is probably due to the existence of the eastern spiral arm. This is discussed in more detail in Sect. 4.5.3.

Finally, a hint of the underlying blue-shifted component detected on the $H\alpha$ velocity map (see Fig. 4.5) is also visible in H I with the same velocity of 65 km s^{-1} (see Fig. 4.9, panel (c)).

4.5 Discussion

We have seen that the $H\alpha$ line emission in NGC 2366 is sometimes split into several components, in one case also corresponding to a line-splitting in H I. We also found line-splitting in H I outside the optical disk along two parallel ridges. In the following subsections, we try to explain detections and also non-detections and deal with the important question what the fate of these outflows is.

4.5.1 The outflows

Two major outflows were found on the $H\alpha$ velocity field. The huge red-shifted outflow expanding from the GEHR to the north-west is not detected on the $H\text{I}$ velocity map, whereas the blue-shifted outflow north of the GEHR has a counterpart in $H\text{I}$. Additionally, we see shell-like structures (SGS1, SB4) on the $H\alpha$ image with no kinematic evidence on the $H\text{I}$ map. Resolution effects cannot be responsible for the non-detection as the structures cover a field of several beam sizes. Unfortunately, we cannot trace them on the $H\alpha$ velocity map as SB4 lies outside the field of view and SGS1 is covered by artificial emission (see Chap. 2).

Coming back to the kinematically detected outflows the question rises why the blue-shifted outflow is detected both in $H\alpha$ and $H\text{I}$ with very similar velocities, whereas the red-shifted outflow is only detected in $H\alpha$. This is probably an effect of age and energy input. Considering their position in the galaxy, it can be assumed that both outflows have a different origin. The huge red-shifted outflow is most probable driven by the two large star clusters in the GEHR (Drissen et al. 2001), whereas the blue-shifted gas might get its energy from a star cluster north of the GEHR. This star cluster might be younger and smaller than the ones in the GEHR so that the energy input is not sufficient or has not been sufficient, yet to fully ionise the surrounding neutral gas. The ionised gas expands into the neutral medium, but instead of ionising it, it just moves the neutral gas outwards. We can only detect a blue-shifted component, which does not mean that there is not a red-shifted component, too. It always depends on the column density whether we can see the gas or not. In this case, it could be possible that the blue-shifted gas runs into an area of higher column-density, whereas the red-shifted part expands into an area of low column density. The same could be true for the huge, red-shifted outflow. In this case, we do not see a blue-shifted component in $H\alpha$ and we do not see any counterpart in $H\text{I}$. Possibly, the energy input is so strong that all the gas was immediately ionised, e.g., by shock heating. The expansion velocities are almost twice the velocities of the blue-shifted gas. The low $H\text{I}$ column density in comparison to its surroundings also indicates that here, larger amounts of neutral gas have already been ionised.

4.5.2 Superbubble blowout in NGC 2366?

As already mentioned in Sect. 4.4.1, Roy et al. (1991) observed the central part of NGC 2366, which was mainly the GEHR NGC 2363, with a Fabry-Perot interferometer. Next to the huge outflow they also reported the detection of an expanding superbubble around NGC 2363 with an expansion velocity of 45 km s^{-1} . Echelle spectroscopy of the central region performed by Martin (1998) and van Eymeren et al. (2007) revealed neither a blue- nor a red-shifted component around NGC 2363. The bubble is also not visible on the $H\text{I}$ velocity field (see Fig. 4.10). In Sect. 2.5, an artefact of the FP interferometer was explained which is caused by blurring inside the detector, which leads to an artificial velocity gradient on very bright emission line regions. Figure 2.8 shows that this blurring leads to a velocity gradient from -90 km s^{-1} to 120 km s^{-1} within 1 kpc, which is unphysical in comparison to the slowly rising velocity gradient in the other parts of the galaxy and which cannot be observed in $H\text{I}$. Assuming that this gradient comes from true emission, its interpretation as an expanding superbubble is indeed intimidating. Therefore, we suppose that most probably, Roy et al. (1991) interpreted an artefact as a real expanding bubble as they were not aware of the technical problem of blurring inside the detector. The non-detections of Martin (1998), van Eymeren et al. (2007) and also of Thuan et al. (2004) in $H\text{I}$ give further support of the non-existence of this superbubble.

4.5.3 Spiral arm structure revisited

Stellar HST photometry (Tikhonov & Galazutdinova 2008) and our optical observations (see Chapter 3) reveal two weak spiral arms in NGC 2366, one on the eastern part of the stellar disk and one on the western side (Fig. 3.1). In $H\alpha$, the spiral arms can be traced by an alignment of small H II regions at large distances from the disk. Looking again at the enlarged view of the centre (Fig. 4.4), we see H I maxima in the column density that follow exactly the way of the spiral arms out of the disk. This could indeed be explained as a concentration of neutral gas formed by a density wave going through the galaxy. All along the spiral arms, the H I line is split into two components, which has already been mentioned by, e.g., Thuan et al. (2004). A closer look at the H I velocities (Fig. 4.8) shows that next to the main component, a red-shifted component runs along the eastern arm to the south and a blue-shifted component along the western arm to the north (see also the example spectra in Fig. 4.9, panels a and b). The eastern arm crosses the supergiant shell SGS1. As the red-shifted component is visible on large scales, it is unlikely that we can see an additional red-shifted component belonging to the SGS1.

In contrast to former H I studies by Hunter et al. (2001) and Thuan et al. (2004), we conclude from our results that the H I data give us even stronger evidence that NGC 2366 has two spiral arms.

4.5.4 Outflow or galactic wind?

We found two main expanding gas structures in NGC 2366. One is only visible in $H\alpha$ with an expansion velocity of 50 km s^{-1} , the other one shows similar expansion velocities in $H\alpha$ and H I of 30 km s^{-1} . We now want to make some statements about the fate of the gas by comparing the expansion velocities to the escape velocity of the galaxy.

van Eymeren et al. (2007) have already tried to model the escape velocities of dwarf galaxies by using the NFW halo model. However, several studies show that the NFW halo does not represent the observed density profiles of dwarfs very well, especially in the inner 1 to 2 kpc where we found the structures. Cold Dark Matter simulations by, e.g., Navarro et al. (1996) and Moore et al. (1998, 1999) predict a cuspy core, whereas observations find a core of constant density in the inner parts of rotation curves (e.g., de Blok & Bosma 2002). This so-called cusp-core discrepancy is addressed in more detail in Chap. 7. Recent publications by, e.g., Kuzio de Naray et al. (2008) and Spano et al. (2008) show that the rotation curves of dwarf and low surface brightness galaxies can better be described by a pseudo-isothermal (ISO) halo (Binney & Tremaine 1987), at least in the inner few kpcs. The ISO halo is an empirically derived description of a dark matter halo. Its density profile is given by

$$\rho_{\text{ISO}}(r) = \rho_0 \left(1 + \left(\frac{r}{r_c} \right)^2 \right)^{-1} \quad (4.1)$$

with ρ_0 being the central density and r_c the core radius. The escape velocity is then given by

$$v_{\text{esc}}(r) = \sqrt{2 v_c^2 \left(1 + \log \left(\frac{r_{\text{max}}}{r} \right) \right)} \quad (4.2)$$

with v_c being the circular velocity and r_{max} being the maximum radius of the dark matter halo (see Binney & Tremaine 1987).

As mentioned above, the ISO halo represents the observations much better than the NFW halo. Therefore, we decided to model the ISO halo as the outflows are generally close to the dynamical centre. The result is shown in Fig. 4.11. The H I rotation curve including receding and approaching

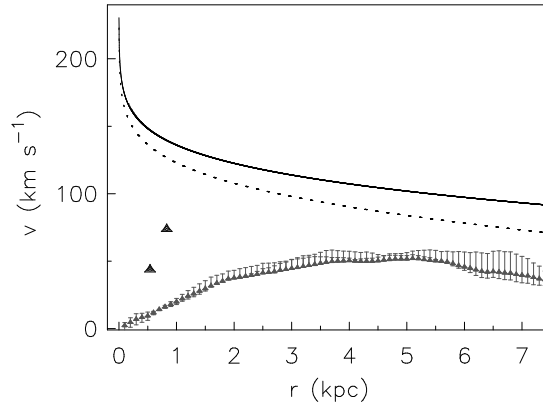


FIG. 4.11: Escape velocity for a pseudo-isothermal halo of $r_{\max} = 7.5$ kpc (dotted line) and $r_{\max} = 15$ kpc (solid line). The observed rotation curve is indicated by small grey triangles. The error bars represent receding and approaching side. The expanding gas structures are marked by black large triangles.

side is indicated by small grey triangular-shaped symbols. The expanding gas structures are marked by black large triangles. We corrected the values for an inclination of 64° as calculated in Sect. 4.4.2, which leads to an increase in velocity of about 10%. The circular velocity was measured from the rotation curve to be 50 km s^{-1} (see Table 4.4.2). We plotted the escape velocity for two different radii $r_{\max} = 7.5$ kpc (dotted line) and $r_{\max} = 15$ kpc (solid line). The lower value of r_{\max} was chosen to equal the size of the HI distribution. Most probably, the dark matter halo is much larger so that we get a lower limit for its size by taking the HI radius. The second value was chosen to be twice the size of the HI radius, which might still be too small to describe the size of the dark matter halo. Nevertheless, a higher r_{\max} increases the escape velocities, which means that all radii larger than the HI radius decrease the probability of a galactic wind so that taking the HI radius as r_{\max} can be regarded as a lower limit for the escape velocity.

Both outflows have expansion velocities that lie clearly below the escape velocity. As the ISO halo is characterised by a core of constant density, the escape velocities in the inner parts are even higher than by using a rapidly decreasing NFW density profile.

4.6 Summary

Fabry-Perot interferometry and HI synthesis observations were performed to compare the morphology and the kinematics of the neutral and ionised gas component in the nearby irregular dwarf galaxy NGC 2366.

We found a huge red-shifted outflow in $\text{H}\alpha$ with an expansion velocity of 50 km s^{-1} , which has been detected before by Roy et al. (1991) and van Eymeren et al. (2007). The FP data allow us for the first time to see the whole extent of the outflow. With a length of 1.4 kpc it is one of the largest outflows found so far in dwarf galaxies. This outflow as well as the supergiant shell SGS1 and the superbubble SB4 do not have a counterpart in HI and they expand into an area of low HI column density. The northern part of the galaxy shows an underlying blue component with a velocity offset of 30 km s^{-1} in $\text{H}\alpha$, which is also visible in HI. We suggest that in case of the red-shifted outflow and the shell structures, the neutral gas is already fully ionised, which indicates that either the star cluster responsible for the ionisation is older than in case of the blue-shifted component or its energy input is higher.

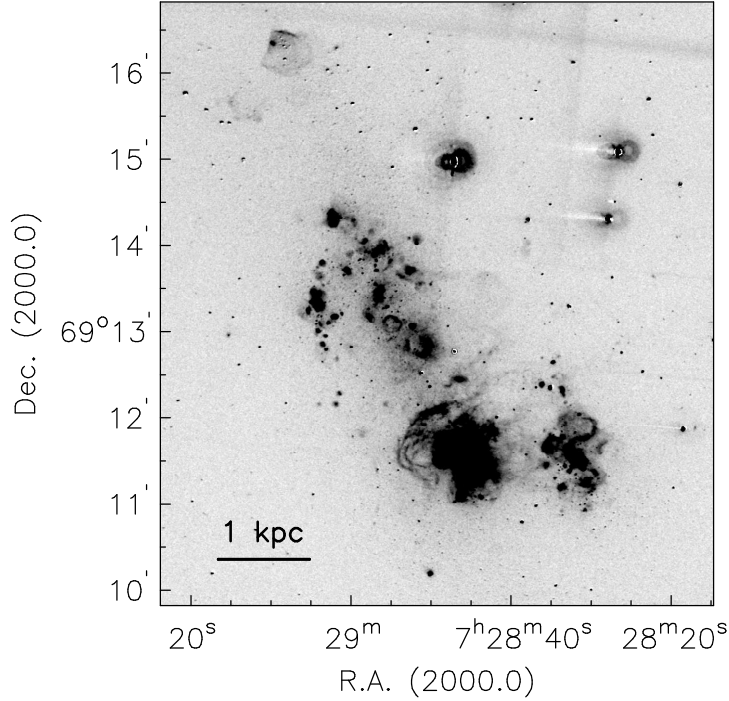


FIG. 4.12: Continuum-subtracted $H\alpha$ image of NGC 2366. The contrast is chosen in a way to demonstrate the small-scale structures.

Nevertheless, a comparison of the measured expansion velocities with the escape velocity of the galaxy, calculated from a pseudo-isothermal halo model, reveals that in all cases and independent of the choice of r_{max} , the expansion velocities of the outflows stay far below the escape velocity, which means that the gas is still gravitationally bound and would need substantial amounts of energy to be accelerated to the escape velocity.

4.A Appendix: $H\alpha$ image and extension of the catalogue of ionised gas structures

Here, the continuum-subtracted $H\alpha$ image is again presented in an enlarged version and with a different contrast as in Fig. 4.1 to emphasise the small-scale structure (see Fig. 4.12). Additionally, the catalogue of van Eymeren et al. (2007) is extended by the superbubbles in the northern tip of the galaxy.

TABLE 4.3: The most prominent structures and their sizes in NGC 2366 – an extension –.

Source	Diameter [$''$]	Diameter [pc]	v_{helio} [km s^{-1}]	FWHM [km s^{-1}]
SB4	30	500	-	-
SB5	25	417	-	-

A comparison of the neutral and ionised gas kinematics in the irregular dwarf galaxy NGC 4861

Abstract

Outflows powered by the injection of kinetic energy from massive stars can strongly affect the evolution of galaxies, in particular of dwarf galaxies as their lower gravitational potentials enhance the probability of a galactic wind.

Fabry-Perot as well as H I synthesis data of the nearby irregular dwarf galaxy NGC 4861 were obtained in order to search for outflowing gas structures by comparing the morphology and the kinematics of the neutral and ionised gas component.

Both in H I and H α the galaxy shows several outflows, two directly connected to the disk and one at kpc-distance from the disk. We measured expansion velocities of 20 to 30 km s⁻¹, which were subsequently compared to the escape velocity of the galaxy by using the pseudo-isothermal halo model in order to make some statements about the fate of the gas. We found that the expansion velocities stay far below the escape velocity minimising the probability of a galactic wind.

NGC 4861 is accompanied by a small H I cloud located east of the main body. We found that this cloud is rotating, but has no stellar counterpart on deep optical images. An interpretation as a dark galaxy can therefore not be ruled out.

5.1 Introduction

Irregular dwarf galaxies can be the sites of giant star formation regions. The feedback between massive stars and the interstellar, on larger scales also the intergalactic medium is one of the most important processes in the evolution of these galaxies. Kinetic energy and momentum are injected into the interstellar medium (ISM) by stellar winds of, e.g., Wolf-Rayet stars and by supernovae explosions. This leads to numerous ionised gas structures in and around the galactic plane (see, e.g., Bomans et al. 1997; van Eymeren et al. 2007). However, ionised gas also exists at kpc distances away from any place

of current star formation (Hunter et al. 1993). In this case, the ionisation mechanisms are not obvious. Shock waves that are driven by a concentration of massive stars may sweep the interstellar gas out of the star forming region, which leads to the formation of a cavity. Due to lower densities than usual in the ISM, the photons can travel larger distances and can ionise much more distant neutral gas (e.g., Hunter & Gallagher 1997). Apart from photoionisation and shock ionisation, turbulent mixing layers (Slavin et al. 1993) and magnetic reconnection (Birk et al. 1998) are additional, possible excitation mechanisms.

Another issue that has to be discussed is the fate of these structures. Does the gas stay gravitationally bound to its host galaxy or is the energy input large enough to accelerate the gas to velocities beyond the escape velocity of the galaxy, which means that the gas might leave the gravitational potential and enrich the IGM? This question is the basis of several models and simulations. Especially the simulations by Mac Low & Ferrara (1999) show that at least in low mass galaxies, the probability rises that the gas escapes from the gravitational potential.

NGC 4861 is classified as an SB(s)m galaxy, although it shows no evidence for spiral structure (Wilcots et al. 1996). It is dominated by a Giant Extragalactic H II region (GEHR) in the southwest, IZw 49, where most of the star formation occurs. A chain of small H II regions extends to the north-east forming a tail and therefore giving the galaxy a cometary-shaped appearance. High-resolution longslit echelle spectra centred on the H α line of this galaxy were recently analysed by us (van Eymeren et al. 2007). We found a huge expanding bubble around the GEHR, the blue-shifted component having a velocity of about 110 km s⁻¹ and the red-shifted component having a velocity of about 60 km s⁻¹. The galaxy has also been studied in H I by Wilcots et al. (1996) as well as by Thuan et al. (2004). They report the detection of a small H I cloud at a deprojected distance of 4 kpc east from NGC 4861 that appears to have no optical counterpart.

In this paper, we search for outflowing gas both in H α and H I in NGC 4861. So far, studies usually concentrated either on the neutral gas by performing radio synthesis observations (e.g., Thuan et al. 2004) or on the ionised gas component by performing long-slit spectroscopy (e.g., Hunter & Gallagher 1997; Martin 1998; van Eymeren et al. 2007). One of the major problems of long-slit spectroscopy is the limited field of view. This changed only during the last decade with the advancement of the so-called 3d spectroscopy. For our optical observations, we used a scanning Fabry-Perot interferometer centred on the H α line that provides us with a complete spatial coverage of NGC 4861 and relevant spectral information. For our H I analysis, we combined the VLA D array data by Wilcots et al. (1996) with the VLA C array data published by Thuan et al. (2004). We added another VLA C array data set obtained by us to improve *uv*-coverage and sensitivity (for details see Table 5.1).

This chapter is organised as follows: The observations and the data reduction are described in § 5.2. Section 5.3 compares the morphology of both gas components, § 5.4 presents a kinematic analysis. In § 5.5, the results are discussed and § 5.6 summarises the main results.

5.2 Observations and data reduction

5.2.1 The Fabry-Perot data

Fabry-Perot (FP) interferometry of the irregular dwarf galaxy NGC 4861 was performed on the 28th of February 2006 at the 1.93m telescope at the Observatoire de Haute-Provence, France. We used the Marseille's scanning FP and the new photon counting camera (Gach et al. 2002). The field of view is 5'8 × 5'8 on the 512 × 512 pixels of the detector and is slightly limited by the interference filter to 5'5 × 5'5, which gives a spatial resolution of 0'68 per pixel. The H α line was observed through

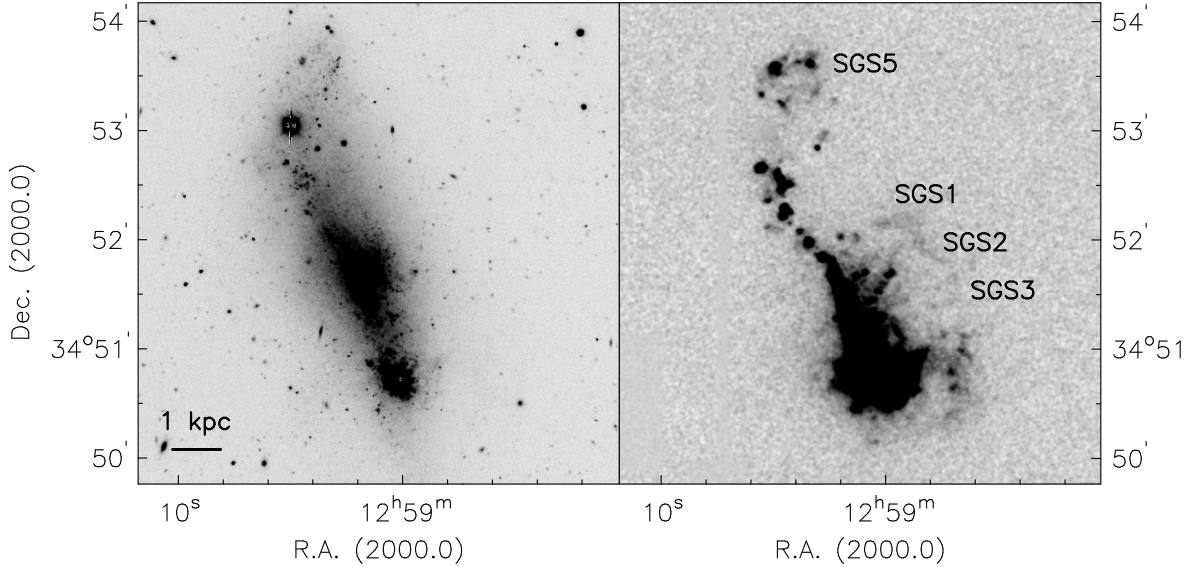


FIG. 5.1: R -band image (left panel) and continuum-subtracted $H\alpha$ image (right panel) of NGC 4861. The three supergiant shells are numbered according to van Eymeren et al. (2007). In order to stress weaker structures and to differentiate them from the noise, we used adaptive filters based on the H-transform algorithm (Richter et al. 1991, see App. B)

an interference filter centred at the galaxy’s rest wavelength of 6581 \AA with a FWHM of 10 \AA . The free spectral range of the interferometer – 376 km s^{-1} – was scanned through 24 channels with a sampling step of 15 km s^{-1} . The final spectral resolution as measured from the night sky lines is about 50 km s^{-1} . The seeing was about $3''$ to $4''$.

In total, NGC4861 was observed for 172 min. We used a neon lamp for the phase and wavelength calibration. The data reduction was done using the software ADHOC¹, written by Jacques Boulesteix. A Gaussian decomposition was performed by interactively fitting the emission (IRAF task *splot*, for a detailed description see App. A). Only detections above a 3σ limit were considered. In order to match the seeing and to improve the signal to noise ratio, we afterwards summed over 3×3 pixels. All given velocities are heliocentric velocities measured along the line of sight.

Further details about the FP technique, the observations and the data reduction process can be found in Chap. 2.

5.2.2 Optical imaging

We obtained a 900 s R -band image with the WIYN 3.5m telescope at Kitt Peak. Additionally, we observed the area around the H I cloud, also with an integration time of 900 s, in R . In order to expand the search for an optical counterpart of the H I cloud, we obtained a 90 min V -band image with the 2.2m telescope at Calar Alto equipped with CAFOS on the 3rd of March 2008. A standard data reduction was performed for all data using IRAF. We use an $H\alpha$ image which is part of the “Palomar/Las Campanas Imaging Atlas of Blue Compact Dwarf Galaxies” by Gil de Paz & Madore (2005). The R -band and $H\alpha$ images of NGC 4861 are shown in Fig. 5.1.

¹<http://www.oamp.fr/adhoc/>

TABLE 5.1: The VLA H I observations.

Parameters [Unit]			
Date	11.04.92	12.12.94	17.01.94
Configuration	C	C	D
Integration Time [min]	266	120	56
Flux calibrator	3C 286	3C 147	3C 147
Phase calibrator	3C 286	3C 147	3C 147
Bandwidth [MHz]	1.56	1.56	1.56
Channel Width [km s ⁻¹]	2.6	2.6	5.2
H I synthesised beam (na) of the combined data:			31'' × 30''

5.2.3 The H I data

The data were obtained with the VLA in its C and D configuration. All data were calibrated using the software package AIPS. For further information about the observing technique and the data reduction process see Wilcots et al. (1996) and Table 5.1. We complemented the data by an archival VLA C array data set in order to improve the sensitivity and the uv-coverage. It was also calibrated by us using AIPS. In all data cubes, the continuum was averaged over the line-free channels to form a single continuum map that was afterwards subtracted from each channel.

For the analysis, all three data sets were combined taking into account the different pointings. The task *invert* in the software package MIRIAD is very well suited for mosaicing data so that we combined, inverted, cleaned and restored the cube in MIRIAD. Figure 5.2 shows the H I channel maps after applying a standard Hanning smoothing, superimposed on a greyscale presentation of our *R*-band image. The white cross in the first channel marks the optical centre of the galaxy. The beam is placed into the lower left corner of the same channel. The corresponding heliocentric velocities are indicated in the upper right corner of each channel map.

In order to create the moment maps (for a more detailed description see App. C) and to analyse the H I data, the software GIPSY² was used.

5.3 General morphology

The *R*-band and the H α images are shown in Fig. 5.1. The galaxy has a very similar shape as NGC 2366. The H α luminosity is dominated by a GEHR in the south. A chain of smaller H II regions extends to the north-east ending with a ring-like structure at the northernmost tip. Comparable to SB4 in NGC 2366, it is located at the outer edge of the star distribution. However, no star cluster seems to be associated with it in contrast to SB4. With a diameter of 1018 pc, it belongs to the large-scale structure of this galaxy. Following the classification and numbering of van Eymeren et al. (2007), it is catalogued as SGS5 (see Table 5.3 in App. 5.A). Next to the large-scale structure (see also the supergiant shells in Fig. 5.1, right panel), Fig. 5.14 in App. 5.A shows an enlargement of the continuum-subtracted H α image that emphasises the small-scale structure close to the disk. Most of the filaments can be found on the western side of the galaxy.

²The Groningen Image Processing System

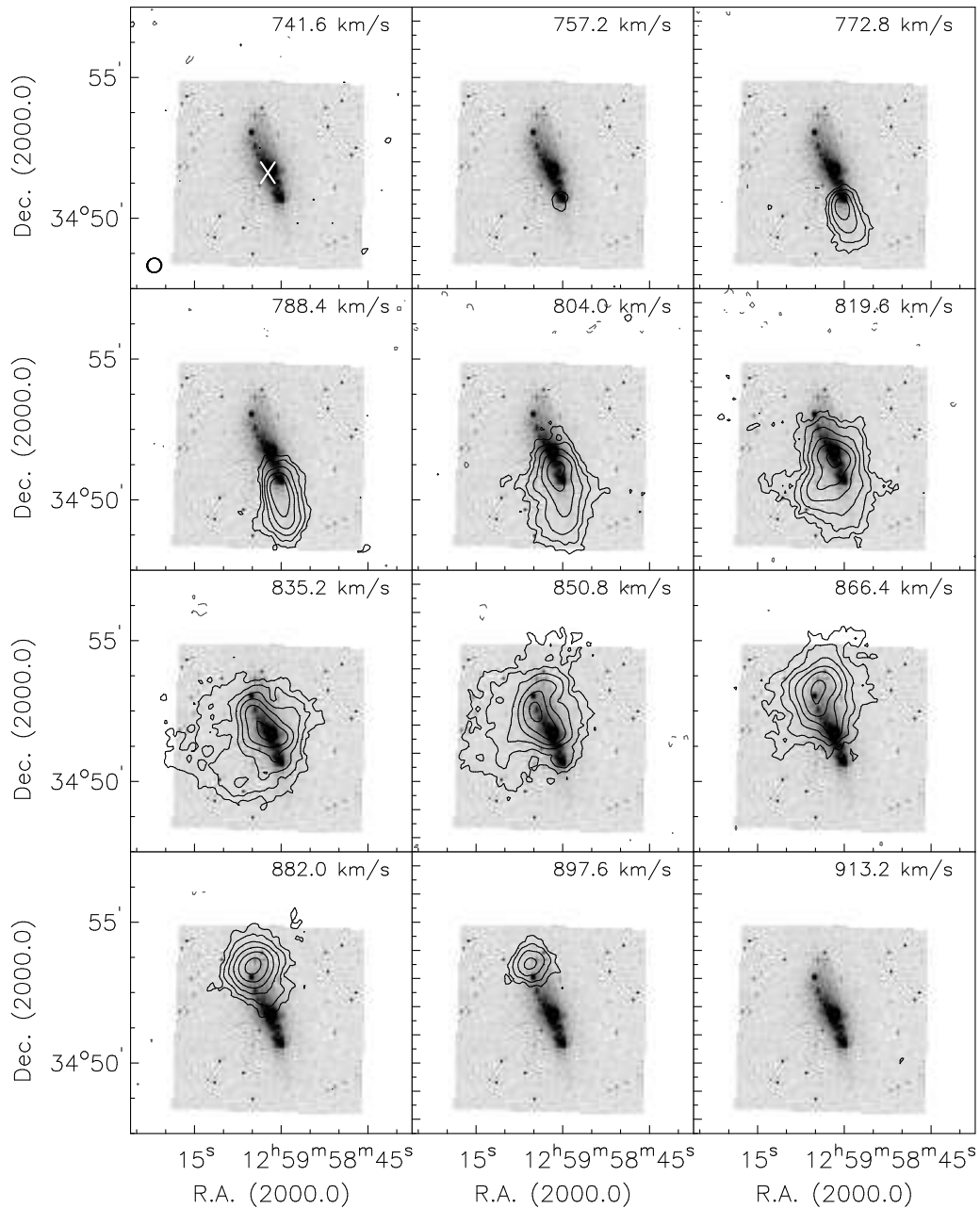


FIG. 5.2: H I channel maps of NGC 4861 (contours) as obtained from the VLA using natural weighting of the data, superposed on the *R*-band image. Contours are drawn at -1.5 (-3σ), 1.5 (3σ), 3 , 6 , 12 , 24 and 48 mJy beam^{-1} . The synthesised beam is displayed in the lower left corner of the first channel map. The optical centre of the galaxy is marked by a white cross in the same channel map. The corresponding heliocentric velocities are indicated in the upper right corner of each channel. A standard Hanning smoothing was applied to the cube. The original channel spacing is 5.2 km s^{-1} .

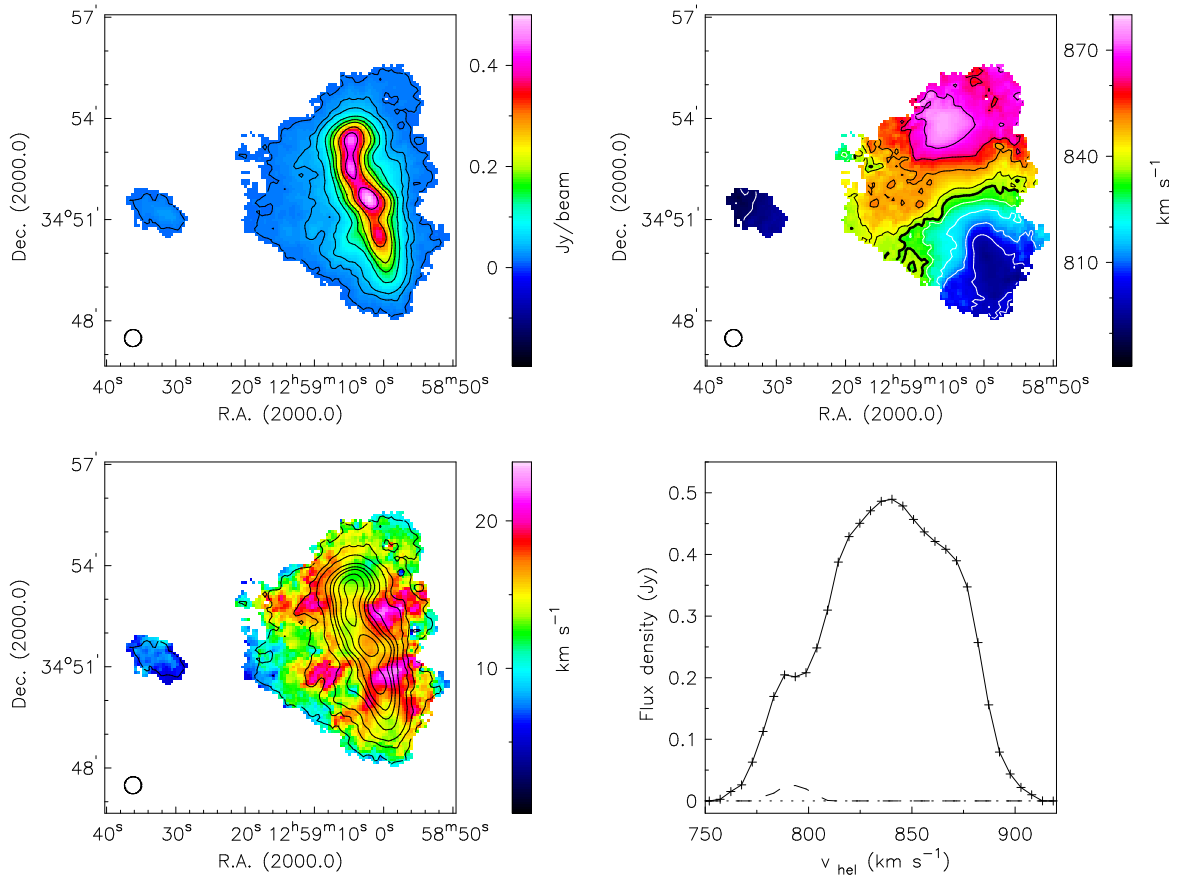


FIG. 5.3: The H I moment maps of NGC 4861 using “natural” weighting, which leads to a synthesised beam of $31'' \times 30''$. **Top left:** The H I intensity distribution. Contours are drawn at 0.01, 0.03, 0.05, 0.1, 0.15, 0.2, 0.3, 0.4 Jy beam^{-1} where 10 mJy beam^{-1} correspond to a column density of $1.6 \times 10^{21} \text{ atoms cm}^{-2}$. **Top right:** The H I velocity field. Contours are drawn from 790 to 870 km s^{-1} in steps of 10 km s^{-1} . The systemic velocity of 835 km s^{-1} is marked in bold. **Bottom left:** The velocity dispersion, overlaid are the same H I intensity contours as on the 0th moment map. **Bottom right:** The global intensity profile of the galaxy (solid line) and the H I cloud (long-dashed line). The short-dashed line marks zero intensity.

The corresponding H I intensity distribution is displayed on the upper left panel of Fig. 5.3. The H I emission is much more extended than the optical extent of the galaxy forming a symmetric distribution, except for the eastern part, with several maxima along the north-south axis. The distortion in the east is most probably due to the small H I cloud.

We now compare the morphology of the ionised and neutral gas by plotting the H I intensity contours over the continuum-subtracted $\text{H}\alpha$ image (see Fig. 5.4). The left panel shows that the optical galaxy lies in the centre of the H I distribution. The H I intensity maxima all coincide with the optical extent. Similar to NGC 2366, the H I maximum coinciding with the GEHR is offset to its centre. Again, the shift is larger than one beam size and therefore not a resolution effect. The other three H I maxima coincide with several of the smaller H II regions along the tail. Close to the supergiant shells SGS1, SGS2 and SGS3 as well as east of the GEHR, the gradient of the intensity decrease is different from the overall gradient. In both cases, the gradient is flatter, which means that the gas density is higher than in the surroundings. This might indicate outflowing gas and indeed, the kinematic analysis below will show that these two regions harbour expanding structures.

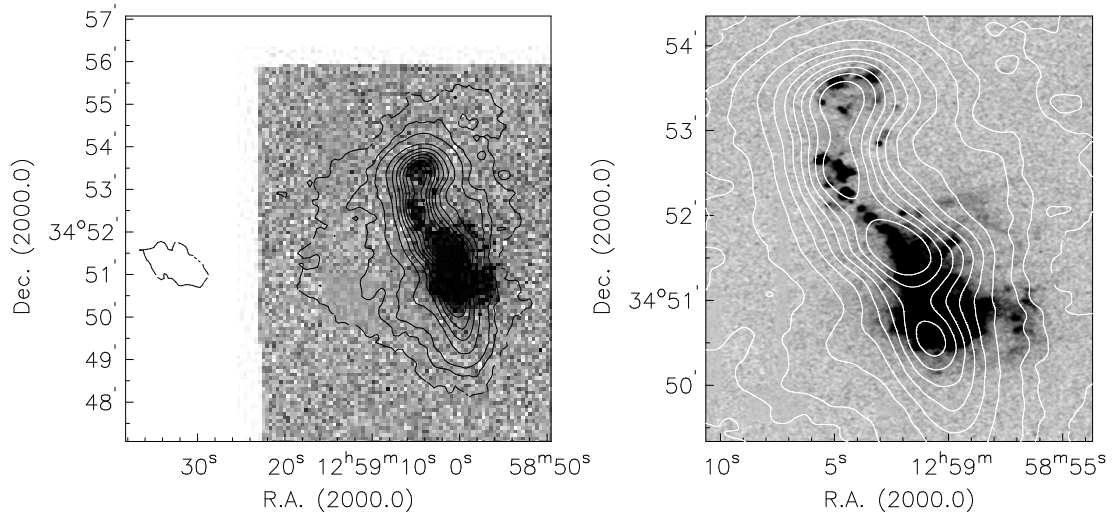


FIG. 5.4: A comparison of the H α and the H I morphology. The left panel shows the continuum-subtracted H α image. Overlaid in black are the H I intensity contours at 0.01, 0.03, 0.05, 0.1, 0.15, 0.2, 0.25, 0.3, 0.35, and 0.4 Jy beam⁻¹. The right panel displays an enlargement of the optical part. The H I intensity contours are overlaid in white.

5.4 Kinematic analysis

We have shown that the H I distribution is very symmetric except for a distortion in the east, most probably caused by an H I cloud, and that the H I maxima trace the main H II regions from the GEHR in the south along the tail of smaller H II regions to the north. Additionally, we have already found indications for outflowing gas. We now want to look at the kinematics of the neutral and ionised gas and to search for expanding gas structures.

5.4.1 H α velocity field

The Gaussian decomposition reveals that at several places, the H α line consists of more than one component, which is an indication for expanding gas structures. Figure 5.5 shows the resulting velocity map with the component of highest intensity plotted. The overall velocity gradient runs from the south-west with velocities of about 800 km s⁻¹ to the north-east with velocities of about 870 km s⁻¹. This fits well with the systemic velocity calculated from the H I data of about 835 km s⁻¹ (see below) and gives the ionised gas a rotation velocity of 35 km s⁻¹.

Several deviations from the overall rotation become immediately visible: first, there is a blue-shifted component in the south of the GEHR. On the right panel of Fig. 5.5, we present as an example one of the spectra extracted from this area (black solid line). The H α line is split into two components, one at 760 km s⁻¹ (blue long-dashed line) representing the outflowing gas and one at 820 km s⁻¹ (red long-dashed line) corresponding to the overall velocity gradient. The sum of both Gaussian fits is plotted in green and is in good agreement with the observed spectrum.

Possibly, a red-shifted counterpart can be seen in the north of the GEHR. Along the chain of H II regions to the north-east of the galaxy, slightly red-shifted gas seems to flow out of the disk in the direction of the supergiant shells (SGSs) located in the west (see Fig. 5.1, right panel). These three SGSs are kinematically separated: SGS1 and SGS2 (following the catalogue of van Eymeren et al. 2007) are red-shifted with an expansion velocity of 30 km s⁻¹, whereas SGS3 follows the rotation velocity.

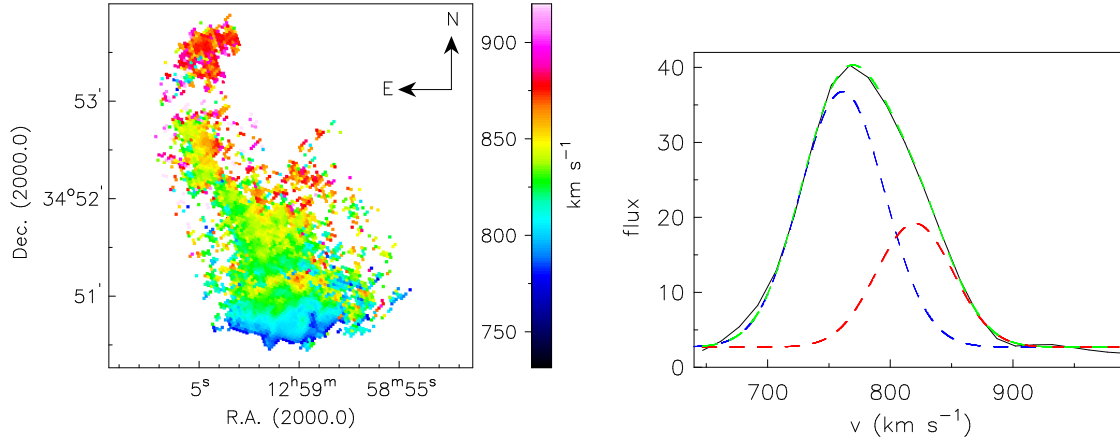


FIG. 5.5: The $H\alpha$ velocity field of NGC 4861. The left panel shows the velocity distribution of the strongest component. The right panel displays one example spectrum (black solid line) at the position of the blue-shifted outflow south of the GEHR which was extracted from the FP data cube. The $H\alpha$ line is split into a component at 760 km s^{-1} (blue long-dashed line) and one at 820 km s^{-1} (red long-dashed line). The sum of both Gaussian fits is plotted in green and is in good agreement with the observed spectrum.

The velocities in the area of SGS5 follow the rotation of the galaxy. We found an indication of a blue- and a red-shifted component with velocity offsets of about 130 km s^{-1} and 110 km s^{-1} in comparison to the main component. This is quite high in comparison to the other outflows and we cannot be sure whether it is true emission or artificial emission, i.e., a ghost of the GEHR (see Sect. 2.5).

5.4.2 H I velocity field

The upper right panel of Fig. 5.3 shows the velocity field which looks fairly regular with a gradient rising from the south-west with velocities of about 795 km s^{-1} to the north-east with velocities of about 870 km s^{-1} . As already mentioned by Wilcots et al. (1996), the isovelocity contours close at both ends of the galaxy, which is an indication for a declining rotation curve. There are two major deviations from the rotation, i.e., the faint eastern part which is perturbed and the small H I cloud in the east which has an offset of about 60 km s^{-1} in comparison to the overall velocity gradient.

The H I velocity dispersion map (Fig. 5.3, lower left panel) shows altogether four peaks, two of them close to H I maxima and therefore coinciding with the optical galaxy and two positioned at the disturbed region to the east. The overlay of the H I intensity contours reveals that the H I maxima are clearly offset from the regions of high dispersion except for the southernmost peak. All four dispersion maxima have velocities of 20 km s^{-1} to 22 km s^{-1} , which is $1/3$ lower than the peak dispersion in NGC 2366. This is not unexpected as the velocity field of NGC 2366 is much more distorted than the one of NGC 4861. The median value lies at 14 km s^{-1} , which is comparable to NGC 2366.

The upper left panel of Fig. 5.6 shows the H I rotation curve of NGC 4861, which was created by fitting tilted-rings to the observed velocity field (for a detailed explanation see App. C). Initial estimates for the relevant parameters are the output of the ellipse fitting task (GIPSY task *ellfit*) and are used as an input for the tilted-ring fits (GIPSY task *rotcur*). The black symbols represent the best-fitting parameters derived in an iterative approach from the initial estimates and combining both sides, the error bars define receding and approaching side. A fit with the initial estimates kept fixed is indicated by the green symbols (fixed approach), a fit with the best-fitting parameters kept free is shown by the red symbols (free approach). In the inner $200''$, the green symbols are in very good

TABLE 5.2: H I properties as measured from the VLA data.

Parameters [Unit]	NGC 4861		NGC 4861 B
	initial estimates	best-fitting values	initial estimates
centre:			
α (J2000.0)	12 ^h 59 ^m 00.7	12 ^h 59 ^m 01.4 ^s	12 ^h 59 ^m 32.6 ^s
δ (J2000.0)	+34° 51' 43"	+34° 51' 43"	+34° 51' 15"
v_{sys} [km s ⁻¹]	840	835	791
i [°]	64	65	65
PA [°]	13	16	244
F_{HI} [Jy km s ⁻¹]		36.08	0.30
M_{HI} [10 ⁸ M _⊙]		4.79	0.04
H I diameter		419" × 294"	98" × 53"
" [kpc]		15.23 × 10.69	3.56 × 1.93
H I / opt. ratio		2.3 × 5	–
v_{rot} [km s ⁻¹]		46	4.4
$\langle \sigma \rangle$ [km s ⁻¹]		14	7
σ_{Peak} [km s ⁻¹]		22.8	9.9
$r_{\text{HI,max}}$ [kpc]		10.9	2.7
M_{dyn} [10 ⁹ M _⊙]		5.4	0.012

agreement with the black ones. From a radius of 200" on, the differences become larger. The red symbols only agree well within a radius of about 150". The reason for this is that the filling factors of the rings drop from about 1 to about 0.5 at a radius of 200", which leads to a higher uncertainty in calculating the rotation velocity. Therefore, every value above 200" has to be treated with care.

In the inner 100", the velocity gradient is very steep and linear, indicating solid body rotation, which is a characteristic sign of dwarf galaxies. Above 100", the curve shows a plateau with a tendency to decline. The new rise at a radius of about 240" is first due to the lower filling factor and resulting higher uncertainties in the velocity calculation. On the other hand, the disturbed gas in the eastern parts of the galaxy also causes a rise in velocity.

The best-fitting parameters are given in Table 5.4.2. We obtained an inclination of 65°, a position angle of 16°, and a systemic velocity of 835 km s⁻¹. The systemic velocity is in good agreement with observations by Thuan et al. (2004) who measured v_{sys} to be 833 km s⁻¹ and a position angle of 17°, but their inclination of 82° is 26% higher than our value. They also derived a higher value of v_{rot} (54 km s⁻¹ in comparison to 46 km s⁻¹ measured by us), which cannot be explained by the difference in the inclination. Nevertheless, our result shows in agreement with Thuan et al. (2004) that the rotation velocity measured by Wilcots et al. (1996) of 80 km s⁻¹ (i of 67°) must be too high.

In order to prove the reliability of the derived parameters, a model velocity field with the best-fitting values was created (Fig. 5.6, lower left panel) and subtracted from the original velocity map (upper right panel). The residual map can be seen on the lower right panel of Fig. 5.6. The overall velocity field is very well represented by our derived parameters except for the extension in the east of the galaxy. Here, the residuals reach values of 15 to 20 km s⁻¹ in comparison to a general value of ± 5 km s⁻¹. As already mentioned in Sect. 5.3, this extension in combination with the disturbed

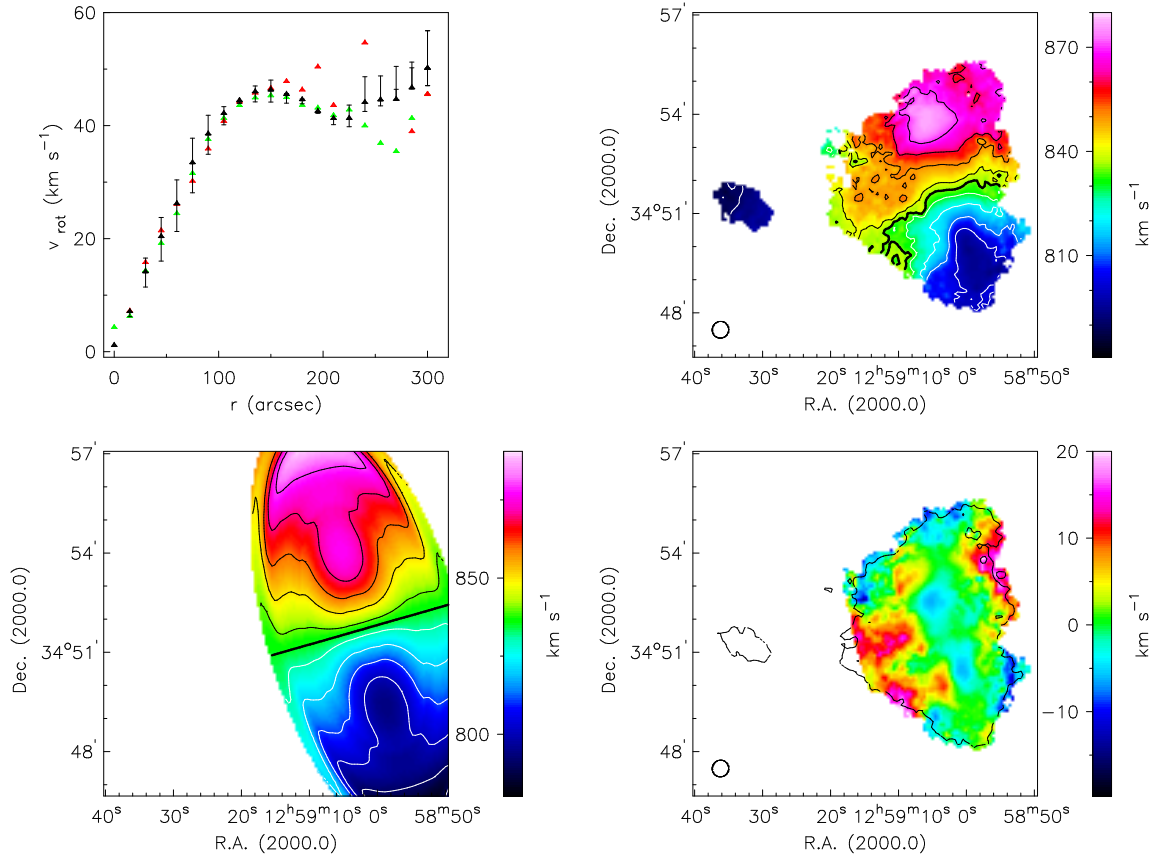


FIG. 5.6: The HI rotation curve of NGC 4861. **Top left:** Different approaches for deriving the rotation curve. The black symbols represent the best-fitting parameters, the error bars indicate receding and approaching side. The green curve was derived by taking the initial estimates and keep them fixed, the red curve by taking the best-fitting parameters and let them vary. **Top right:** The HI velocity field. **Bottom left:** The model velocity field, created by the best-fitting parameters. **Bottom right:** The residual map after subtracting the model from the original velocity map.

velocity field is caused by an interaction with a small HI cloud to the east of the main body. A discussion follows in Sect. 5.5.4.

5.5 Discussion

We found several outflows in $H\alpha$ and regularly rotating neutral gas. We now want to have a closer look at the HI spectra in order to look for deviations from the main components. The HI outflows are then compared to the expanding ionised gas structures and predictions about the fate of the outflows are made (also in comparison to NGC 2366). Furthermore, we will have a closer look at the small HI cloud.

5.5.1 Comparison of the neutral and ionised gas

The $H\alpha$ velocity field (see Fig. 5.5) shows two, possibly three major deviations from the overall rotation velocity, one in the south of the GEHR, one close to SGS1 and one north of the GEHR.

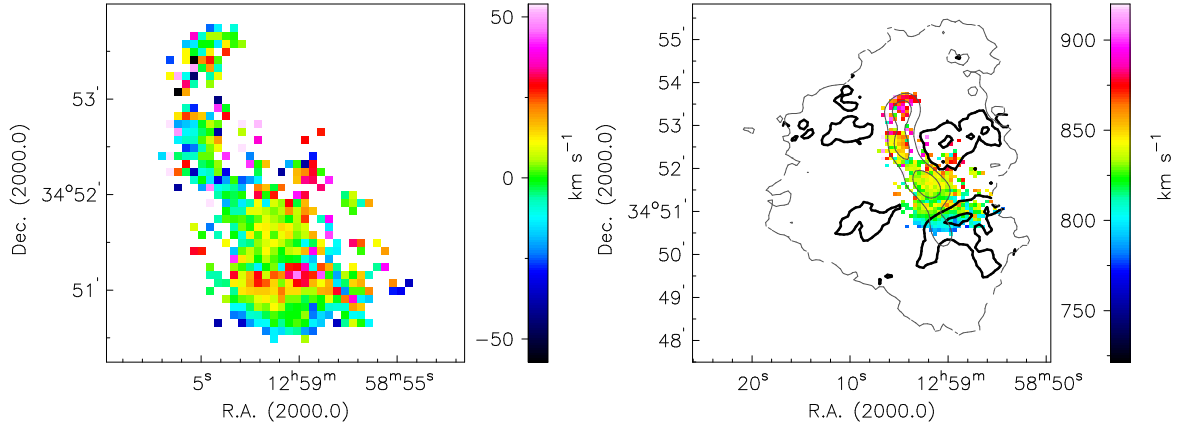


FIG. 5.7: A comparison of the neutral and ionised gas. The left panel shows the residuals after subtracting the H I velocity map from the H α velocity map. The right panel presents the H α velocity map with the H I dispersion contours at 18 and 22 km s⁻¹ overlaid in black. The outermost and two of the inner H I intensity contours are plotted in grey.

As a next step, the H I image was subtracted from the H α velocity map. Therefore, the FP data were smoothed to fit the spatial resolution of the H I data of $31'' \times 30''$. The residual map is shown in Fig. 5.7, left panel. At most positions, the velocities of the neutral and ionised gas are in good agreement. As already seen on the H α map, the two main outstanding parts are the south of the GEHR and the area close to SGS1. The gas in the southern part is blue-shifted with a velocity offset of about 20 km s⁻¹. The gas of the shell is red-shifted with a velocity offset of about 30 km s⁻¹. Additionally, some red-shifted gas can be seen north of the GEHR, also with expansion velocities of about 30 km s⁻¹. From the geometry and the similar expansion velocities both the blue-shifted outflow to the south of the GEHR and this red-shifted outflow could originate from the same event. The detections are a bit surprising as van Eymeren et al. (2007) found an expanding bubble around the GEHR with much higher velocities (see Sect. 5.1). They could detect the bubble in five highly-resolved spectra, which excludes any mistakes. On the other hand, we do detect this gas, but on the edges of the bubble where the line of sight velocities are smaller than in the middle. The central part of the GEHR could not be properly analysed due to the artificial emission that contaminates the velocity field (see Sect. 2.5). The spectra show very broad lines all over the GEHR, which might be an indication for an underlying second or even third component.

A hint of a blue- and a red-shifted component with high velocity offsets of 130 km s⁻¹ and 110 km s⁻¹, respectively – was also visible in the area of SGS5 (see Sect. 5.4.1). This area was not covered by the echelle spectra analysed in van Eymeren et al. (2007) so that we cannot prove at the moment whether it is true emission or an artefact. In case it is real emission, NGC 4861 becomes an interesting object because it then harbours two superbubbles with very high expansion velocities, which requires a very high energy input. XMM-Newton data show that NGC 4861 has a very luminous X-ray source in the centre of the GEHR (Stobbart et al. 2006), which would explain the high expansion velocities. In the area of SGS5, however, no X-ray emission can be seen.

On the the right panel of Fig. 5.7, the H I velocity dispersion contours at 18 and 22 km s⁻¹ are shown in black plotted over the H α velocity field. Additionally, the outermost and two of the inner contours of the H I intensity distribution at 0.01, 0.3, and 0.4 Jy beam⁻¹ are plotted in grey. The areas of high H I velocity dispersion coincide very well with the regions of expanding ionised gas. Therefore, we decided to have a closer look at the kinematics of the neutral gas. We performed a

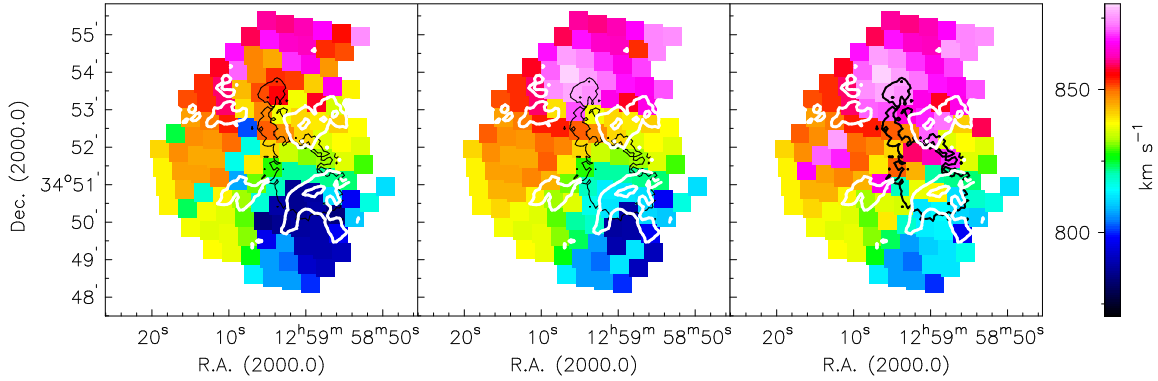


FIG. 5.8: Gaussian decomposition of the H I. Blue-shifted (left panel), main (middle panel) and red-shifted (right panel) components of the H I velocities are shown. Overlaid in white are the H I velocity dispersion in contours of 18 and 22 km s^{-1} as well as the outermost $\text{H}\alpha$ intensity contour in black.

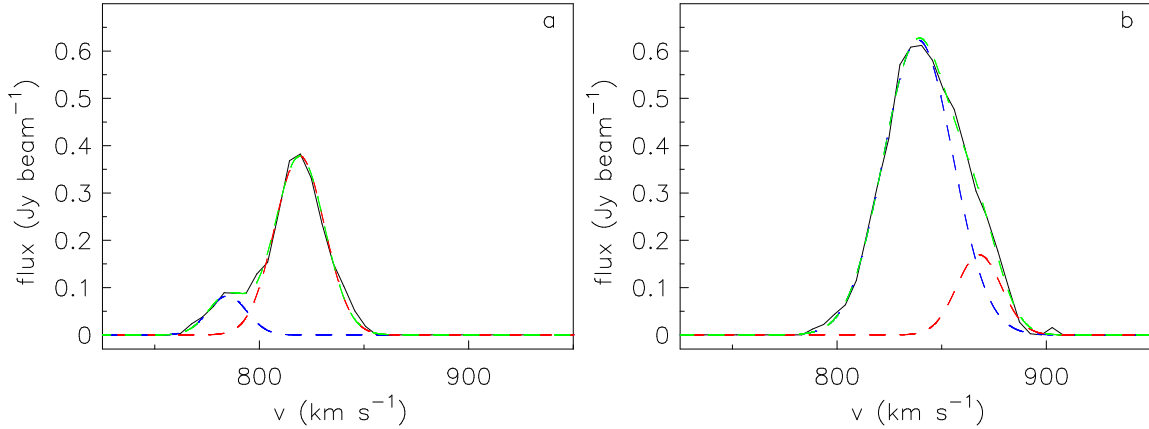


FIG. 5.9: Some example H I line profiles. (a) The blue-shifted outflow south of the GEHR. (b) The red-shifted outflow close to the supergiant shells. The Gaussian profiles fitted to the single components are plotted in blue and red, the resulting sum of the profiles is overlaid in green.

Gaussian decomposition of the H I velocities, especially at the positions of high velocity dispersion by averaging the velocities over one beam size. The result is shown in Fig. 5.8: the components of highest intensity are presented in the middle panel. Overlaid in white are the H I velocity dispersion contours at 18 and 22 km s^{-1} and the outer $\text{H}\alpha$ intensity contour in black. For a comparison, the blue- and red-shifted components are shown on the left and right panel. Note that regions where we did not find a blue- or redshifted component were filled with the main component. Two example spectra extracted from the H I cube are given in Fig. 5.9 together with the fitted Gaussian profiles for the single components (long-dashed blue and red lines) and the resulting sum (long-dashed green lines).

Looking at the southern part of the optical galaxy, a blue-shifted component is detected with a heliocentric line of sight velocity of about 786 km s^{-1} . The main component at this position has a velocity of about 812 km s^{-1} . The $\text{H}\alpha$ velocity field shows at the same position a blue-shifted outflow with velocities of about 780 to 790 km s^{-1} , which is in good agreement with the H I data. This outflow has already been detected in H I by Thuan et al. (2004) who suggested that this gas was moved away from the GEHR, driven by stellar winds and SNe over the last 1600 yr. The region west of NGC 4861 where the three supergiant shells are located reveals a red-shifted component (see Fig. 5.8, right

panel). The velocities vary between 860 and 870 km s⁻¹ in comparison to the main component of 830 to 840 km s⁻¹, which is comparable to the ionised gas as the H α velocity map shows a red-shifted component of 860 to 870 km s⁻¹.

Summarised, it can be said that the neutral and ionised gas show the same kinematic behaviour regarding outflows. In both cases, the neutral outflowing gas is much more extended than the ionised gas. This is certainly due to the much lower column densities of the ionised gas, which means that there is probably more extended gas, but the sensitivity of the FP data is not high enough to detect it.

As already mentioned above, the northern part of the GEHR shows a red-shifted component in H α with a velocity offset of about 30 km s⁻¹. Figure 5.8, right panel also shows some red-shifted emission at the same position with velocities of about 837 km s⁻¹, which corresponds to an offset of about 23 km s⁻¹ in comparison to the main H I component. The large velocity offset detected in the echelle spectra (van Eymeren et al. 2007), which we did not find in the H α velocity field, can therefore also not be detected in the H I velocity field. This does not necessarily mean that the expanding bubble does not exist. First of all, the H α velocity field is contaminated by artificial emission so that the existence of the outflow in H α cannot be ruled out. Furthermore, outflowing gas in H α without a counterpart in H I has already been found in NGC 2366 (see Chap. 4), which led to the interpretation that the H I in these cases is already fully ionised.

We showed in Sect. 5.3 that the H I intensity distribution (see Fig. 5.3, upper left panel) has at the positions of both outflows a different behaviour in comparison to the rest of the galaxy as the distance of two neighboured intensity contours becomes much larger. That means that the gas density is higher in these areas, which fits into the image of gas which is blown out and is at the same time moving more gas out of the GEHR and therefore enhancing the density.

Alltogether, it can be said that the expansion velocities are generally quite moderate, not only the ones of the gas close to the disk, but also of the structures further out like the SGSs. SGS5 shows no line-splitting in H I, only a component that follows the overall rotation so that the assumption of the blue-shifted component being a ghost feature (see Sect. 5.4.1) is further supported. However, as seen above, a missing H I outflow is no proof for a nonexistent H α outflow.

5.5.2 Outflow or galactic wind?

In order to learn about the fate of the outflowing gas, the expansion velocities of the detected outflows are now compared to the escape velocities of NGC 4861. The procedure is the same as described in Sect. 4.5.4. We took the pseudo-isothermal halo model and calculated the escape velocity following Eq. 4.2. The circular velocity was measured from the rotation curve to be 46 km s⁻¹ (see Table 5.4.2). We plotted the escape velocity for two different radii $r_{\text{max}} = 11$ kpc (dotted line) and $r_{\text{max}} = 22$ kpc (solid line). The lower value of r_{max} was chosen to equal the size of the H I distribution so that the corresponding curve is again a lower limit for the escape velocities. The result is shown in Fig. 5.10: the observed rotation curve including receding and approaching side is indicated by small grey triangular-shaped symbols. The expanding gas structures are marked by black large triangles. We corrected the values for an inclination of 65° as calculated in Sect. 5.4.2, which leads to an increase in velocity of about 10%.

As Fig. 5.10 shows, the expansion velocities of all outflows stay far below the escape velocities, which makes it impossible for the gas to leave the gravitational potential of the galaxy.

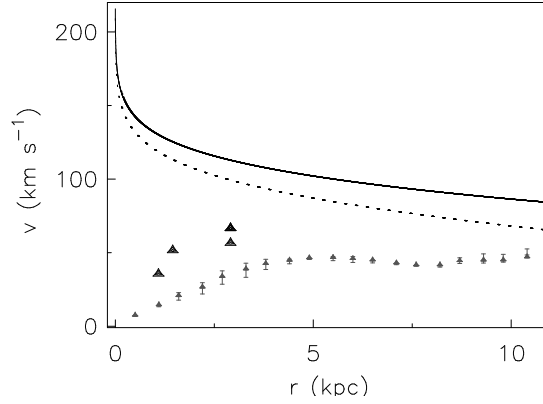


FIG. 5.10: Escape velocity for an pseudo-isothermal halo of $r_{\max} = 11$ kpc (dotted line) and $r_{\max} = 22$ kpc (solid line). The observed rotation curve is indicated by small grey triangles. The error bars represent receding and approaching side. The expanding gas structures are marked by black large triangles.

5.5.3 Comparison with NGC 2366

NGC 4861 is very well suited to be compared with NGC 2366 because not only its optical morphology is very similar to NGC 2366 (see Sect. 5.3), but also the parameters describing the kinematic properties of the neutral gas are similar for both galaxies. The HI distribution of NGC 2366, however, is more patchy and the velocity field is more perturbed, which results, e.g., also in higher outflow velocities in comparison to NGC 4861. The main drivers for the distortions are probably the GEHR and the possible spiral arms. NGC 4861 has no spiral arms, but also a GEHR. Two major outflows are directly connected to it, a third one is close to the supergiant shells. The expansion velocities do not exceed 30 km s^{-1} and all outflows were detected in the HI and the $\text{H}\alpha$ velocity field. The 50 km s^{-1} outflow in NGC 2366, however, was only detected in $\text{H}\alpha$. As already discussed in Sect. 4.5.1, this is probably an effect of age and energy input. The energy input of the GEHR in NGC 4861 seems not to be high enough to have fully ionised the surrounding neutral medium, which might indicate that this galaxy is younger than NGC 2366 or less affected by events that trigger star formation (like, e.g., density waves). The outflow close to the supergiant shells is most probably ionised by a different cluster.

5.5.4 HI cloud to the east

We saw on the HI moment maps that NGC 4861 has a small companion east of the main body at a deprojected distance of 4 kpc. It seems to interact with the main HI complex as the large-scale HI distribution is extended in the direction of the HI cloud and the velocity field is distorted. Publications by, e.g., Wilcots et al. (1996) imply that the cloud has no optical counterpart. However, they only used a DSS image so that we decided to perform deep imaging.

Figure 5.11 shows an overlay of the outer HI intensity contour at $0.01 \text{ Jy beam}^{-1}$ over our *R*-band and *V*-band images. Despite an exposure time of 900 s with a 3.5m telescope in the case of the *R*-band image, no optical counterpart of NGC 4861 B can be seen. We therefore obtained a 90 min *V*-band exposure with the Calar Alto 2.2m telescope, which does also not show any stellar association that could be connected to the HI cloud. Assuming that the size of a possible stellar disk equals the HI extent of $98'' \times 53''$, we derived an upper limit for the integrated flux in the *V*-band of $m_V < 24.3 \text{ mag}$ and $M_V < -6.54 \text{ mag}$, respectively, which makes the existence of a stellar component very unlikely.

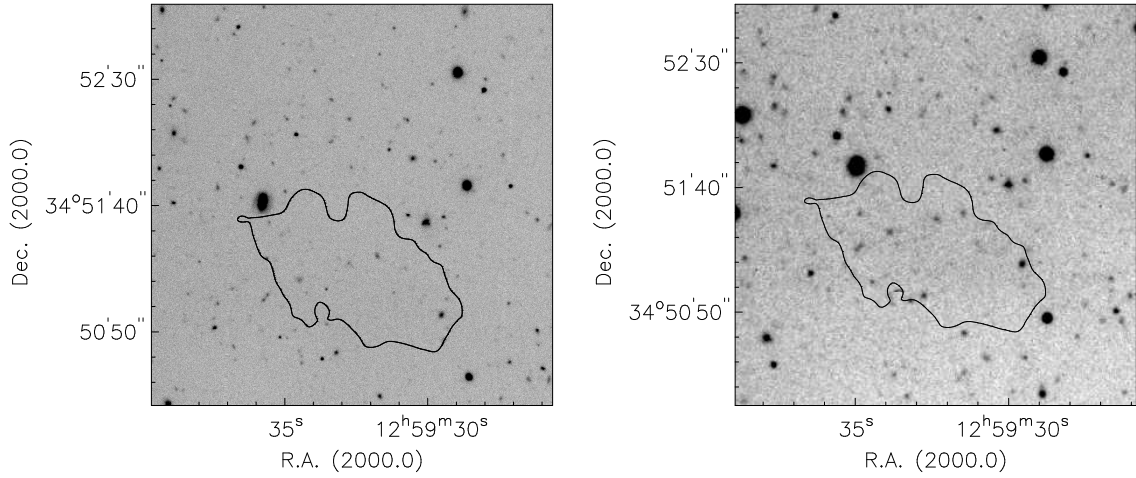


FIG. 5.11: Deep R -band and V -band images of the surroundings of NGC 4861. Overlaid in black is the outer H I intensity contour of the H I cloud at $0.01 \text{ Jy beam}^{-1}$.

Additionally, we had again a look at the H I velocity field and performed the same kinematic analysis for the H I cloud as for the whole galaxy (see Sect. 5.4.2) treating the cloud as an individual system. As we are limited by both spectral and spatial resolution and as the emission is detected at 5σ , which is close to our detection limit, we worked with the initial estimates derived by *ellfit* as the best-fitting parameters. Therefore, the results are just an estimate. The left panel of Figure 5.12 shows the velocity field, the model and the residual map are displayed in Fig. 5.12 middle and right panel. The velocity field reveals a fairly regular rotation pattern with a rotation velocity of 4.4 km s^{-1} . The inclination is the same as the one of NGC 4861, but the cloud rotates under a different position angle than the main body (see Table 5.4.2). The systemic velocity was measured to be 791 km s^{-1} , which is about 60 km s^{-1} lower than expected from the rotation of the main body. Having in mind that the line of sight velocity difference between single galaxies in a group can be of the order of 100 km s^{-1} at a distance of these galaxies of several hundred kpcs, this velocity offset might indicate that NGC 4861 B lies in the foreground of NGC 4861 at a distance of maybe 100 kpc or more.

These results make NGC 4861 B an interesting candidate for the dark galaxy debate. The detection of dark galaxies is important for the cosmologists as it would offer a solution to the missing satellite problem (see Sect. 1.1). Studies by, e.g., Taylor et al. (1993) and Taylor et al. (1995) exclusively concentrated on the search for isolated H I clouds in the vicinity of dwarf galaxies. They found the fraction to be very high, although more than 50% of them had an optical counterpart. One of the most famous dark galaxy candidates at the moment is VIRGOHI21, which has a velocity width of 220 km s^{-1} , no optical counterpart down to a surface brightness level of $27.5 \text{ B mag arcsec}^{-2}$, and is located at a distance of 150 kpc from the next galaxy (NGC 4254) (Minchin et al. 2005). It was interpreted by the authors as a dark matter halo. However, it is very difficult to differentiate a dark galaxy from tidal debris. Simulations, e.g., by Bekki et al. (2005) show that tidal debris can have the same properties concerning velocity width, optical surface brightness and distance from the progenitor, even if the values are as high as for VIRGOHI21.

NGC 4861 B has a very low velocity width, but in comparison to this low width a high H I mass. Therefore, we checked whether the parameters are consistent with the Baryonic Tully-Fisher (BTF) relation (see Fig. 5.13). The grey stars represent the galaxies analysed by McGaugh (2005) with his

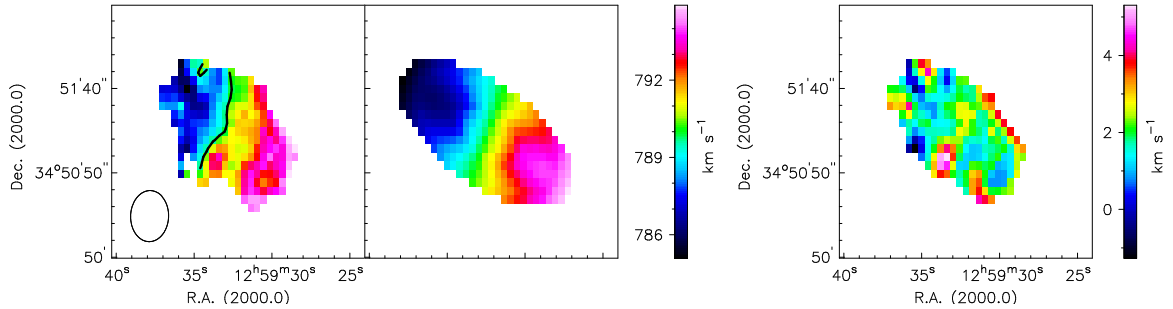


FIG. 5.12: A kinematic study of the H I cloud NGC 4861 B. Velocity map (left panel) with a black contour at $v_{\text{sys}} = 791 \text{ km s}^{-1}$, model velocity field (middle panel) and residual map (right panel).

fit of $M = 50 * v^4$ as long-dashed line, black dots are from Trachternach et al. (2008b). NGC 4861 B (black filled triangle) lies far above the correlation. Assuming that it has a stellar component would even increase the distance from the correlation. Observations by Begum et al. (2006) show that galaxies with H I masses of $4 \times 10^6 M_{\odot}$ or even less exist (e.g., KK 230 or DDO 210). However, these two galaxies have rotation velocities that are a factor of two and four, respectively higher than the one of NGC 4861 B and therefore better fulfil the BTF correlation (see black squares in Fig. 5.13). Note that we neglected the stellar mass. The ellipse fitting task calculated an inclination angle of 65° for the H I cloud, which is quite high. If we assume a much lower inclination (about 14°), the rotation velocity would rise and the cloud would approach the BTF correlation. This implies, of course, that the BTF correlation also works for these low masses and low rotation velocities because the galaxies mentioned above lie all at the lower end.

Alltogether, it can be said that at the moment we cannot rule out any idea of what NGC 4861 B might be, dark galaxy or just tidal debris or infalling gas. Our deep V-band image implies that the existence of a stellar component is very unlikely and the H I velocity field shows a regular rotation. These are both strong arguments to interpret the cloud as a dark galaxy. However, we need a better measurement of the inclination and a higher spatial resolution and sensitivity of the H I data in order to verify our interpretation.

5.6 Summary

Fabry-Perot interferometry and H I synthesis observations were performed to compare the morphology and the kinematics of the neutral and ionised gas component in the irregular dwarf galaxy NGC 4861.

Both gas components show a very similar behaviour. The overall velocity gradient runs from the south-west to the north-east from 800 to 870 km s^{-1} . We detected a blue-shifted outflow in the south of the GEHR with an expansion velocity of about 23 km s^{-1} as well as a red-shifted outflow in the north of the GEHR with an expansion velocity of about 25 km s^{-1} . Furthermore, a red-shifted outflow was detected close to the SGSs in the west of the tail with an expansion velocity of about 30 km s^{-1} . All outflows are more extended in H I than in H α . A comparison of the expansion velocities with the escape velocity of the galaxy using the pseudo-isothermal halo model reveals that the gas stays gravitationally bound. However, we did not include the two fast expanding superbubbles mentioned in Sect. 5.5.1. The one expanding from the GEHR is too close to the dynamical centre where the escape velocities are high. SGS5, whose existence first needs to be confirmed by, e.g., obtaining a slit spectrum, is a bit further away from the dynamical centre, which means that here, the probability of a galactic wind is strongly increased.

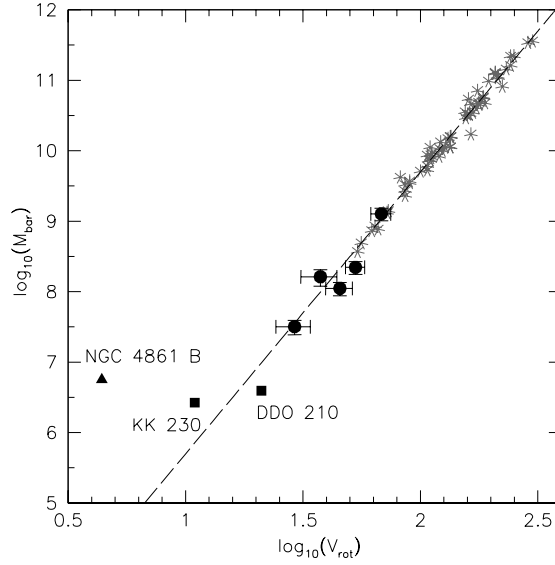


FIG. 5.13: Baryonic Tully-Fisher relation. The grey stars represents the values measured by McGaugh (2005) with their fit of $M = 50 * V^4$ as long-dashed line. The black dots are from Trachternach et al. (2008b), the black squares from Begum et al. (2006). NGC 4861 B is marked by a filled triangle.

Additionally, we examined the H I cloud NGC 4861 B in more detail. A 90 min V-band exposure obtained with the Calar Alto 2.2m telescope suggests that this cloud has no optical counterpart as we did not detect any star association down to a 3σ detection limit of 27.84 in V. Nevertheless, it shows a regular rotation, although that small in comparison to an H I mass of $4 \times 10^6 M_{\odot}$ that it lies far above the Baryonic Tully-Fisher relation. From our results, an interpretation as a dark galaxy cannot be ruled out.

5.A Appendix: H α image and extension of the catalogue of ionised gas structures

Here, the continuum-subtracted H α image is again presented in an enlarged version and with a different contrast as in Fig. 5.1 to emphasise the small-scale structure (see Fig. 5.14). Additionally, the catalogue of van Eymeren et al. (2007) is extended by the supergiant shell at the northern tip of the galaxy.

TABLE 5.3: The most prominent structures and their sizes in NGC 4861 – an extension –.

Source	Diameter ["]	Diameter [pc]	v_{helio} [km s $^{-1}$]	FWHM [km s $^{-1}$]
SGS5	28	1018		

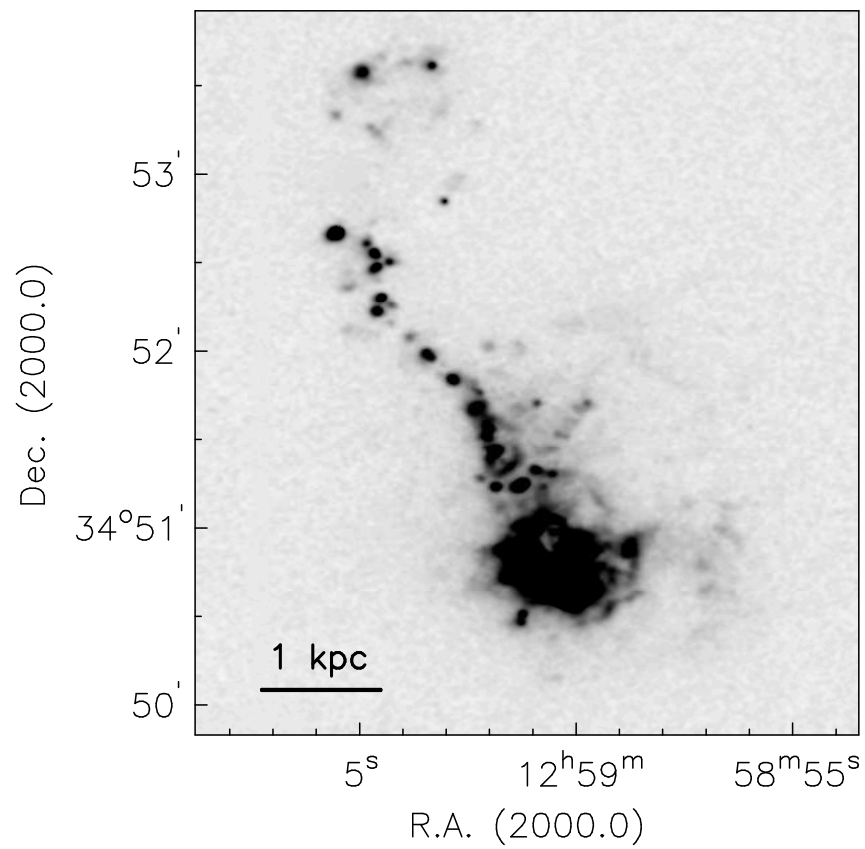


FIG. 5.14: Continuum-subtracted H α image of NGC 4861. The contrast is chosen in a way to demonstrate the small-scale structures.

The Local Volume HI Survey: Gas kinematics in IC 4662 and NGC 5408

Abstract

The feedback between massive stars and the interstellar medium is one of the most important processes in the evolution of dwarf galaxies. Numerous neutral and ionised gas structures both in the disk and in the halo have been found, but their origin and fate are not clear, yet. Therefore, we want to study the kinematics of both gas components in order to search for outflowing gas structures and to make predictions about their fate.

We here present new radio and optical data of two peculiar dwarf galaxies in the Local Volume: IC 4662 and NGC 5408. The HI line and 20 cm radio continuum data were obtained with the Australia Telescope Compact Array and are part of the “Local Volume HI Survey”. The radio data are complemented by optical images and spectroscopic data obtained with the ESO New Technology Telescope.

The HI velocity field of NGC 5408 is fairly regular, whereas IC 4662 shows disturbed HI kinematics. After a Gaussian decomposition of the HI and the H α line, we found several outflows in both galaxies with expansion velocities up to 75 km s^{-1} , sometimes present in both gas components, sometimes only in one gas component. However, the expansion velocities are too low to allow the gas to escape from the gravitational potential of the galaxies as a comparison with the escape velocities derived from the cored pseudo-isothermal halo model shows. This result is consistent with studies of other dwarf galaxies.

6.1 Introduction

The interplay between massive stars and the interstellar medium (ISM) has a large effect on the formation and the evolution of galaxies. Thereby, dwarf galaxies provide a perfect environment for this kind of interaction as they are simple systems, fragile and hence likely to be strongly affected by both external and internal processes (e.g., Gallagher & Hunter 1984).

Numerous ionised gas structures in and around the galactic plane of these galaxies have been found (e.g., Bomans et al. 1997; Hunter & Gallagher 1997; Martin 1998; van Eymeren et al. 2007).

Generally, these structures enclose large concentrations of massive stars. In this case, the ionisation mechanisms are relatively well understood: kinetic energy and momentum are delivered by massive stars to their surroundings through stellar winds and supernovae explosions. A superbubble filled with hot gas evolves and begins to expand into the ISM. Due to Rayleigh-Taylor instabilities the outer shells can rupture and the hot gas can rise through tunnel-like features – chimneys – into the halo (Norman & Ikeuchi 1989). However, it is not clear, yet what the final fate of the gas is. Theoretical models predict that at least part of the hot gas has enough kinetic energy to leave the gravitational potential of its host galaxy and to enrich the intergalactic medium (IGM) by becoming a freely flowing wind (e.g., Mac Low & Ferrara 1999). The relatively low escape velocities of dwarf galaxies facilitate the removal of substantial amounts of gas. Nevertheless, no convincing case of a galactic wind has been reported so far (Bomans 2005).

We here present a multi-wavelengths study of two more galaxies, the peculiar dwarf galaxies IC 4662 and NGC 5408. We performed HI and 20 cm radio continuum observations as well as optical imaging and spectroscopy.

IC 4662 (HIPASS J1747–64) is classified as an IBM galaxy. Its distance of $D_{\text{TRGB}} = 2.44$ Mpc was obtained by Karachentsev et al. (2006) and makes it therefore to be the nearest known representative of blue compact dwarfs (Karachentsev et al. 2006). It seems to be a rather isolated galaxy, belonging to no known groups. de Vaucouleurs (1975) describes IC 4662 as a foreground galaxy in the direction of the NGC 6300 group.

NGC 5408 (HIPASS J1403–41) is classified as an IB(s)M galaxy. It was first studied by Bohuski et al. (1972). Its nucleus consists of several bright H II regions and appears to be undergoing a violent burst of star formation (Bohuski et al. 1972). As it harbours an ultra-luminous X-ray source very close to the concentrations of H II regions, it was a popular object to study over the last decades. Its distance of $D_{\text{TRGB}} = 4.81$ Mpc was obtained by Karachentsev et al. (2002). Its position on the sky puts NGC 5408 in the Centaurus A group, but its distance differs from the medium value of Cen A members by more than 1 Mpc.

This chapter is organised as follows: in Section 6.2 we summarise the observations and the data reduction. In § 6.3 we compare the morphology of the neutral and ionised gas and the radio continuum. Section 6.4 contains a kinematic analysis including a search for outflowing gas. The fate of the gas is discussed in § 6.5, which will be followed by a summary in Sect. 6.6.

6.2 Observations and Data Reduction

6.2.1 ATCA radio data

HI line and 20 cm radio continuum observations of IC 4662 and NGC 5408 were obtained with the Australia Telescope Compact Array (ATCA) as part of the “Local Volume HI Survey” (LVHIS). IC 4662 was observed for a full synthesis (12 h) in each of three arrays (see Table 6.2). The lower resolution data of NGC 5408 (375 and 750D array) were taken from the archive and complemented by high-resolution data within LVHIS (1.5A array). As the archival data were part of a larger sample of galaxies, all observed within a few nights, the uv -coverage is worse than for IC 4662. Therefore, the synthesised beam of IC 4662 is generally better than the one of NGC 5408.

The first frequency band was centred on 1418 MHz with a bandwidth of 8 MHz, divided into 512 channels. This gives a channel width of 3.3 km s^{-1} and a velocity resolution of 4 km s^{-1} . The ATCA primary beam is $33'.6$ at 1418 MHz. The second frequency band was centred on 1384 MHz (20 cm) with a bandwidth of 128 MHz.

TABLE 6.1: The basic properties of IC 4662 and NGC 5408.

Optical name	IC 4662	NGC 5408	References
HIPASS name	J1747-64	J1403-41	
optical centre:			
α (J2000)	17 ^h 47 ^m 08.8 ^s	14 ^h 04 ^m 22 ^s	(1)
δ (J2000)	-64° 38' 30''	-41° 22' 36''	(1)
l, b	328.6, -17.9	317.2, 19.5	(1)
distance [Mpc]	2.44	4.81	(2)
v_{opt} [km s ⁻¹]	336 ± 29	537 ± 33	(1)
type	IBm	IB(s)m	(1)
optical diameter	3.0' × 1.6'	2.6' × 1.6'	(3)
"	2.1 kpc × 1.1 kpc	3.6 kpc × 2.2 kpc	
inclination	58°	52°	(3)
position angle	104°	62°	(3)
m_B [mag]	-14.84 ± 0.09	-15.84 ± 0.09	(3)
v_{HI} [km s ⁻¹]	302 ± 3	506 ± 3	(4)
v_{LG} [km s ⁻¹]	153	314	(4)
w_{50} [km s ⁻¹]	86	62	(4)
w_{20} [km s ⁻¹]	133	112	(4)
F_{HI} [Jy km s ⁻¹]	130.0 ± 12.0	61.5 ± 6.7	(4)
log M_{HI} [M_{\odot}]	8.26 ± 0.04	8.53 ± 0.03	

The total B -magnitude, m_B , was obtained from Lauberts & Valentijn (1989). Using the Galactic B -band extinction, A_B (Schlegel et al. 1998), these were converted to absolute magnitudes, M_B .

References: (1) de Vaucouleurs et al. (1991), (2) Karachentsev et al. (2004), (3) Lauberts & Valentijn (1989) [ESO Uppsala], (4) Koribalski et al. (2004) [HIPASS BGC].

TABLE 6.2: ATCA radio observations.

Object	IC 4662	NGC 5408
	EW367	375
Arrays	750A	750D
	1.5D	1.5A
HI synthesised beam (na)	70'' × 62''	57'' × 50''
20 cm synthesised beam (r0)	33'' × 29''	77'' × 53''

TABLE 6.3: Imaging – Some observational parameters.

Parameter [Unit]	IC 4662	NGC 5408
Filter	608 (R) / 596 (H α)	642 (R) / 692 (H α)
Exp. Time [s]	600 / 1800	600 / 1200
Spatial resolution ["]	0.36	0.16

The data reduction was performed with the MIRIAD software package using standard procedures. Both H I and 20 cm data were flux- and phase-calibrated. Using a first order fit to the line-free channels in the H I data set, the 20 cm radio continuum is separated from the pure H I emission. The H I channel maps were made using “natural” (na) weighting of the uv -data in the velocity range covered by the H I emission in steps of 4 km s^{-1} and a standard Hanning smoothing was applied. They are displayed in Figs. 6.1 and 6.2, superimposed on a greyscale presentation of our R -band images. The white cross in the first channel marks the optical centre of the galaxy. The beam is placed into the lower left corner of the same channel. The corresponding heliocentric velocities are indicated in the upper right corner of each channel. In case of IC 4662, we excluded the longest baselines, which are all baselines to the distant antenna 6, because they do not contain any significant flux. In case of NGC 5408, the longest baselines are included, which gives us a resolution comparable to IC 4662 despite the worse uv -coverage. One $\text{Jy beam}^{-1} \text{ km s}^{-1}$ corresponds to an H I column density of $2.59 \times 10^{20} \text{ atoms cm}^{-2}$ (IC 4662, na) and $3.9 \times 10^{20} \text{ atoms cm}^{-2}$ (NGC 5408, na), respectively.

The broadband 20 cm continuum maps of both galaxies were made using robust ($r=0$) weighting, but excluding all baselines to CA06. The resulting synthesised beams for all data sets are given in Table 6.2. The measured rms noise is around $0.1 \text{ mJy beam}^{-1}$.

In order to create the moment maps and to analyse the H I data, the software GIPSY¹ was used. The moment maps were created by first isolating the regions of significant emission in every channel and afterwards clipping everything below a 3σ threshold (for further details see App. C).

6.2.2 Optical data

The optical data presented here (both imaging and spectroscopy) were obtained with the EMMI instrument attached to the 3.5m ESO New Technology Telescope (NTT). A standard data reduction was performed using IRAF.

Imaging

Deep R -band and H α data are available for both galaxies. The images of IC 4662 were observed by us, the images of NGC 5408 are from the ESO archive. After the standard data reduction, further reduction steps were carried out. In order to get the pure H α line emission, the flux of the stars in the continuum image was scaled to the H α flux and the continuum image was afterwards subtracted from the H α image. In order to stress weaker structures in the H α images and to differentiate them from the noise, adaptive filters based on the H-transform algorithm (Richter et al. 1991, see App. B) were used. The resulting R -band images are displayed in Fig. 6.3 and the relevant observational parameters are given in Table 6.3.

¹The Groningen Image Processing System

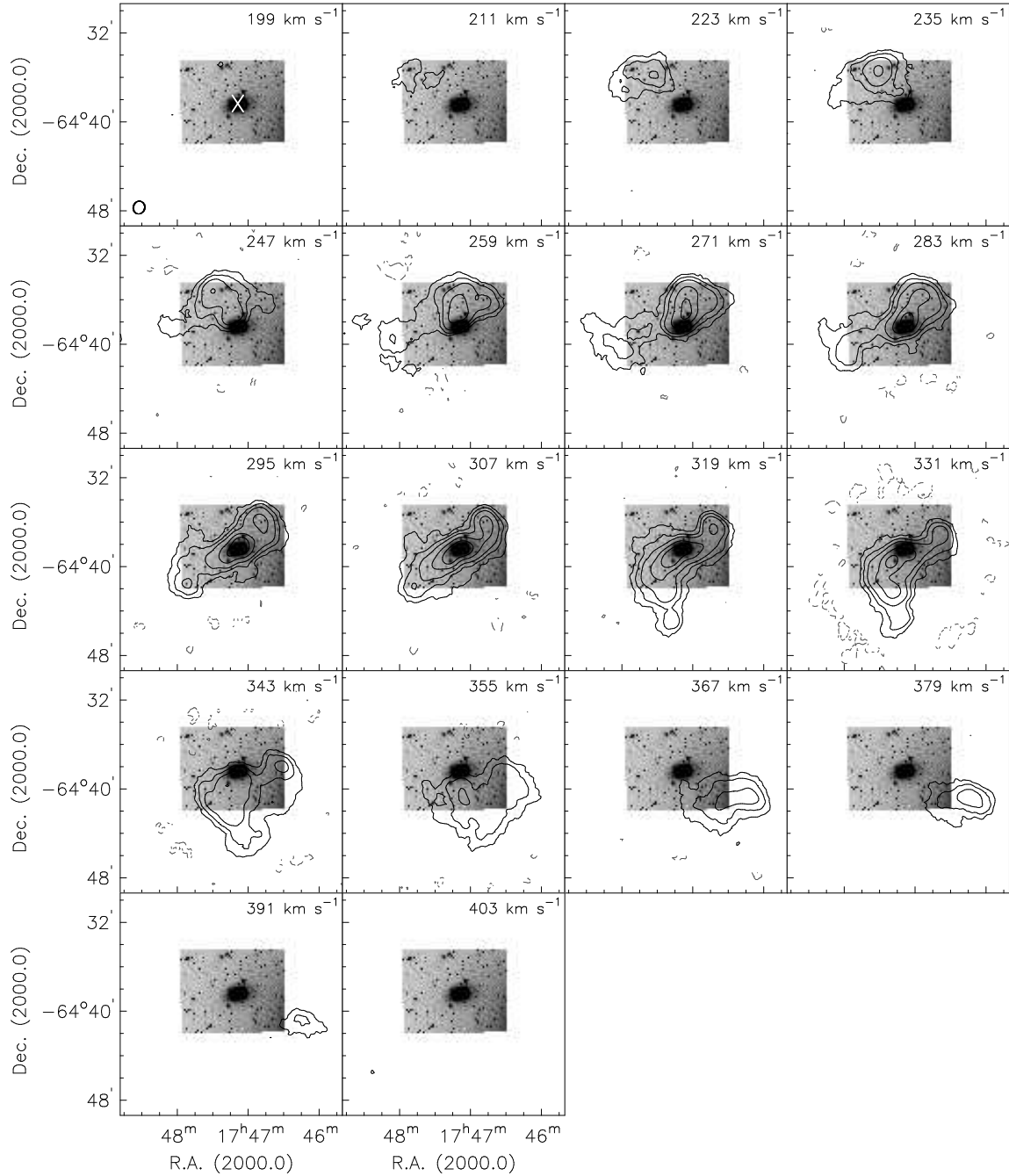


FIG. 6.1: HI channel maps of IC 4662 (contours) superposed on our *R*-band image. Contours are drawn at -4.5 (-3σ), 4.5 (3σ), 10, 20, 50, 100, and $200 \text{ mJy beam}^{-1}$. The synthesised beam (natural weighting) is displayed in the lower left corner of the first channel map. The optical centre of the galaxy is marked by a white cross in the same channel map. The corresponding heliocentric velocities are indicated in the upper right corner of each channel. A standard Hanning smoothing was applied to the cube. The original channel spacing is 4 km s^{-1} .

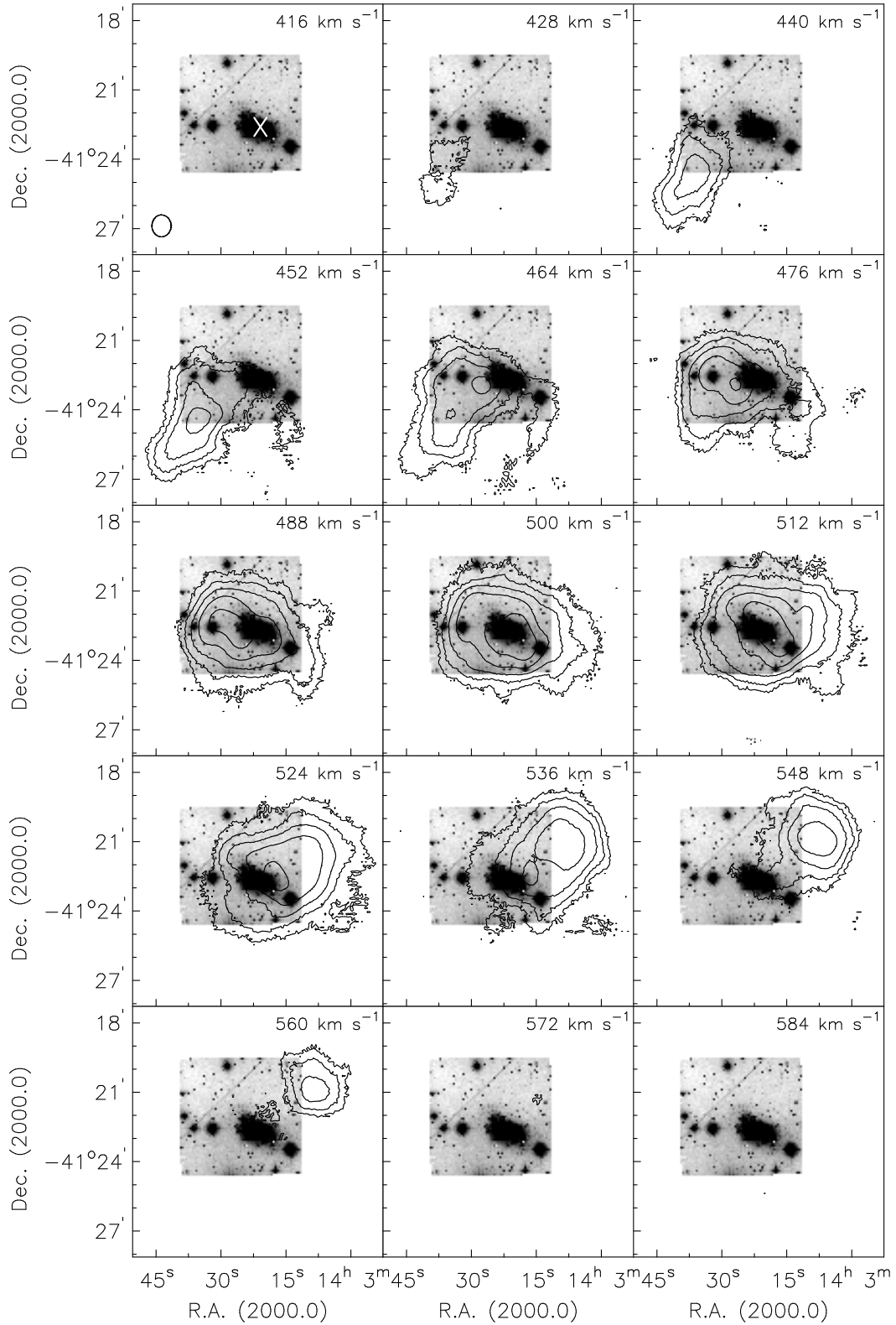


FIG. 6.2: HI channel maps of NGC 5408 (contours) superposed on the *R*-band image. The same as in Fig. 6.1. Contours are drawn at -4 (-3σ), 4 (3σ), 8 , 16 , 32 , and 64 mJy beam^{-1} .

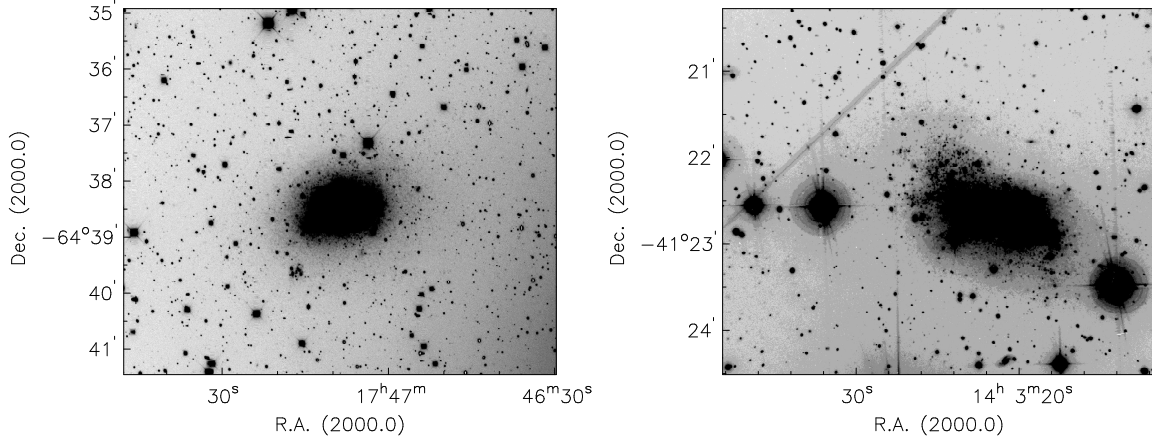


FIG. 6.3: *R*-band images of the peculiar dwarf galaxies IC 4622 (left panel) and NGC 5408 (right panel), obtained with EMMI attached to the ESO NTT.

Medium-resolution long-slit spectroscopy

Archival medium-resolution long-slit spectra with a spectral resolution of about 60 km s^{-1} , as measured from the night sky lines, were reduced and used for a kinematic analysis of NGC 5408. As the target of these observations was the X-ray source in NGC 5408, all spectra were obtained at almost the same position. Therefore, we only took one slit position as a representative.

Further medium-resolution spectra not only of NGC 5408, but also of IC 4662 were obtained from May 1st to May 3rd 2006 by us. Only the red part of EMMI was read out using grating #7 centred at the $\text{H}\alpha$ line with a wavelength coverage of 1300 \AA and a dispersion of 0.41 \AA/pix . With a slit width of $1''$, we achieved a spectral resolution of 112 km s^{-1} , again as measured from the night sky lines. The spatial resolution is $0''.332$ and the seeing was about $1''$. A geometric distortion correction was not necessary because the deviations were smaller than one pixel. For the wavelength calibration, spectra of a thorium comparison lamp were obtained. The detector is a mosaic of two chips with the overscan region lying in between. As the emission is very extended, both chips had to be used to obtain a spectrum, which meant that a small part of the emission always lay in the gap. A single spectrum was exposed for 45 min. Afterwards, the telescope was slightly moved to have a different part of the emission in the gap.

Three spectra each at different positions along the two galaxies were obtained. Details are given in Table 6.4. For the measurement of the emission lines, the spectra were binned in spatial direction by three pixels, which corresponds to about $1''$ matching the seeing. At positions of very weak emission, ten pixels were summed up to improve the signal to noise (S/N) ratio. The IRAF task *splot* was used in the interactive mode to determine the peak wavelength and the Full Width at Half Maximum (FWHM). All wavelengths measurements were converted into heliocentric velocities.

6.3 General morphology

At the beginning of the analysis, we had a look at the optical and radio morphology of IC 4662 and NGC 5408 in order to have a first impression of how the stars and the gas are connected. Additionally, we measured the star formation rates from the 20 cm radio continuum data.

TABLE 6.4: Long-slit spectroscopy – some details.

Object	Slit No.	Exp. Time [min]	PA [$^{\circ}$]
NGC 5408	1	225	54
	2	180	6
	3	201.5	296
	1b	60	80
IC 4662	1	180	330
	2	135	56
	3	180	70

6.3.1 IC 4661

Our optical images show that IC 4662 has a slightly elongated shape along the east-west axis (see Fig. 6.3, left panel and Fig. 6.16 of App. 6.A, upper panel). On the $H\alpha$ image, this part of the galaxy is surrounded by diffuse filamentary structure, especially in the eastern part. Additionally, a cluster of stars with associated $H\alpha$ emission that appears to be detached from the main body of the galaxy can be seen. It is located $1\frac{1}{5}$ or 1.1 kpc to the south-east of the centre. Hidalgo-Gómez et al. (2001) pointed out that this H II region differs significantly from the main body in oxygen abundance. Therefore, the scientists speculate whether it is an own system interacting with IC 4662 (e.g., H. Lee, private communication) or just an unusually placed OB association. Our deep $H\alpha$ image in combination with the H-transform algorithm shows that this bright H II region is at least connected to the main complex by a chain of small H II regions and diffuse filamentary gas structures. We will come back to this peculiarity during the kinematic analysis.

The upper left panel of Fig. 6.4 shows the H I intensity distribution, which seems to consist of two parts. The inner high-intensity system is perpendicular to the outer low-intensity system. As displayed in Fig. 6.5, the inner system coincides with the optical extent of IC 4662 including the southern H II region. We see an additional H I maximum to the north-west with no optical counterpart.

In Fig. 6.6 (left panel) the 20 cm radio continuum contours are plotted over the continuum-subtracted $H\alpha$ image, which coincide very well with the optical extent of the galaxy. Not only the bright H II regions in the north, but also the small H II region in the south-east can be seen at 20 cm.

6.3.2 NGC 5408

Like IC 4662, the stellar disk of NGC 5408 is slightly elongated along the east-west axis, which leads to a box-like appearance in the optical (see Fig. 6.3, right panel and Fig. 6.16 of App. 6.A, lower panel). It is dominated by a bright complex of H II regions in the south-west. In the eastern part, the ionised gas becomes more patchy with several filaments emanating from the disk. Diffuse gas can also be seen on the whole southern side of the galaxy.

The H I intensity distribution looks fairly symmetric with two point-like maxima in the centre (see Fig. 6.7, upper left panel). A comparison with the ionised gas distribution shows that the H I intensity maximum coincides with the optical extent of NGC 5408 (see Fig. 6.5).

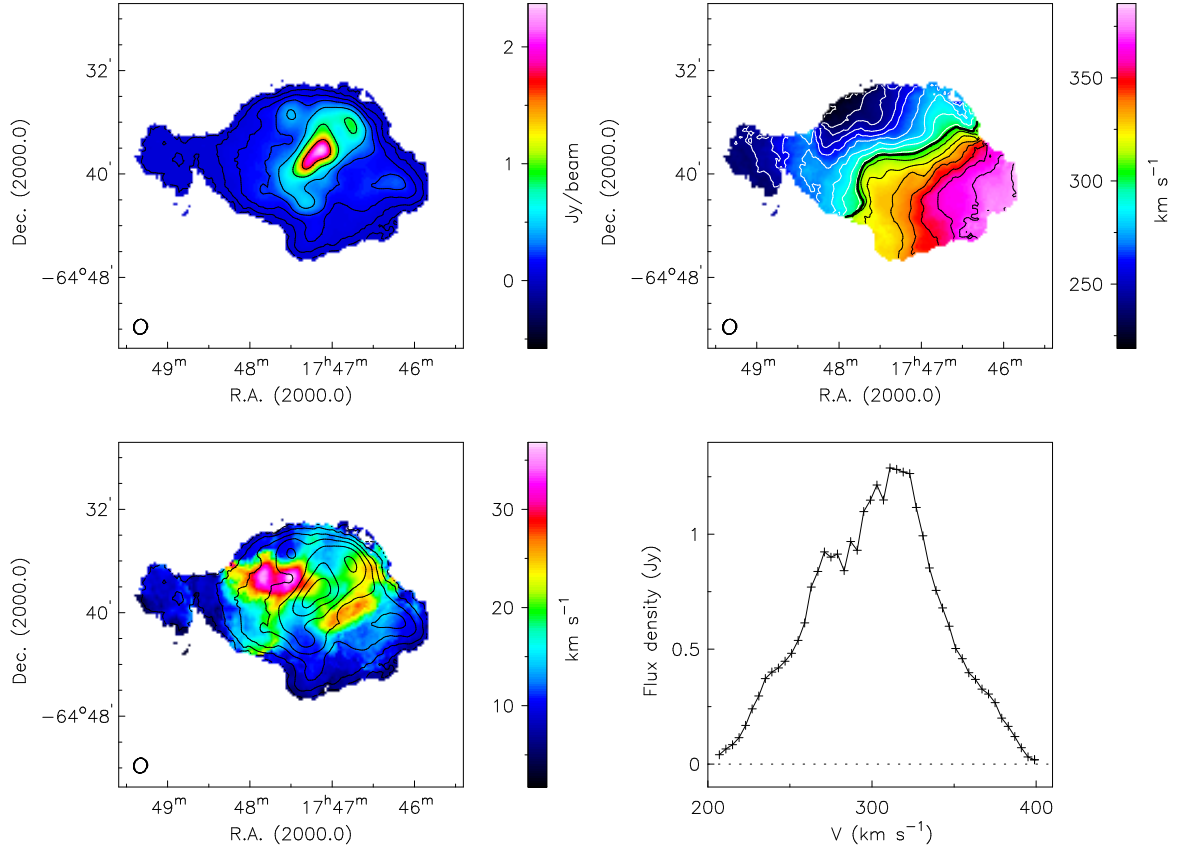


FIG. 6.4: HI moment maps of IC 4662, combining three arrays, but excluding baselines to CA06, which leads to a synthesised beam of $70'' \times 62''$. **Top left:** The H I distribution (0th moment map). Contours are drawn at 0.015 (3σ), 0.04, 0.1, 0.2, 0.4, 0.8, and 1.6 Jy beam^{-1} where $0.015 \text{ Jy beam}^{-1}$ correspond to a column density of $3.3 \times 10^{20} \text{ atoms cm}^{-2}$. **Top right:** The mean H I velocity field (contour levels range from 220 to 380 km s^{-1} in steps of 10 km s^{-1}). The systemic velocity of 302 km s^{-1} derived by Koribalski et al. (2004) is marked in bold. **Bottom left:** The H I velocity dispersion. Overlaid are the same H I intensity contours as on the 0th moment map. **Bottom right:** The global intensity profile. The short-dashed line marks zero intensity.

The right panel of Fig. 6.6 displays the 20 cm radio continuum contours superimposed onto the $\text{H}\alpha$ image. The continuum peaks at the position of the bright H II region in the south-western part of the galaxy, which is also the position of the western H I maximum. It is more or less a point source with a slight extension to the north-east, following the main part of the body and further out. Unfortunately, we are limited by the beam size. Higher resolution data are needed to prove whether the radio continuum is more than a point source.

6.3.3 Star Formation rates

In order to estimate the star formation rate (SFR) of a galaxy from the 20 cm data, we used

$$SFR [\text{M}_{\odot} \text{ yr}^{-1}] = 0.14 D^2 S_{20 \text{ cm}} \quad (6.1)$$

derived from Condon (1992) and Haarsma et al. (2000), where D is the distance in Mpc. We measured a flux density of $S_{20 \text{ cm}} = 33 \text{ mJy}$ in IC 4662 and $S_{20 \text{ cm}} = 24 \text{ mJy}$ in NGC 5408, resulting in $SFR =$

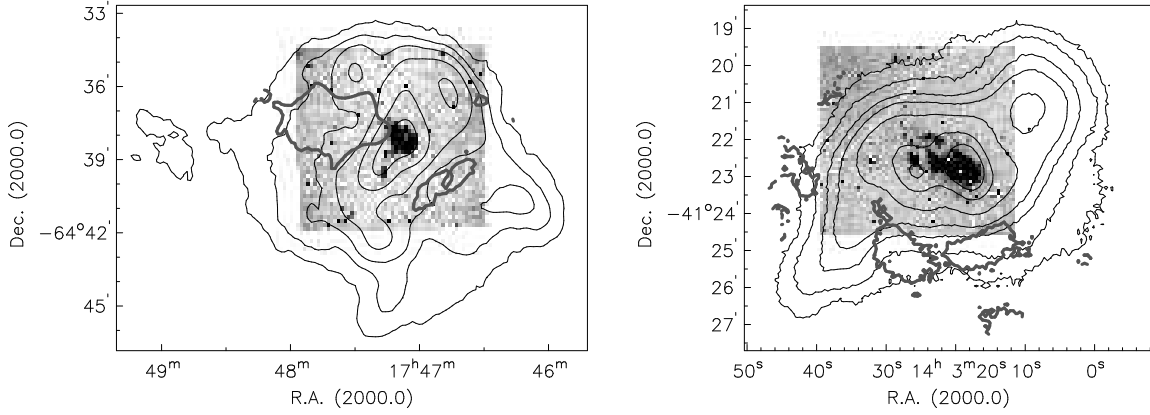


FIG. 6.5: Continuum-subtracted H α images of IC 4662 (left panel) and NGC 5408 (right panel). The spatial resolution was smoothed to fit the resolution of the H I data. Overlaid in black are the H I intensity contours at 0.015 (3σ), 0.04, 0.1, 0.2, 0.4, 0.8, and 1.6 Jy beam $^{-1}$ (IC 4662) and 0.05 (3σ), 0.1, 0.2, 0.3, 0.5, 0.8, and 1.0 Jy beam $^{-1}$ (NGC 5408). Overlaid in grey are the H I velocity dispersion contours at 25 km s $^{-1}$.

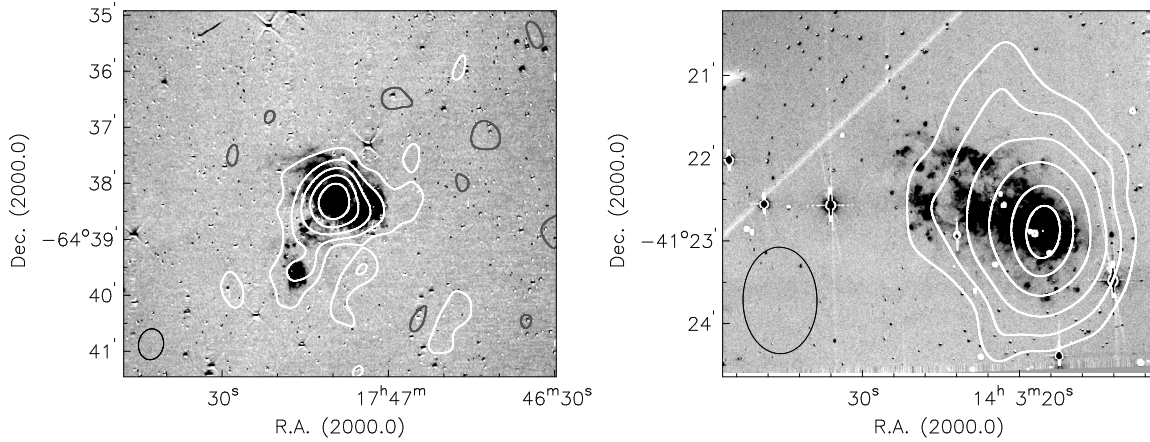


FIG. 6.6: Continuum-subtracted H α images of IC 4662 (left panel) and NGC 5408 (right panel) with the 20 cm radio continuum contours overlaid in white, combining three arrays and using robust weighting ($r=0$), but excluding baselines to CA06. IC 4662: The contour levels are -0.4 , 0.4, 0.8, and 1.6 mJy beam $^{-1}$. Sidelobes from two strong radio sources, PKS 1740–64 and PKS 1746–64 are visible in the lower right corner. NGC 5408: The contour levels are -5 , 5, 10, 20, 40, 80, and 160 mJy beam $^{-1}$.

0.027 M_{\odot} yr $^{-1}$ and $SFR = 0.074 M_{\odot}$ yr $^{-1}$, respectively. The star formation rate of a galaxy can also be estimated from its far-infrared luminosity, L_{FIR} , using $SFR [M_{\odot} \text{ yr}^{-1}] = 0.17 L_{FIR}$ (Kennicutt 1998), with L_{FIR} in units of $10^9 L_{\odot}$. The IRAS 60 μ and 100 μ flux densities, the resulting FIR luminosity, and FIR star formation rate are given in Table 6.5. Following Helou et al. (1985) we calculated the parameter q which is the logarithmic ratio of FIR to radio flux density. For IC 4662 we find $q = 2.54$, for NGC 5408 we find $q = 2.16$, which is in both cases consistent with the mean value of 2.3 for normal spiral galaxies (Condon 1992).

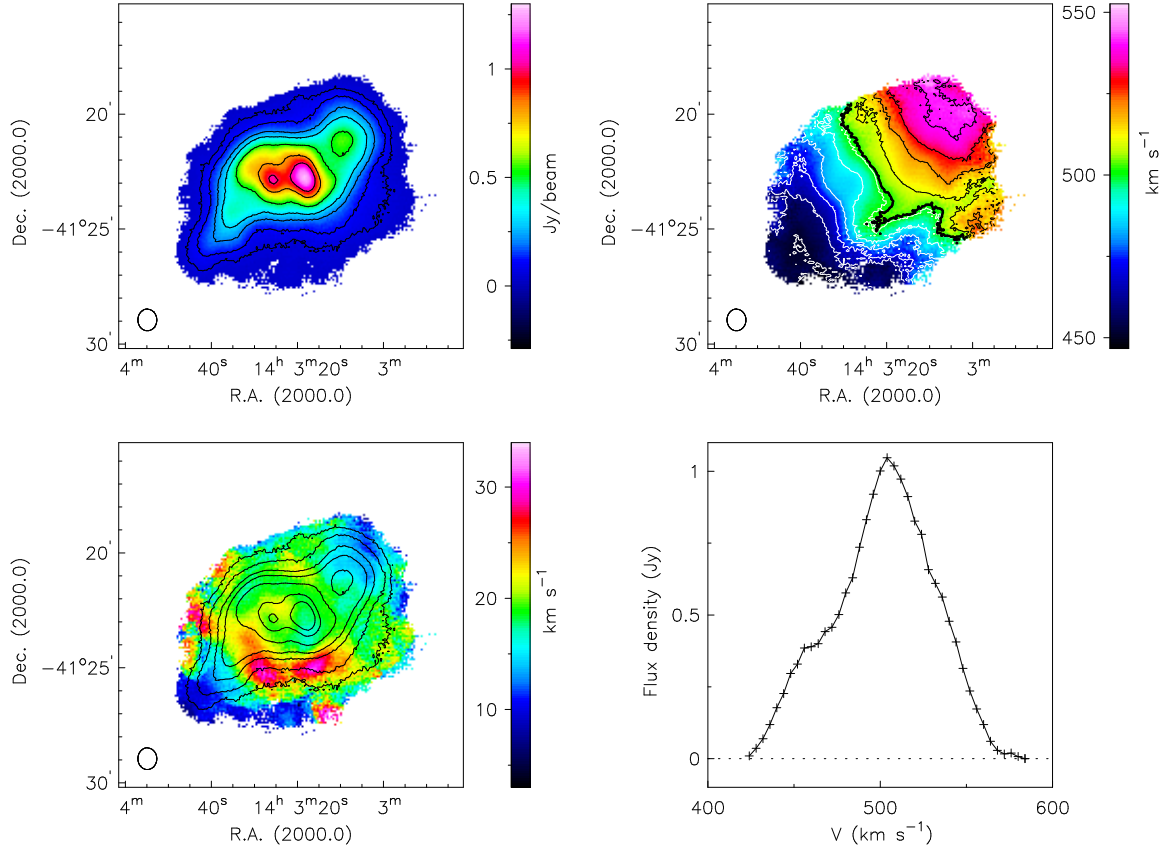


FIG. 6.7: H I moment maps of NGC 5408, combining three arrays and including baselines to CA06, which leads to a synthesised beam of $57'' \times 50''$. **Top left:** The H I distribution. Contours are drawn at 0.05 (3σ), 0.1, 0.2, 0.3, 0.5, 0.8, and 1.0 Jy beam^{-1} where 0.1 Jy beam^{-1} correspond to a column density of $5.0 \times 10^{20} \text{ atoms cm}^{-2}$. **Top right:** The H I velocity field (contour levels range from 440 to 550 km s^{-1} in steps of 10 km s^{-1}). The systemic velocity of 502 km s^{-1} , as calculated from fitting tilted-rings to the velocity field, is marked in bold. **Bottom left:** The H I velocity dispersion, overlaid are the same H I intensity contours as on the 0th moment map. **Bottom right:** The global intensity profile of the galaxy. The short-dashed line marks zero intensity.

TABLE 6.5: Star formation rates from FIR and 20 cm radio continuum measurements.

Optical name	IC 4662	NGC 5408
$S_{60\mu\text{m}}$ [Jy]	8.82	2.83
$S_{100\mu\text{m}}$ [Jy]	11.38	2.96
F_{FIR} [$10^{-11} \text{ erg s}^{-1} \text{ cm}^{-2}$]	43.01	12.94
SFR_{FIR} [$M_{\odot} \text{ yr}^{-1}$]	0.014	0.016
$F_{20 \text{ cm}}$ [mJy]	33	24
$SFR_{20 \text{ cm}}$ [$M_{\odot} \text{ yr}^{-1}$]	0.027	0.074
q -factor	2.54	2.16

F_{FIR} was obtained using the relation by Sanders & Mirabel (1996).

6.4 Kinematic analysis

The comparison of the optical and radio morphology in IC 4662 and NGC 5408 revealed that the optical extent coincides very well with the H I maxima and that both galaxies have a radio continuum source at the location of strongest star formation, which is in case of IC 4662 extended to the southern H II region. Here, the morphology already suggests that the southern H II region is more likely an unusually displaced OB association than an own system because it appears to be connected to the stellar disk by H II regions and diffuse ionised gas and is embedded into the central H I maximum.

Looking at Fig. 6.5, it becomes obvious that the optical appearance of both galaxies is defined by an alignment which is perpendicular to the large-scale H I distribution. The subsequent kinematic analysis will give further information about the gas properties of these two dwarfs.

6.4.1 The kinematics of the neutral gas – the H I velocity fields

The H I velocity field of IC 4662 (see Fig. 6.4, upper right panel) is very disturbed. The overall velocity gradient runs from the north-east with velocities of 220 km s^{-1} to the south-west with velocities of 380 km s^{-1} . It seems as if the direction of the rotation changes from the western part of the galaxy to the eastern part, causing a sudden change of the position angle of almost 90° . This change is possibly correlated with the two perpendicular systems as discussed in Sect. 6.3. The H I velocity dispersion map (lower left panel of Fig. 6.4, overlaid are the H I intensity contours) shows a dispersion of 20 km s^{-1} in the inner and 11 km s^{-1} in the outer parts, except for two maxima with almost 40 km s^{-1} east of the extended H I intensity maximum.

NGC 5408 shows a very symmetric H I velocity field (Fig. 6.7, upper right panel) with a velocity gradient running from the south-east with velocities of 440 km s^{-1} to the north-west with velocities of 550 km s^{-1} . The gradient is very smooth except for both ends of the disk where the velocity field looks slightly warped. South of the intensity maxima a distortion of the velocity field can be seen. The H I velocity dispersion is shown on the lower left panel of Fig. 6.7, overlaid are the H I intensity contours. The mean dispersion is about 20 km s^{-1} with two peaks at 30 km s^{-1} , offset from the H I intensity maxima to the south, but coinciding with the disturbed region in the velocity field.

6.4.2 The kinematics of the neutral gas – the H I rotation curves

In order to derive the rotation curves, a tilted-ring model was fitted to the observed velocity field with the GIPSY task *rotcur* (for a detailed description see App. C). Initial estimates for the relevant parameters are the output of the ellipse fitting task (GIPSY task *ellfit*) and are used as an input for the tilted-ring fits (GIPSY task *rotcur*). The upper left panels of Figs. 6.8 and 6.9 show the results: the black symbols represent the best-fitting parameters derived in an iterative approach from the initial estimates and combining both sides, the error bars define receding and approaching side. A fit with the initial estimates kept fixed is indicated by the green symbols (fixed approach), a fit with the best-fitting parameters kept free is shown by the red symbols (free approach). In order to prove the reliability of the calculated values, a model velocity field was created by using the best-fitting parameters (Figs. 6.8 and 6.9, lower left panels) and afterwards subtracted from the original velocity field (upper right panels). The residual maps are shown on the lower right panels with the outer H I intensity contour and the systemic velocity contour overplotted. We subsequently discuss the resulting rotation curves as well as the kinematic properties of the neutral gas for both galaxy separately.

TABLE 6.6: ATCA H I properties.

Optical name	IC 4662		NGC 5408	
HIPASS name	J1747–64		J1403–41	
	initial estimates	best-fitting values	initial estimates	best-fitting values
dynamical centre:				
α (J2000)	17 ^h 47 ^m 06.4	17 ^h 47 ^m 08.8 ^s	14 ^h 03 ^m 21.6 ^s	14 ^h 03 ^m 20.4 ^s
δ (J2000)	-64° 39' 25"	-64° 39' 00"	-41° 22' 43"	-41° 22' 14"
v_{sys} [km s ⁻¹]	302	310	508	502
i [°]	38	38	55	57
PA [°]	278	214	299	303
F_{HI} [Jy km s ⁻¹]		103		59
$\log M_{\text{HI}}$ [M_{\odot}]		8.2		8.5
H I diameter [']		15.0 × 11.5		10.0 × 6.3
" [kpc]		10.6 × 8.2		14.0 × 8.8
H I / opt. ratio		5 × 7		4
v_{rot} [km s ⁻¹]		107		53
$\langle \sigma \rangle$ [km s ⁻¹]		11/20		18
σ_{Peak} [km s ⁻¹]		36.8		31.7
$r_{\text{HI,max}}$ [kpc]		6		9.5
M_{dyn} [$10^9 M_{\odot}$]		15.9		6.2

IC 4662

As already mentioned above, the H I velocity field of IC 4662 is very disturbed, which made it difficult to fit a rotation curve. Nevertheless, we tried to derive values for the different kinematic parameters. The upper left panel of Fig. 6.8 shows the results for the different approaches. The error bars, indicating receding and approaching side, are very large, which means that the difference between receding and approaching side is quite high. The fixed approach shows a completely different behaviour as the iterative or even the free approach. The curve is very flat in the inner 100'' and rises slowly over the next 200''. The iterative and free approach show a steeper rotation curve that immediately begins to rise coming to a plateau at 300'', which is what we would expect from the rotation curve of a dwarf galaxy (for a comparison see Figs. 4.6 and 5.6, upper left panels). From a radius of 300'' on, the scatter in the velocities becomes even larger, which is due to the decreasing filling factor of the rings (see discussion in App. C).

The iterative approach gives us an inclination angle of 38°, a position angle of 214°, and a systemic velocity of 310 km s⁻¹ (see also Table 6.6). The latter is a few km s⁻¹ higher as expected from the H I profile. HIPASS observations by Koribalski et al. (2004) also reveal a lower v_{sys} of 302 ± 3 km s⁻¹. This deviation results from the different ways of how v_{sys} was measured. Usually, both methods – calculating v_{sys} from the widths of the H I profiles or by fitting tilted-rings to the velocity field – should lead to the same value, at least in case of a “well-behaved” galaxy. IC 4662, however, is far away from being a regular galaxy. Especially, the velocity field is quite disturbed, which most probably leads to the different value for v_{sys} . For the analysis presented here, we decided to work with the higher value of 310 km s⁻¹.

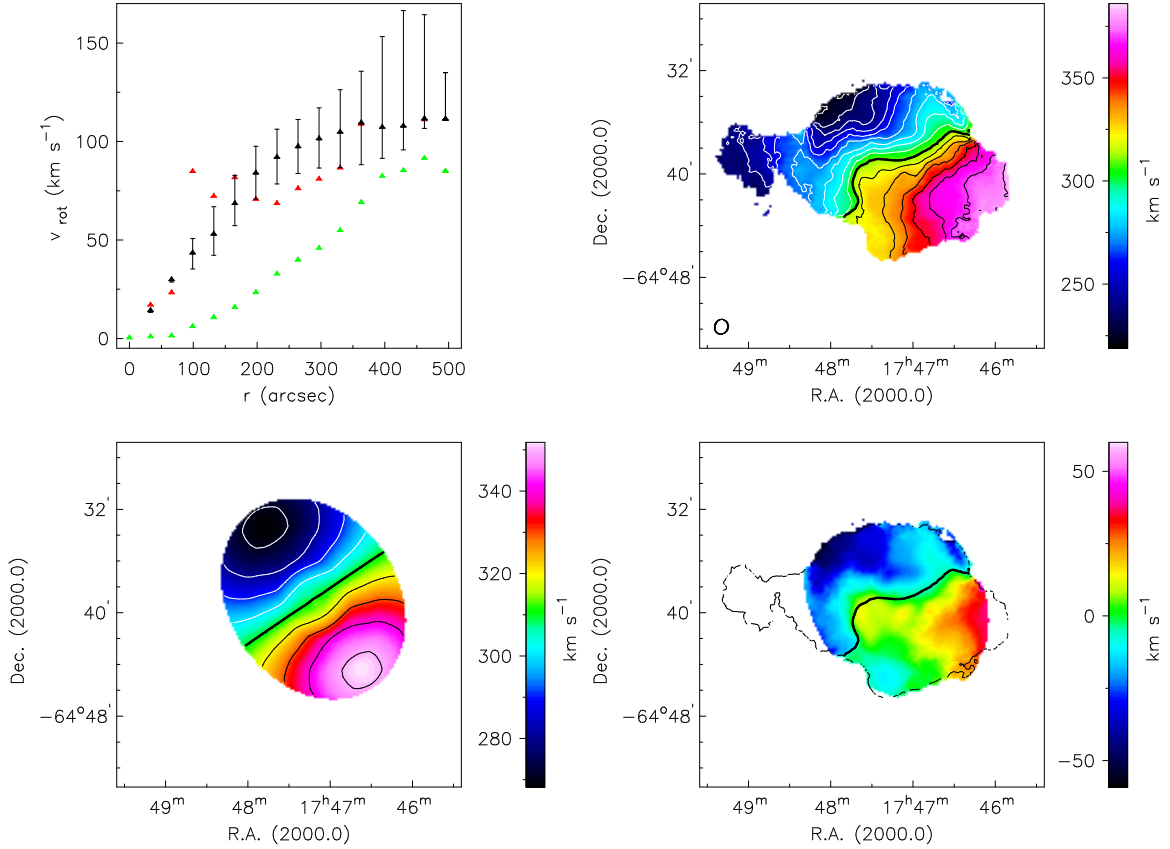


FIG. 6.8: The H I rotation curve of IC 4662 created by fitting a tilted-ring model to the observed velocity field. **Top left:** Different approaches for deriving the rotation curve. The black symbols represent the iterative approach, the error bars indicate receding and approaching side. The green curve was derived by taking the initial estimates and keeping them fixed (fixed approach), the red curve by taking the best-fitting parameters and keeping them free (free approach). For a more detailed description see App. C. **Top right:** The observed H I velocity field. **Bottom left:** The model velocity field created by taking the best-fitting parameters. **Bottom right:** The residual map after subtracting the model from the original velocity field.

The residual map (lower right panel of Fig. 6.8) shows that the inner part is well represented by the model velocity field, whereas the outer parts in the east and west are badly fitted by the derived best-fitting parameters.

NGC 5408

NGC 5408 has a slowly rising rotation curve coming to a plateau at a radius of $250''$. The error bars, i.e., receding and approaching side, show a very similar kinematic behaviour. The initial estimates are already very close to the best-fitting parameters. The free approach is also in good agreement with the other two approaches except for some scatter from $50''$ to $100''$. This is still far away from the disturbed region, which can therefore not explain the scatter. From a radius of $300''$ on, the deviations become larger, which is again due to the strongly decreasing filling factor, but probably also to the warped structure. Beyond $350''$, the rotation curve tends to rise again, although the receding side declines.

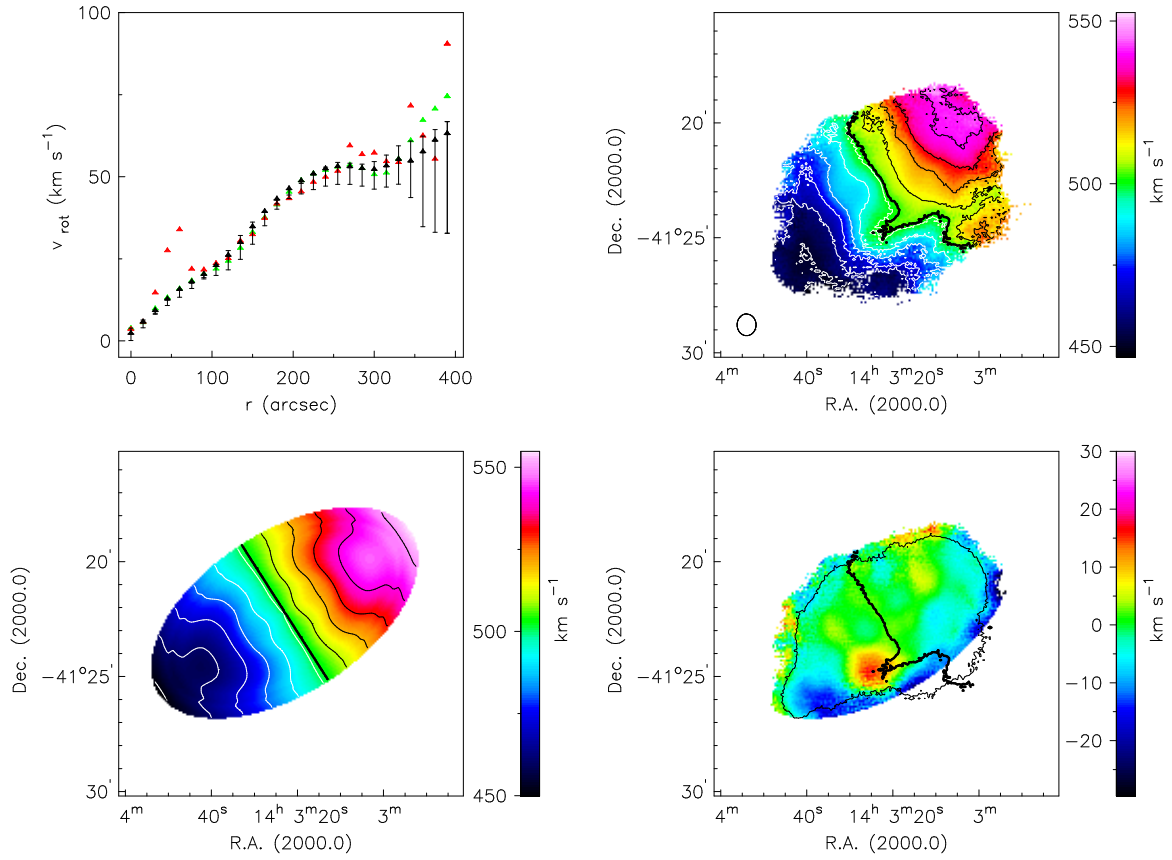


FIG. 6.9: NGC 5408: The same as in Fig. 6.8.

The iterative approach gives an inclination angle of 57° , a position angle of 303° , and a v_{sys} of 502 km s^{-1} (see also Table 6.6). This time, the systemic velocity is slightly lower than the one measured in HIPASS (Koribalski et al. 2004), but agrees well with the H I line profile.

We again chose the best-fitting parameters (see Table 6.6) to create the model velocity field and subtracted it from the observed velocity field. The residual map shows that the original velocity field is very well represented by these parameters (Fig. 6.9, lower right panel). The residuals are generally at $\pm 5 \text{ km s}^{-1}$, except for one region in the south with a value of 15 km s^{-1} . This region coincides with the already mentioned distortion in the velocity field and the high velocity dispersion. A closer look at the velocity profiles reveals a second component with an offset of 35 km s^{-1} blue-shifted. This shall be examined in more detail in Sect. 6.4.3.

6.4.3 The kinematics of the ionised gas – long-slit spectroscopy of the $\text{H}\alpha$ line

As already mentioned in Sect. 6.2.2, we performed a Gaussian decomposition of the long-slit spectra by interactively fitting Gaussian profiles to the observed emission lines (see also App. A). Figure 6.10 shows example spectra of IC 4662 (slit 3 at $r = -50''$) and NGC 5408 (slit 1b at $r = 0''$), respectively. Two Gaussian profiles were fitted to the $\text{H}\alpha$ line (blue and red long-dashed line). The sum of both components is plotted in green and fits the observed spectrum very well. From all spectra, we created position-velocity (pv) diagrams. The corresponding H I velocities were taken from the H I data cubes

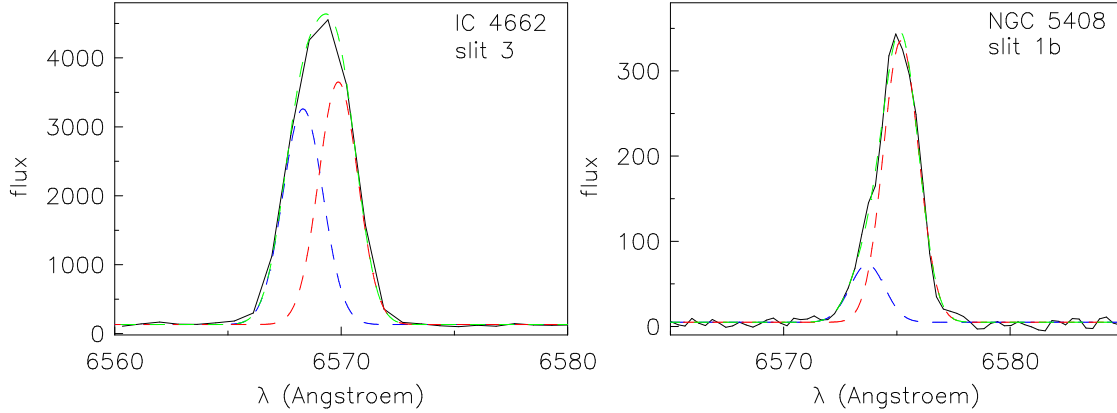


FIG. 6.10: Example spectra of IC 4662 (slit 3 at $r = -50''$) and NGC 5408 (slit 1b at $r = 0''$). In both cases, the $H\alpha$ line is split into two components (blue and red long-dashed lines). The sum of both Gaussian fits is plotted in green and is in good agreement with the observed spectrum.

and are, as well as the $H\alpha$ velocities, not corrected for inclination. The results are shown in Figs. 6.11 and 6.12. Both figures contain the $H\alpha$ image of the galaxies, overplotted are the slit positions. Position 0 in the pv diagrams is marked by a small circle. $H\alpha$ velocities are plotted with + symbols, the HI velocities are indicated by a solid line. Again, we discuss the results for both galaxies separately.

IC 4662

Three spectra at different locations of IC 4662 were obtained (Fig. 6.11, upper panel). The lower part of Figure 6.11 shows the resulting pv diagrams. Parts of the ionised gas follow the HI velocities, but also some deviations from the HI can be seen. Spectrum 1 splits at two positions into two components, one red-shifted and one blue-shifted, both with an offset in comparison to the neutral gas of about 40 km s^{-1} . The line splitting at $-150''$ coincides with the southern H II region, the line splitting at $-60''$ coincides with the main complex of H II regions in the north.

The southern H II region has been and still is a subject of great interest. Due to its chemical composition, which is different from the main complex, and its isolated position, it is considered to be a separate system interacting with IC 4662. However, both from the morphology (see Sect. 6.3) and the kinematics it can be concluded that it most probably belongs to IC 4662. Strong evidence is given on the pv diagrams as the southern H II region and the northern H II complex show the same behaviour concerning outflowing gas. As mentioned above, the $H\alpha$ line is split into a red- and a blue-shifted component at both locations. The velocity offsets to the corresponding HI velocities agree very well with each other.

The $H\alpha$ emission in spectrum 2 follows the HI velocities along the whole slit except for the last part which seems to be offset by 20 km s^{-1} blue-shifted. This region coincides with the filamentary structure to the north-east of the main body where outflowing material is expected. Spectrum 3 looks very chaotic at first glance. Along the whole slit, the $H\alpha$ emission splits into two components, one slightly below the HI velocity, the other one red-shifted by about 75 km s^{-1} . Spectrum 2 also shows a hint of this highly red-shifted component.

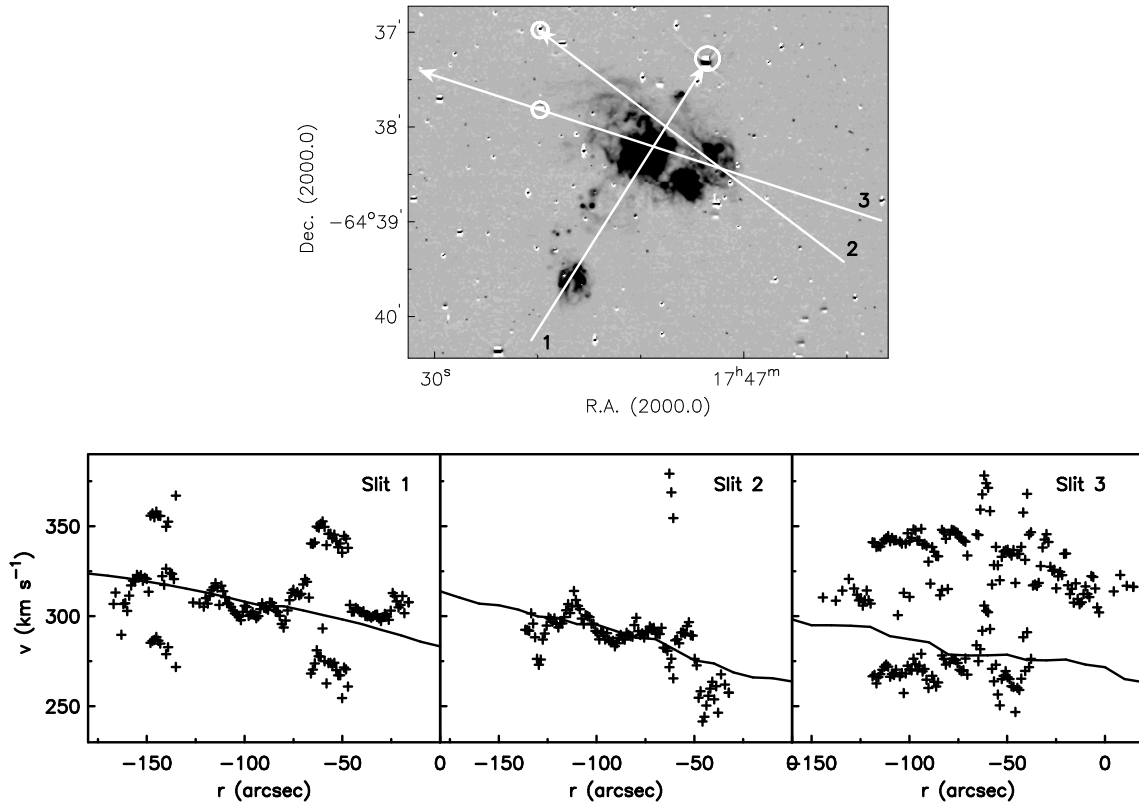


FIG. 6.11: Pv diagrams of IC 4662. The upper panel shows the continuum-subtracted $H\alpha$ image. White arrows indicate the slit positions, white circles mark position 0. The lower three panels display the pv diagrams of the $H\alpha$ emission. The + symbols represent the $H\alpha$ velocities obtained from the spectra, the solid line the H I velocities obtained from the ATCA H I data cube.

NGC 5408

As already mentioned in Sect. 6.2.2, spectra from two different observations of NGC 5408 were kinematically analysed. Figure 6.12 shows the pv diagrams. The upper row contains our own data, the lower left panel represents the archival data.

The data confirm what was already visible on the $H\alpha$ image (see Fig. 6.16 of App. 6.A): NGC 5408 shows outflowing material distributed over the whole disk. The centre of the $H\alpha$ emission in the southwest harbours a strong blue-shifted component with a velocity offset of about 60 km s^{-1} in comparison to H I (see slit 1a). In spectrum 1b (the archival higher resolution spectrum), the blue-shifted component is in fact even more than 60 km s^{-1} offset from H I. This is most probably a resolution effect. Additionally, spectrum 1b shows a red-shifted component in this region with a similar offset of about 50 km s^{-1} . This component cannot be seen in the lower resolution data, which is again a resolution effect. The eastern H II region shows a blue-shifted component with an offset of 30 to 50 km s^{-1} in slit 1b and slit 3. And finally, slit 2 and slit 3 reveal a red-shifted component in the northernmost part of the galaxy with a velocity offset of about 30 to 40 km s^{-1} , which might be the counterpart of the blue-shifted outflow.

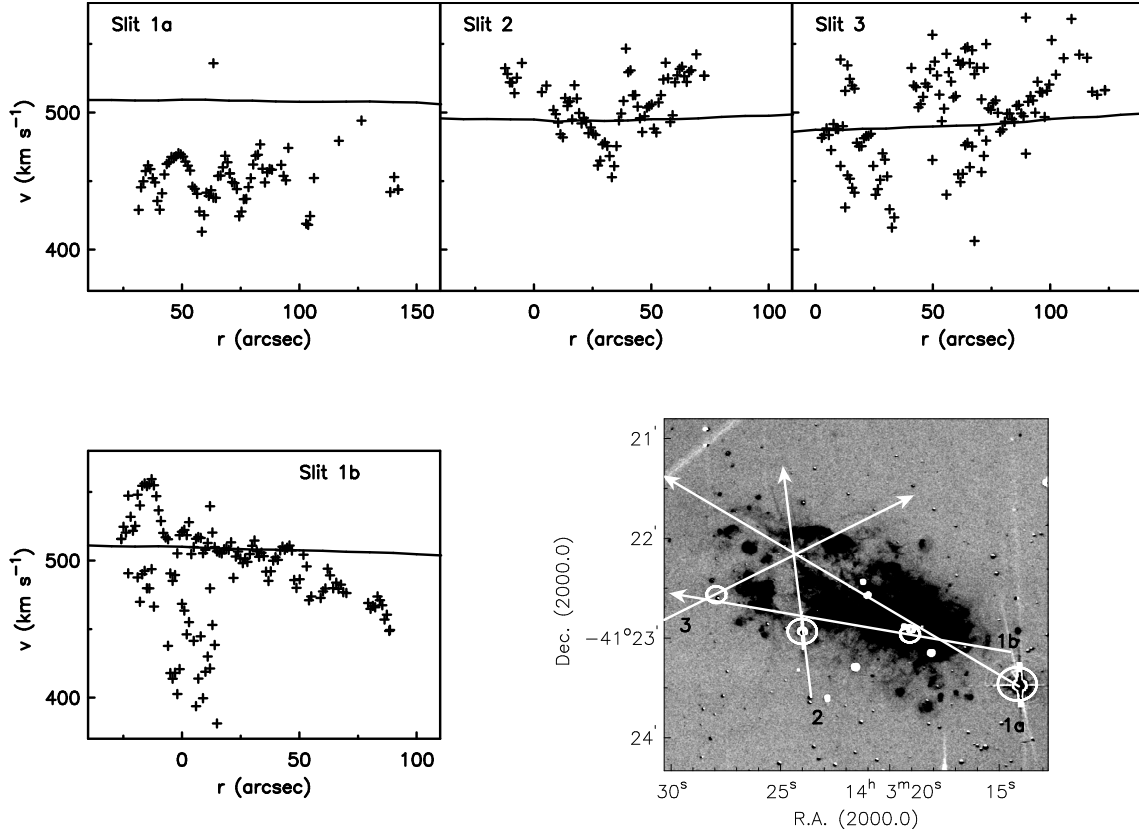


FIG. 6.12: P-v diagrams of NGC 5408. The upper part shows the three slit positions that were obtained by us, the lower left panel the archival data. The lower right panel displays the continuum-subtracted H α image. Again, all slit positions are indicated by white arrows. Position 0 is marked by white circles.

6.4.4 A comparison of the H I with the H α kinematics

We had a closer look at the H I kinematics of both galaxies by performing a Gaussian decomposition as described in App. A. Figures 6.13 and 6.14 show the resulting maps: a map with the blue-shifted gas on the left, a map with the main component (component of highest intensity) in the middle and a map with red-shifted gas on the right. Note that regions where we did not find a blue- or redshifted component were filled with the main component. The velocities were averaged over $70'' \times 70''$ in case of IC 4662 and $50'' \times 50''$ in case of NGC 5408, which roughly corresponds to one beam size. In white, an H I velocity dispersion contour at 25 km s^{-1} is overlaid as well as the outer intensity contour of the H α image.

IC 4662

We see line-splitting of the H I close to the centre of the galaxy and especially north of the stellar disk. East of the optical galaxy and coinciding with the major peak in H I velocity dispersion, the H I shows a red-shifted component with a velocity offset of 60 km s^{-1} . At the position of the southern H II region, the H I emission is split into the main component at 315 km s^{-1} and a blue-shifted component at 280 km s^{-1} . In H α we even see three components, the main component at 325 km s^{-1} , a blue-shifted component at 285 km s^{-1} and a red-shifted component at 360 km s^{-1} . At the position of the main H II region complex, the H I is again split into two component, the main component at 300 km s^{-1} , the

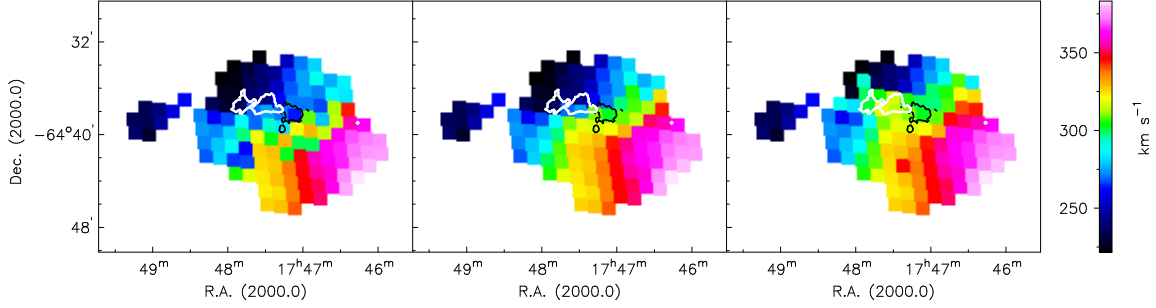


FIG. 6.13: Gaussian decomposition of the HI in IC 4662. Blue-shifted (left panel), main (middle panel) and red-shifted (right panel) components of the HI velocities are shown. Note that regions where we did not find a blue- or redshifted component were filled with the main component. We averaged the velocities over $70'' \times 70''$, which roughly corresponds to one beam size. Overlaid in white are the HI velocity dispersion contour at 25 km s^{-1} as well as the outermost $\text{H}\alpha$ intensity contour in black.

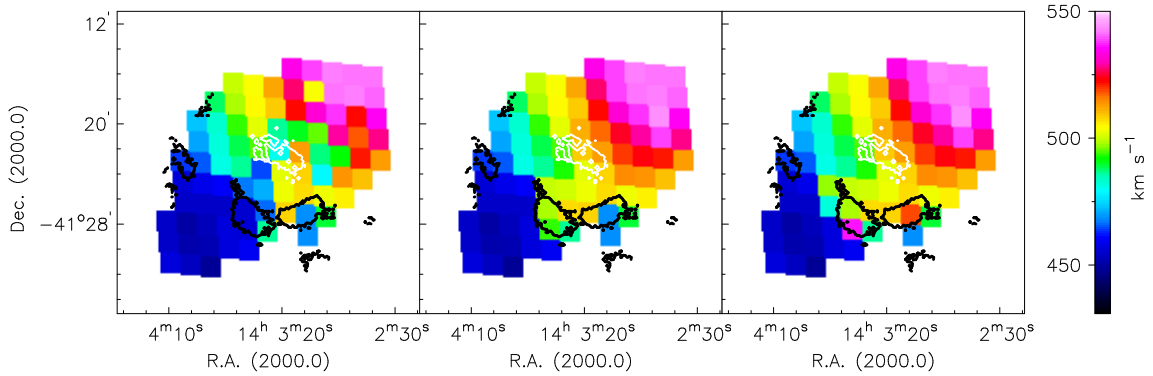


FIG. 6.14: Gaussian decomposition of the HI in NGC 5408. The same as in Fig. 6.13. We averaged the velocities over $50'' \times 50''$, which roughly corresponds to one beam size.

blue-shifted one at 260 km s^{-1} . The $\text{H}\alpha$ line reveals a blue-shifted component at 260 km s^{-1} and a red-shifted component at 350 km s^{-1} . This means firstly that also the HI associated with the southern H II region and the main H II region complex shows the same kinematic behaviour. Secondly, the HI and $\text{H}\alpha$ velocities agree very well with each other, revealing a blue-shifted component with an offset of about 40 km s^{-1} . At the location of the stellar disk, the red-shifted, probable counterpart is only visible in $\text{H}\alpha$, although a bit further to the east the HI shows a red-shifted outflow with an expansion velocity of 60 km s^{-1} (see above). Looking at the HI intensity distribution close to the stellar disk (see Fig. 6.4, upper left panel), a significant drop in intensity at the position of the outflowing gas becomes visible. We saw a similar behaviour in NGC 2366 and NGC 4861: probably, the neutral gas has already been blown away from the location of the stellar disk and the inner part has partly or even fully been ionised, which means that the HI content is now significantly reduced. A similar feature can be seen west of the optical galaxy at two minor velocity dispersion peaks. Studies have been made where about 50 so-called HI holes have been found in a single dwarf galaxy (see, e.g., Walter & Brinks 1999).

In addition to the low HI column density, we also need to have in mind that the spatial resolution of the ATCA data is very low (the whole optical extent of IC 4662 only corresponds to two beam sizes), which might be the reason why we miss the the red-shifted HI gas associated with the stellar disk.

NGC 5408

In the eastern part of the optical galaxy, the HI shows an additional component at 485 km s^{-1} in comparison to the main component at 515 km s^{-1} leading to an offset of 30 km s^{-1} . This fits with the results from the spectroscopy, although we again fail to detect a red-shifted component in the HI. The reasons are probably the same as for IC 4662.

In the south of the HI distribution and more than 2 kpc away from the optical galaxy, the HI splits into two components, one following the rotation with about 500 km s^{-1} and a blue-shifted one with 465 km s^{-1} . The highest HI velocity dispersion as well as the large residuals after subtracting the velocity model from the observed velocity field are found to be in the same area a bit south of the optical galaxy. The HI intensity distribution does not show any peculiarities, like, e.g., an HI hole.

6.5 Outflow or galactic wind?

In order to make predictions about the fate of the outflowing gas structures we compared the expansion velocities with the escape velocities of the galaxies derived by using the cored pseudo-isothermal (ISO) halo model. As discussed in Sect. 4.5.4, only the ISO halo was used for estimating the escape velocity as it represents the shape of the rotation curves in the inner parts much better than the NFW halo. Following Eq. 4.2, the escape velocity was calculated using the circular velocity derived from the HI rotation curves. Again, two estimates for the maximal halo radius r_{max} were made: as a lower limit we took the HI radius and as a more physical assumption we took twice the HI radius. In case of IC 4662, we chose an r_{max} of 6 kpc (dotted line) and 12 kpc (solid line), respectively, for NGC 5408 we took an r_{max} of 9.5 kpc (dotted line) and 19 kpc (solid line), respectively. Figure 6.15 shows the results for both galaxies. The observed rotation curve is indicated by small grey triangles. The outflows with their distances from the dynamical centre and their velocities compared to the HI velocities are marked by large black triangles.

In both galaxies, the expansion velocities of the outflows stay far below the escape velocity. A higher r_{max} results in an increase of the escape velocity. Probably, the radius of the dark matter halo r_{max} is much higher than assumed, which means that the escape velocities become even higher. The curve with $r_{\text{max}} = r_{\text{HI,max}}$ gives therefore a lower limit for the escape velocity values.

In IC 4662, the outflow velocities of up to 75 km s^{-1} are quite high in comparison to NGC 2366 (see Chap. 4) and NGC 4861 (see Chap. 5) with an average outflow velocity of 30 km s^{-1} . Additionally, the galaxy has a rotation velocity of 107 km s^{-1} , which is twice as high as in the ones of NGC 2366, NGC 4861, and NGC 5408. This results in a high dynamical mass, which significantly increases the gravitational potential. Thus, although IC 4662 has the highest outflow velocities, the factor of $v_{\text{exp}}/v_{\text{esc}}$ is similar than the one of the other three galaxies.

NGC 5408 shows expanding gas of 60 kms, but only close to the dynamical centre where the escape velocities are the highest. However, we also found expanding neutral gas at a distance of 4.3 kpc from the dynamical centre. Although the expansion velocity of 35 km s^{-1} is low in comparison to the other outflows in this galaxy, it is only 20 km s^{-1} away from the value of the escape velocity. This means that because the escape velocities at distances of 2 kpc and more from the centre are

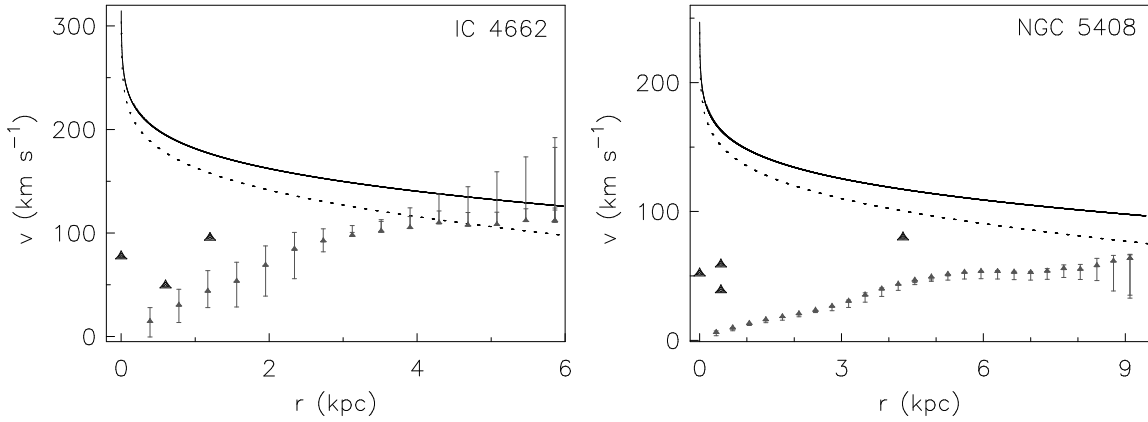


FIG. 6.15: Outflow or galactic wind? The expansion velocities of the outflowing gas structures in IC 4662 (left panel) and NGC 5408 (right panel) are compared with the escape velocities calculated by using the pseudo-isothermal halo model. IC 4662: the escape velocity is calculated for an isothermal halo of $r_{\text{max}} = 6$ kpc (dotted line), which fits the size of the H I distribution, and $r_{\text{max}} = 12$ kpc (solid line). NGC 5408: the escape velocity is calculated for an isothermal halo of $r_{\text{max}} = 9.5$ kpc (dotted line), which fits again the size of the H I distribution, and $r_{\text{max}} = 19$ kpc (solid line). The observed rotation curve is indicated by small grey triangles. The error bars represent receding and approaching side. The expanding gas structures are marked by black large triangles.

significantly lower than in the inner 1 kpc, it is more likely for an expanding gas structure to leave the gravitational potential. Simulations dealing with superbubble blowout (e.g., Mac Low & Ferrara 1999) predict that at least a small fraction of the gas escapes into the IGM. This leads to the following conclusions: There might be gas further away from the main body of the galaxies with higher expansion velocities that cannot be detected by us due to its low surface density. Usually, we only see the edges of a superbubble or supershell. The other explanation would be that these dwarf galaxies are too young to have accelerated the gas to such high velocities and distances or the energy input is too low.

6.6 Summary

Radio and optical data of the two peculiar dwarf galaxies IC 4662 and NGC 5408 were analysed in order to compare the morphology and the kinematics of the neutral and ionised gas.

In both galaxies, we found several outflows both in H α and H I with expansion velocities of 30 km s^{-1} up to 75 km s^{-1} . Although the H I velocity field of IC 4662 is much more disturbed than the one of NGC 5408, both galaxies show the same properties concerning outflowing gas. The expansion velocities are of the same order, the outflows are scattered over the whole stellar disk, but in the end it is very unlikely that they will be blown away as the expansion velocities stay far below the escape velocities of the host galaxies. Only in NGC 5408, we found an outflow in H I with no optical counterpart, at a distance of 4.3 kpc from the dynamical centre and with an expansion velocity of 35 km s^{-1} . At this distance from the dynamical centre, the escape velocity has significantly dropped so that the outflow still remains below the escape velocity, but closer to it than all the other outflows detected in this galaxy.

The most peculiar feature in IC 4662 is the southern H II region which has been studied by, e.g., Hidalgo-Gómez et al. (2001) who found a different oxygen abundance in comparison to the main H II region complex. This rises the question whether the H II region is an own system or just an unusually placed OB association. The comparison of the optical and radio morphology showed that this H II

region is embedded in the highest column density HI together with the main H II region complex. The 20 cm radio continuum also shows an extension to the southern H II region. The long-slit spectra reveal a blue- and a red-shifted component in H α both at the position of the southern H II region and throughout the northern main H II region complex with an expansion velocity of 40 km s $^{-1}$. The HI line is split at the same positions in a blue-shifted and the main component. This similar kinematic behaviour as well as the fact that the southern H II regions fits well into the radio morphology strengthens the interpretation that this H II region is part of IC 4662.

6.A Appendix: H α

Here, the continuum-subtracted H α images are again presented in an enlarged version, without any overlays, and with a contrast that emphasises the small-scale structure (see Fig. 6.16).

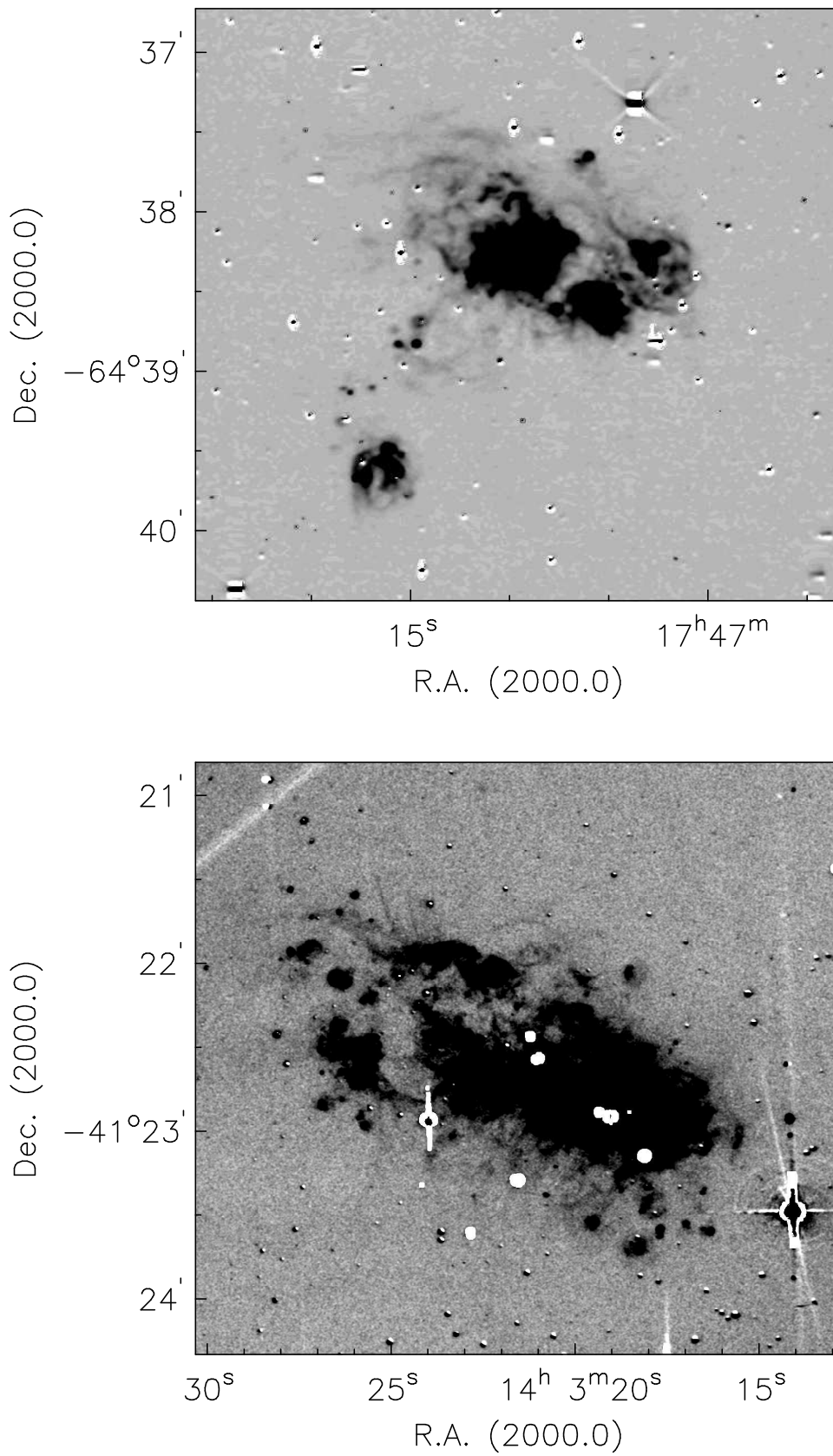


FIG. 6.16: Continuum-subtracted H α images of IC 4662 and NGC 5408. The contrast is chosen in a way to demonstrate the small-scale structures.

Dark matter in dwarf galaxies

Abstract

The cusp-core discrepancy is one of the major problems which result from comparing the observations of the mass distribution with the predictions of Cold Dark Matter theories. Simulations predict a cuspy density slope in the inner parts of galaxies, whereas observations of dwarf and low surface brightness galaxies show a constant density core.

VLA and ATCA HI data have been obtained for a sample of four nearby irregular dwarf galaxies and rotation curves have been derived. We here complement the inner parts of the HI rotation curves by high-resolution H α data from Fabry-Perot observations and long-slit spectroscopy. In order to look at the behaviour of the inner part of the rotation curves, we fit NFW and pseudo-isothermal halo models to the data using a χ^2 minimisation. We model the minimum-disk, the minimum-disk + gas, and the maximum-disk cases. The surface photometry is taken from the literature in order to derive the rotation curve for the stellar component.

In all cases, the observed rotation curves can better be described by a cored pseudo-isothermal halo. Furthermore, the fits improve by including gas and stars, which means that the velocity contribution from the baryons in the inner parts is significant enough to not be neglected.

7.1 Introduction

Early observations of the rotation curves of spiral galaxies showed that the dynamical mass is too high to be explained by the amount of luminous matter alone (e.g., Bosma 1978; Rubin et al. 1978). Therefore, the so-called “dark” matter has since then become part of modern cosmology. In order to explain and describe the properties of the Universe, a cosmological constant Λ and a form of collisionless Cold Dark Matter (CDM) have been involved. Simulations like, e.g., the Millennium Simulation by Springel et al. (2005) have been very successful in describing the observed large-scale structures in the Universe (Spergel et al. 2003; Spergel et al. 2007), but they do not work properly on galaxy scales.

The main problems are the missing satellite problem (Moore et al. 1999) and the cusp-core discrepancy (e.g., de Blok & Bosma 2002). Numerical simulations predict cuspy haloes with a density

distribution described by a power law $\rho(r) \sim r^\alpha$ with $\alpha = -1$ (e.g., Navarro et al. 1996) to $\alpha = -1.5$ (e.g., Moore et al. 1998, 1999). This cusp leads to a steeply rising rotation curve. However, observations of dwarf and low surface brightness galaxies show that real rotation curves rise less steeply than predicted by CDM simulations (e.g., de Blok & Bosma 2002). Similar conclusions have also been made from observations of high surface brightness disk galaxies (Salucci 2001). At small radii (typically few kpcs), the mass distribution can better be described by a central, constant-density core (e.g., de Blok & Bosma 2002).

This interpretation has been met with skepticism as cored haloes lack theoretical and cosmological motivation. Systematic effects in the data like beam smearing, slit misplacement and non-circular motions have also been used to argue against the presence of cored haloes (van den Bosch et al. 2000; Swaters et al. 2003). However, repeated one-dimensional long-slit spectra observed by independent observers at different telescopes (de Blok et al. 2003) as well as high-resolution $H\alpha$ observations using a two-dimensional velocity field (e.g., Kuzio de Naray et al. 2008; Spano et al. 2008) also suggest the presence of a dark matter core in the inner parts of disk galaxies. Non-circular motions can indeed affect the results of rotation curve studies as it is assumed that the particles travel on circular orbits. Recent observations by Gentile et al. (2005) and Trachternach et al. (2008a), however, show that non-circular motions are typically of the order of few km s^{-1} , i.e., too small to explain the cusp-core discrepancy.

In this chapter, the cusp-core discrepancy is addressed by using the rotation curves derived from H I synthesis data of four nearby irregular dwarf galaxies. In the inner few kpcs, high-resolution $H\alpha$ data are added to the H I rotation curves. In principle, H I synthesis observations are well suited for this study as the H I usually has a higher filling factor than the patchy and diffuse $H\alpha$ distribution. However, de Blok (2004) shows that a spatial resolution better than 1 kpc is needed to distinguish between a cusp and a core. As this is only given for the H I data of NGC 2366, $H\alpha$ velocities from Fabry-Perot (FP) observations (NGC 4861) and from long-slit spectra (IC 4662 and NGC 5408) are used to replace the inner parts of the H I rotation curves.

This chapter is organised as follows: in § 7.2, the data are shortly described. In § 7.3, we explain the derivation of the $H\alpha$ rotation curves. Section 7.4 contains the theoretical background of the mass models, which is followed by a discussion of the results in § 7.5. Section 7.6 gives a short summary.

7.2 The data

Rotation curves derived from H I synthesis observations of four nearby irregular dwarf galaxies are used for the mass decomposition. The data of NGC 2366 are part of the The H I Nearby Galaxy Survey (THINGS, Walter et al. 2008) and were obtained with the VLA in three different configurations leading to a high spatial resolution of $13'' \times 12''$. NGC 4861 was also observed with the VLA in two configurations. The H I data of IC 4662 and NGC 5408 are part of the Local Volume H I Survey (LVHIS) and were obtained with the ATCA in three different configurations. Some observational details are given in Table 7.1. The phase and flux calibration as well as the separation of the continuum from the H I line emission were performed with AIPS in the case of NGC 4861 and with MIRIAD for IC 4662 and NGC 5408. We then used MIRIAD to combine the different arrays and to create the H I cubes. The data of NGC 2366 had already been calibrated and combined by the THINGS team.

Additionally, $H\alpha$ data are used for the inner parts of the rotation curves. FP interferometry of NGC 2366 and NGC 4861 was performed with the Marseille's scanning FP attached to the 1.93m telescope at the Observatoire de Haute-Provence, France. The data reduction was carried out with

TABLE 7.1: The main observational parameters.

Parameter	NGC 2366	NGC 4861	IC 4662	NGC 5408
H I data				
Telescope	VLA	VLA	ATCA	ATCA
Arrays	B+C+D	C+D	EW367+750A+1.5D	375+750D+1.5A
Spectral resolution [km s ⁻¹]	2.6	5.2	4	4
Synthesised beam ["]	13 × 12	31 × 30	70 × 62	57 × 50
Optical data				
Telescope	1.93m OHP	1.93m OHP	ESO NTT	ESO NTT
Instrument	FP	FP	EMMI	EMMI
Spectral resolution [km s ⁻¹]	50	50	112	60/112
Seeing ["]	3.5	3.5	1	1/1

ADHOCw (see Chaps. 2, 4 and 5). For IC 4662 and NGC 5408, we obtained long-slit spectra with the ESO NTT on La Silla equipped with EMMI. The data reduction was performed with IRAF (see Chap. 6). Some observational details are again summarised in Table 7.1.

7.3 Rotation curves

7.3.1 H I rotation curves

The H I rotation curves have already been derived in Chaps. 4 to 6 by fitting a tilted-ring model to the H I velocity fields with the GIPSY task *rotcur*.

7.3.2 H α rotation curves

As the spatial resolution of optical data is much higher than the spatial resolution of radio data, a derivation of the H α rotation curve could help to improve the quality of the H I curve in the inner parts. For the outer parts, we still depend on the H I rotation curve as the neutral gas is much more extended than the ionised gas. Recent publications show that, e.g., for a cusp-core debate, the inner 1 to 2 kpc need a very high spatial resolution (de Blok 2004), which cannot be achieved with single dish radio data and which is even difficult to obtain with the current radio interferometers. The THINGS survey is one of the first to contain H I data of a number of nearby galaxies with a high spatial resolution. Of course, this also depends on the distance of the objects and currently, only nearby galaxies can be resolved better than 1 kpc.

In order to directly compare both curves, the same parameters (centre coordinates, inclination, position angle, systemic velocity) have to be chosen. For NGC 2366 and NGC 4861, we used the FP data cubes and derived a rotation curve as described in App. C. For IC 4662 and NGC 5408, we obtained slit spectra, which give us only a rough estimate of an H α rotation curve because we assume that a slit spectrum positioned along the major axis gives us the rotation curve. This is, of course, only true if the galaxy has a regular rotation pattern. Furthermore note that, as the purpose of the slit spectra was different from using them for deriving a rotation curve (see Chap. 6), it is coincidence if

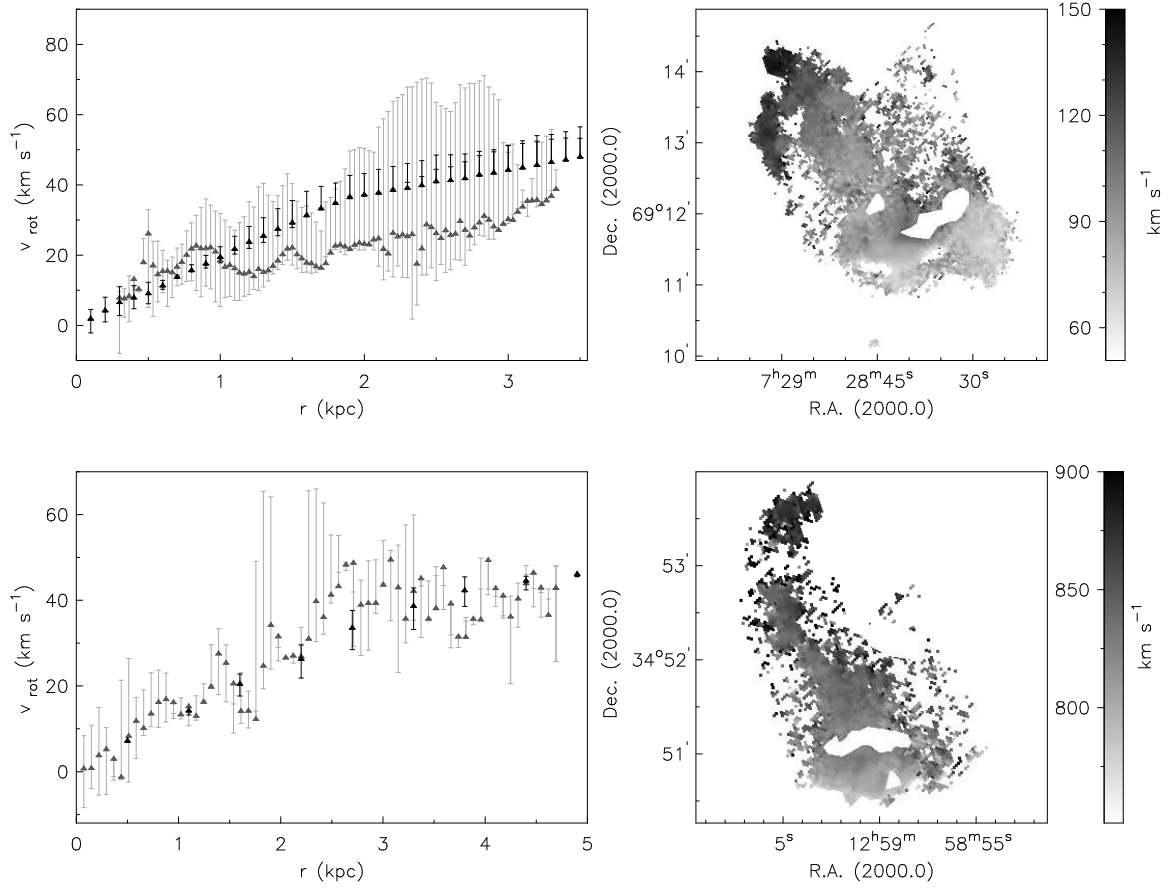


FIG. 7.1: A comparison of the H I and the H α rotation curve (left panels). H I velocities are marked in black with the values for receding and approaching side indicated by the error bars. In dark grey the same for the H α velocities. The right panels show again the H α velocity field. Regions of red- or blue-shifted emission are removed to improve the quality of the rotation curve.

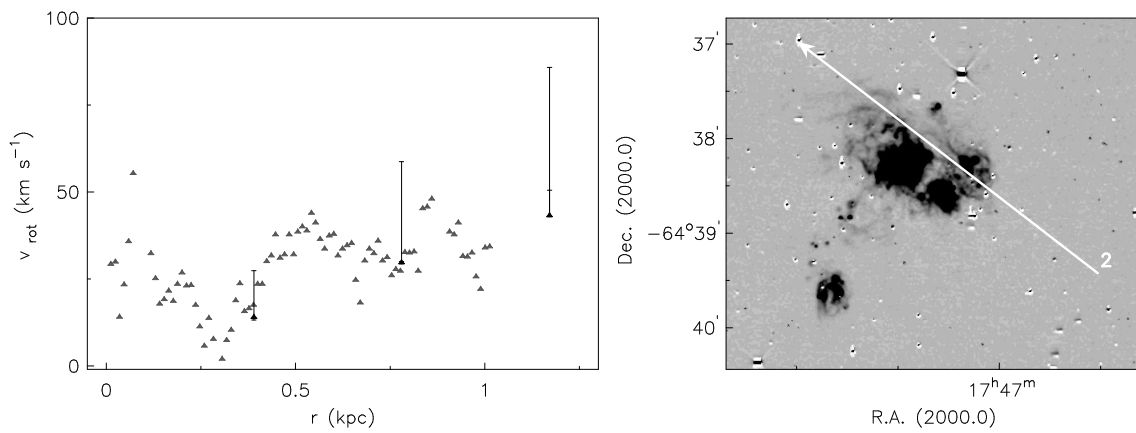


FIG. 7.2: A comparison of the H I and the H α rotation curve of IC 4662 (left panel). H I velocities are marked in black with the values for receding and approaching side indicated by the error bars. The velocities obtained from slit 2 (see right panel) were taken to estimate the H α rotation curve (dark grey symbols).

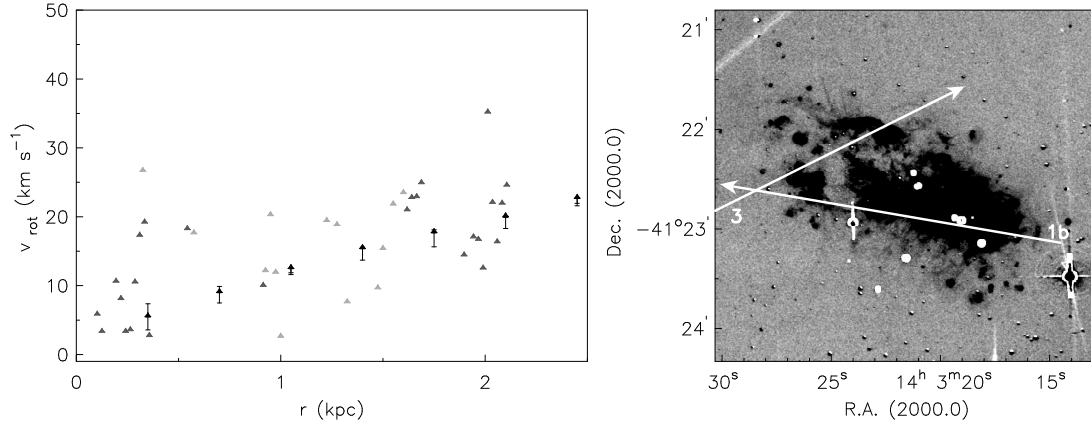


FIG. 7.3: A comparison of the H I and the H α rotation curve of NGC 5408 (left panel). H I velocities are marked in black with the values for receding and approaching side indicated by the error bars. The velocities obtained from two slit positions (see right panel) were taken to estimate the H α rotation curve. The values of slit 3 are marked by symbols in dark grey, the values of slit 1b by symbols in light grey.

their position angles correspond to the H I position angles. Thus, we sometimes had to deproject the slits onto the major axis, which causes further uncertainties in the measurement of the rotation curves. And last but not least, we might make errors in the calculation of the rotation curves not only from the long-slit spectra but also from the FP data because part of the H α emission could be absorbed by dust.

The resulting rotation curves are now described and discussed separately for all four galaxies.

NGC 2366

A comparison of both rotation curves (see Fig. 7.1 upper left panel) shows that from a radius of 1 kpc on, the H α rotation curve lies below the H I curve. Several factors could be responsible for this difference: first of all, the H α distribution is usually very patchy so that the fitting of a tilted-ring model to the velocity field leads to a low the filling factor of the rings, which then leads to higher errors in the velocity calculation. Additionally, the ionised gas is dominated by outflows as, e.g., the huge outflow north-west of the Giant Extragalactic H II Region (GEHR) in NGC 2366. The FP H α velocity map used for deriving the rotation curve always shows the component of highest intensity and not the intensity weighted mean, which is at the position of the huge outflow the outflow itself and not a gas component that follows the rotation of the galaxy. In fact, the only component detected in this area is the huge outflow of ionised gas. This means for the tilted-ring fitting that sometimes, a high fraction of points along the rings (especially close to the centre where the rings are small) has a completely different velocity as expected from the rotational gradient, which results in an over- or underestimation of the actual rotation velocity. However, an over- or underestimation of outflowing gas can here be ruled out as the H α velocity field was first cleaned from blue- or red-shifted gas (see white gaps in Fig. 7.1 upper right panel). This brings us back to the low filling factor of the rings. The centre of the H I lies to the very east of the optical galaxy at $07^{\text{h}}28^{\text{m}}55^{\text{s}}$, $+69^{\circ}12'28''$. From a radius of 1 kpc on, we mainly collect emission from the western H II region and noise. This is why the receding side, indicated by the upper error bars, significantly differs from the combined values as almost no red-shifted emission can be detected beyond a radius of 1 kpc. Therefore, the combined values are dominated by the values from the approaching side.

Additionally, an ellipse fitting of the *R*-band image gives a slightly higher inclination angle of 68° instead of 64° and a much lower position angle of 28° instead of 45° (see Table 4.2). For the $H\alpha$ image we get an inclination of 71° and again a position angle of 28° . This means that the orientation of the optical galaxy is different in comparison to the H I distribution and the optical galaxy seems to be higher inclined than the H I. This was also observed by Hunter et al. (2001) who measured these parameters by drawing several isophotes onto a *V*-band image. If we now apply the H I parameters to the calculation of the $H\alpha$ rotation curve, this might lead to errors.

Because of the problems described above and as the H I rotation curve with a spatial resolution of $13'' \times 12''$ is accurate enough for our kind of study, we would decrease the quality of our analysis by taking the $H\alpha$ velocities for the inner part of the rotation curve. Therefore, we fit the mass models to the H I rotation curve only.

NGC 4861

Figure 7.1 lower left panel shows the rotation curves of NGC 4861. In this case, the H I centre is in very good agreement with the optical centre, which leads to two very similar rotation curves. The error bars of the $H\alpha$ velocities are sometimes quite high (up to 40 km s^{-1}), which is again an effect of outflowing gas structures, although we tried to remove significant red- or blue-shifted emission from the $H\alpha$ velocity field (see Fig. 7.1 lower right panel). The velocity gradient of the $H\alpha$ rotation curve might be a bit steeper, but this could also be caused by the high velocities of the receding side.

As both rotation curves agree very well, we replace the H I velocities in the inner 4.7 kpc by the $H\alpha$ velocities. The velocities can best be fitted by a polynomial function of $v_{rot} = -2.1895 r^2 + 19.126 r$ with v_{rot} in km s^{-1} and r in kpc. This increases the spatial resolution by a factor of 8 in the inner 4.7 kpc and should therefore improve the quality of the models.

IC 4662

For IC 4662, we had to estimate the $H\alpha$ rotation curve from three long-slit spectra. As slit 1 is almost perpendicular to the major axis and slit 3 shows mainly blue- or red-shifted emission, we were left with slit 2, which shows a major fraction of gas that follows the H I rotation (see Fig. 6.11) and whose position angle is close to the H I position angle. The slit was then deprojected onto the major axis and the velocities corrected for the inclination of the neutral gas distribution. Figure 7.2 left panel shows the resulting $H\alpha$ rotation curve indicated by dark grey symbols together with the H I curve marked by black symbols. The $H\alpha$ velocities could best be fitted by a polynomial function of $v_{rot} = -7.1872 r^2 + 51.326 r$, which leads to a steeper rotation curve in the inner 1.2 kpc. In comparison to the H I rotation curves of the other three galaxies of our sample, the H I rotation curve of IC 4662 rises very slowly in the inner part. This is most probably due to the disturbed H I velocity field (see Fig. 6.8) and the low resolution of the H I data (beam smearing). Adding the $H\alpha$ velocities significantly improved the quality of the H I rotation curve. The dynamical centre is located at $17^{\text{h}}47^{\text{m}}09^{\text{s}}, -64^\circ 39' 00''$, which means that the $H\alpha$ emission is mainly located on the approaching side. Therefore, no error bars indicating receding and approaching side could be drawn.

NGC 5408

Concerning its morphology, the optical part of NGC 5408 is perpendicular to the H I distribution. The H I centre is located in the north at $14^{\text{h}}03^{\text{m}}20^{\text{s}}, -41^\circ 22' 14''$, which means that the $H\alpha$ has again only an approaching side. The spectra mainly show expanding gas structures (see Fig. 6.12), which

made it difficult to extract the velocities following the H I rotation. The position angle of slit 3 is almost identical to the H I position angle so that we took the velocities along slit 3 without any spatial correction. Additionally, we deprojected slit 1b onto slit 3. Both slits together cover the inner 2 kpc of NGC 5408, which is shown in Fig. 7.3 left panel. The H α velocities are corrected for the inclination of the neutral gas. Values from slit 3 are marked in dark grey, values from slit 1b in light grey. Only data points close to the H I values are plotted in this diagram. Again, no error bars indicating receding and approaching side could be drawn as we only measure the approaching side of NGC 5408. In general, the H α velocities follow the H I rotation curve very well. The H α gradient can best be described by a linear function of $v_{rot} = 10.864 r$.

7.4 Mass models

We have improved the quality of the H I rotation curves of our sample galaxies (except for NGC 2366) by adding high-resolution H α data to the inner kpcs. These rotation curves are now used to perform a mass decomposition with the GIPSY task *rotmas*, which allows to interactively fit the single components (halo, gas, stars) to the observed rotation curve by minimising the χ^2 of the parameter space. In this section, the derivation of the single mass components is described and the used dark matter halo models are introduced.

7.4.1 Dynamical components

As dwarf galaxies are dark matter-dominated, the velocity contribution from the baryons is often neglected when fitting dark matter halo models to the rotation curves of these galaxies. This type of fit which ignores the contribution of stars and gas is called the minimum-disk case. But although the dark matter is the dominant component in dwarf galaxies, the baryons are still important, especially close to the centre. In order to accurately determine the distribution of the dark matter, the contribution of stars and gas to the observed rotation curve has also to be considered. The velocity component of the gas is determined by using the H I density profiles. In order to account for He and metals a scaling factor of 1.5 is included. Flux-calibrated optical or infrared images together with a stellar mass to light (M/L) ratio give the contribution of the stars. Taking into account all three components is called the maximum-disk case. The observed, total velocity is then given by

$$v_{\text{obs}}^2 = v_{\text{stars}}^2 + v_{\text{gas}}^2 + v_{\text{halo}}^2 \quad (7.1)$$

7.4.2 Dark matter halo models

We use two models to describe the dark matter halo, which are the cuspy NFW halo (e.g., Navarro et al. 1996) and the cored pseudo-isothermal (ISO) halo (e.g., Binney & Tremaine 1987).

Numerical simulations show that the density of CDM haloes rises steeply towards the halo centre (e.g., Navarro et al. 1996). The NFW mass-density distribution is described as

$$\rho_{\text{NFW}}(r) = \frac{\rho_i}{r/r_s \cdot (1 + r/r_s)^2} \quad (7.2)$$

where ρ_i is related to the density of the Universe at the time of halo collapse, and r_s is the characteristic radius of the halo. This leads to a rotation curve

$$v_{\text{rot}}(r) = v_{200} \sqrt{\frac{\ln(1 + cx) - (cx)/(1 + cx)}{x[\ln(1 + c) - c/(1 + c)]}} \quad (7.3)$$

with $x = r/r_{200}$. The concentration parameter $c = r_{200}/r_s$ is directly correlated to v_{200} , the circular velocity at r_{200} (de Blok et al. 2003)

$$\log c = 1.191 - 0.064 \log v_{200} - 0.032 \log v_{200}^2 \quad (7.4)$$

r_{200} is the radius at which the density contrast exceeds 200, roughly the virial radius (Navarro et al. 1996).

As observations have shown that dwarf and low surface brightness galaxies cannot well be fitted by a cuspy halo, the empirically derived ISO halo is used. It describes a dark matter halo that has a core of roughly constant density. The density profile is given by

$$\rho_{\text{ISO}}(r) = \rho_0 \left(1 + \left(\frac{r}{r_c} \right)^2 \right)^{-1} \quad (7.5)$$

with ρ_0 being the central density and r_c the core radius. The rotation curve corresponding to this density profile is

$$v_{\text{rot}}(r) = \sqrt{4\pi G \rho_0 r_c^2 \left(1 + \frac{r_c}{r} \arctan \left(\frac{r}{r_c} \right) \right)} \quad (7.6)$$

7.4.3 Fitting process

Three different scenarios are presented here, a minimum-disk fit, a minimum-disk + gas fit, and a maximum-disk fit.

Minimum-disk

The NFW and ISO haloes are fitted to the observed rotation curve. As the contribution of stars and gas are ignored, this case puts an upper limit on the slope and the concentration of the halo density profile.

Minimum-disk + gas

The gas also contributes to the observed rotation curve. Next to H I, which dominates the gas component, He and the metals are included by scaling the H I data by a factor of 1.5. As the ratio between the molecular gas and H I is much lower in dwarf galaxies in comparison to luminous spirals (Taylor et al. 1998; Leroy et al. 2005), we did not correct for this gas component. In order to create a surface density profile for the H I, the GIPSY task *ellint* was taken, using the H I intensity map and the parameters from the best tilted-ring model as an input. The output of *ellint* is given in terms of mean flux and has therefore to be converted to physical units. The GIPSY task *rotmod* then allows to determine the rotation of the gas under the assumption of an infinitesimally thin disk.

Maximum-disk

The derivation of the rotation curve of the stellar disk is the most critical part as the surface photometry depends on different factors which are difficult to estimate like the extinction or the M/L ratio. We used results from surface photometry performed by Hunter et al. (2001) for NGC 2366, by Gil de Paz & Madore (2005) for NGC 4861, by Hunter & Elmegreen (2006) for IC 4662, and by Noeske et al.

TABLE 7.2: Parameters for the exponential disk fitting.

	NGC 2366	NGC 4861	IC 4662	NGC 5408
Band	<i>V</i>	<i>R</i>	<i>V</i>	<i>J</i>
μ_0 [mag/arcsec ²]	22.82	20.95	19.49	18.29
<i>h</i> [kpc]	1.59	0.88	0.3	0.33
References	(1)	(2)	(3)	(4)
<i>M/L</i>	1	0.3	0.2	-
M_\odot [mag]	4.83 (<i>V</i>)	4.42 (<i>R</i>)	4.83 (<i>V</i>)	3.64 (<i>J</i>)

References: (1) Hunter et al. (2001), (2) Gil de Paz & Madore (2005), (3) Hunter & Elmegreen (2006), (4) Noeske et al. (2003)

(2003) for NGC 5408. For all galaxies, the surface density can be described by an exponential disk model

$$\mu = \mu_0 + 1.086 \frac{r}{h} \quad (7.7)$$

with μ_0 being the central surface brightness and *h* the disk scale length. The parameters for each galaxy are given in Table 7.2. They were then converted from [mag/arcsec²] to units of L_\odot/pc^2 . As the absolute magnitudes are just the magnitudes measured at a distance of 10 pc, we could determine how many arcsec² would fit into an area of 1 pc² at a distance of 10 pc. Using the absolute magnitude of the sun M_\odot in the appropriate filter (see Table 7.2), we may say that L_\odot/pc^2 equals the absolute solar magnitude per 1 pc² area at a distance of 10 pc. This gives a conversion factor of

$$conv = \frac{M_\odot[\text{mag}]}{-2.5 \log(\tan(1/10))^2 [\text{arcsec}^2]} = M_\odot + 21.5649 \quad (7.8)$$

The desired surface brightness values in terms of luminosities could then be calculated with

$$\Sigma = 10^{-0.4(\mu - conv)} \quad (7.9)$$

Again, we used *rotmod* to determine the rotation of the stars under the assumption of an infinitesimally thin disk. Note that we made the simplifying assumption of a stellar *M/L* of 1 in the case of NGC 2366, which is in good agreement with adopting a Kroupa or a Kennicutt initial mass function (IMF) (Portinari et al. 2004). For the other three galaxies, calculations by assuming a Kroupa or Kennicutt IMF revealed a stellar *M/L* below 1, but above 0.6. However, adopting a stellar *M/L* of 0.6 already led in all three galaxies to a stellar rotation curve that lay above the observed curve in the inner kpc. Therefore, we chose a *M/L* of 0.3 for NGC 4861 and 0.2 for IC 4662, which are still physical values (see also Spano et al. 2008). In case of NGC 5408, we did not fit a stellar component as the *M/L* value had to be far below 0.1 in order to fit the observed rotation curve.

Figures 7.4, 7.5, 7.6 and 7.7 show the results for the four sample galaxies. For both dark matter halo models, the full rotation curve is plotted and modelled as well as only the inner rising part. As described in App. C, the outer parts show a large scatter due to the lower filling factor of the tilted rings. From top to bottom the minimum-disk, the minimum-disk + gas and the maximum-disk cases are fitted. Grey symbols represent the observed rotation curve, the long-dashed lines present the halo

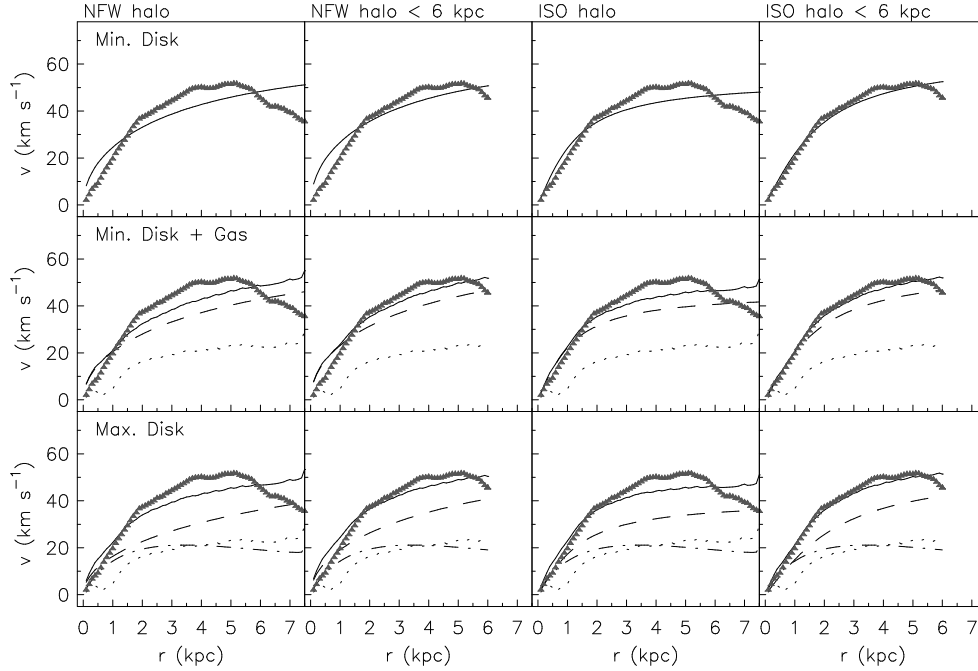


FIG. 7.4: Mass decomposition of NGC 2366. The rotation curves for an NFW halo (full rotation curve and < 6 kpc) and an pseudo-isothermal halo are modelled. From top to bottom the minimum-disk, the minimum-disk + gas, and the maximum-disk cases are fitted. Grey symbols represent the observed rotation curve, the long-dashed lines the halo component, the dotted lines the gas component, the dashed-dotted lines the contribution of the stars, and the solid lines the resulting model fit.

component, the dotted lines the gas component, and the dashed-dotted lines the contribution of the stars. The resulting model fit is indicated by a solid line.

Table 7.3 lists the results of the best fits for both profiles including the reduced χ^2 . We assumed v_{200} to be the rotation speed, which we estimated from the observed rotation curve. Following Eq. 7.4, we derived the concentration parameter c . We kept both parameters fixed so that the only free parameter is r_{200} . In the case of the ISO halo both parameters were kept free.

7.5 Discussion

All fits show that in general, the ISO halo gives much better solutions than the NFW halo, which agrees with other analyses (see, e.g., Kuzio de Naray et al. 2008; Spano et al. 2008). All fits could further be improved by adding the gas and the stellar component. In the following subsections each galaxy is analysed separately.

7.5.1 NGC 2366

Figure 7.4 shows the resulting fits for NGC 2366. A comparison of the reduced χ^2 values immediately reveals that the ISO halo gives much better results than the NFW halo independent of the radius of the rotation curve. As the HI rotation curve strongly declines from a radius of 6 kpc on, we also modelled the curves without the outer 1.5 kpc. This gives improved fits for both haloes. Additionally, χ^2 becomes lower by going from the minimum-disk to the maximum-disk case, which means that the baryons play an important role, at least in the core region of a galaxy.

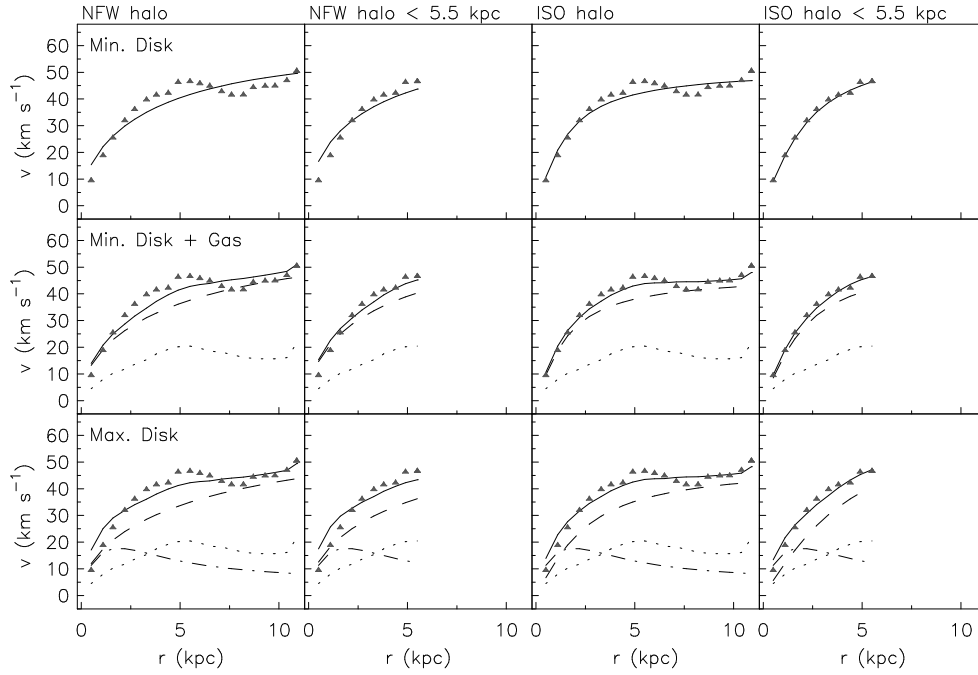


FIG. 7.5: Mass decomposition of NGC 4861. In the inner 4.7 kpc, the H I velocities are replaced by a polynomial function fitted to the H α velocities of $v_{rot} = -2.1895 r^2 + 19.126 r$ with v_{rot} in km s^{-1} and r in kpc. Otherwise the same as in Fig. 7.4. A reduced rotation curve was fitted up to a radius of 5.5 kpc.

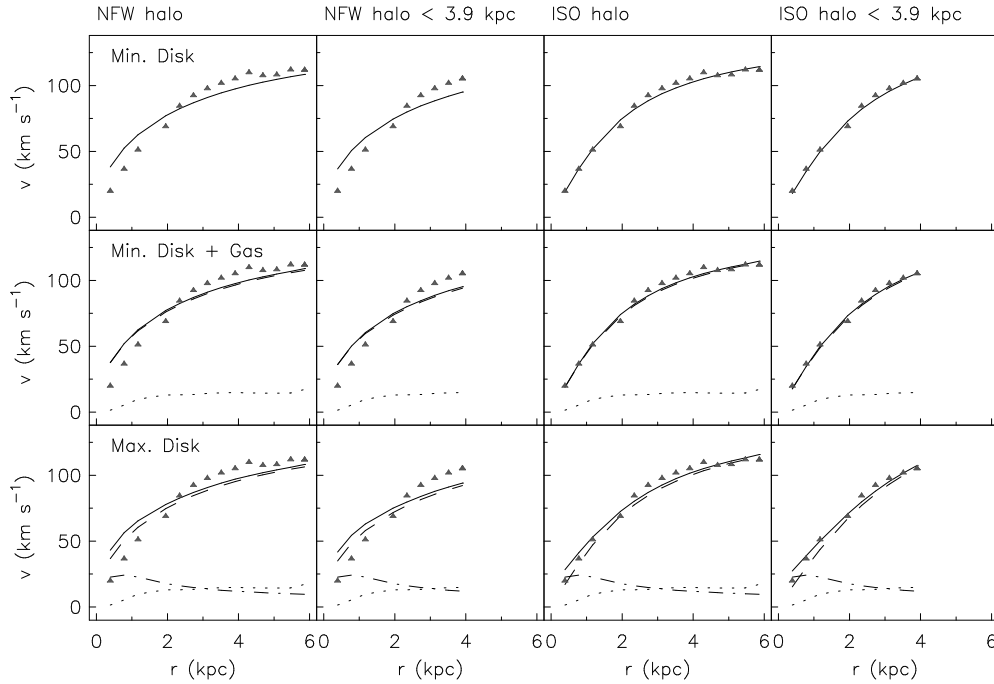


FIG. 7.6: Mass decomposition of IC 4662. The same as in Fig. 7.5. The H α velocities replace the H I velocities in the inner 1.2 kpc and are represented by a polynomial function of $v_{rot} = -7.1872 r^2 + 51.326 r$. A reduced rotation curve was fitted up to a radius of 3.9 kpc.

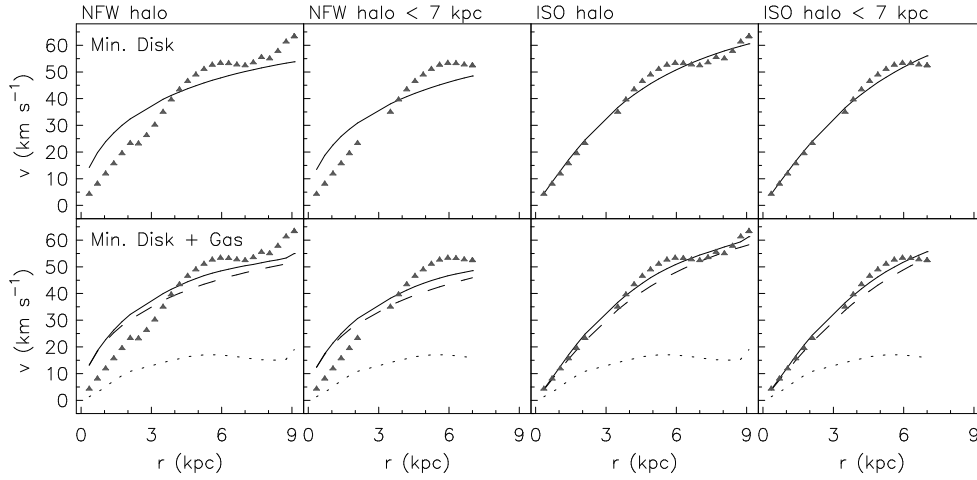


FIG. 7.7: Mass decomposition of NGC 5408. The $H\alpha$ velocities replace the $H\text{I}$ velocities in the inner 2.1 kpc and are represented by a linear function of $v_{rot} = 10.864 r$. The contribution of the stars could not be fitted. A reduced rotation curve was fitted up to a radius of 7 kpc.

Alltogether, the reduced $H\text{I}$ rotation curve fitted with an ISO halo gives the lowest values for χ^2 . The resulting model fit agrees very well with the $H\text{I}$ curve in the inner 3 kpc and also in the outer parts the ISO halo gives better results than the NFW halo. Moreover, the values of the core densities and radii from the ISO models are very reasonable.

7.5.2 NGC 4861

We had to choose a stellar M/L of 0.3 for NGC 4861, which is a factor of 2 to 3 lower than the one we calculated by adopting a Kroupa or a Kennicutt IMF (see Sect. 7.4.3). However, only this low value provided us with a stellar rotation curve that lay below the observed rotation curve. As already mentioned in Sect. 7.4.3, the derivation of the stellar component is the most crucial part of the mass decomposition due to the surface photometry which depends on different, hard assessable factors. This means that the surface photometry might be wrong. Another possibility is that the observed rotation curve is not exact. However, we measured the rotation curve from two different data sets and in two different wavelengths, and they both agree very well, which is a good check against an incorrect rotation curve. The reduced χ^2 values of the maximum-disk case show that we did indeed not fit a very good model as the χ^2 values are partly the highest for the maximum-disk case in comparison to the other two cases. In NGC 2366, they always decrease from the minimum- to the maximum-disk case, which is what we would expect by adding the gas and the stars.

Without further considering this problem, we can nevertheless say that NGC 4861 shows the best resulting fits and lowest χ^2 values of all four galaxies (see Fig. 7.5 and Table 7.3). As already mentioned in Chap. 5 and Sect. 7.3.2, both the morphology and the kinematics of the neutral and ionised gas agree very well with each other. The galaxy is very symmetric and undisturbed except for the outer eastern part. Nevertheless, the trend is the same as in NGC 2366: the ISO halo gives much better results than the NFW halo and the fits could significantly be improved by removing the outer rising part of the rotation curve and by concentrating on the inner 5.5 kpc. By taking the $H\alpha$ rotation curve for the inner 4.7 kpc, the χ^2 values could significantly be lowered to 60% of the old value in case of the full rotation curve and a NFW halo, to 30% of the old value in case of a reduced rotation curve and a NFW halo, to 50% in case of the full rotation curve and an ISO halo, and to below 30% in case of a

reduced rotation curve and an ISO halo. The improvement of the resulting fits for the reduced rotation curves is of course much larger as almost 90% of these curves consist of $H\alpha$ velocities. Altogether, the ISO halo gives an excellent model for the inner 5.5 kpc.

7.5.3 IC 4662

Concerning the stellar M/L value, we had the same problems for IC 4662 as for NGC 4861. Additionally, IC 4662 was very difficult to handle due to its disturbed HI velocity field which led to huge problems in deriving a rotation curve. The low resolution of the ATCA data and therefore the problem of beam smearing together with the distortions in the inner part of the galaxy were two good reasons to use the $H\alpha$ rotation curve. But as only one slit spectrum was available, the so-derived rotation curve is only an approximate representation of the true rotation curve. Because of all these reasons, the reduced χ^2 values are almost always the highest in this galaxy in comparison to the other three galaxies.

7.5.4 NGC 5408

NGC 5408 is similar to NGC 4861, a quiet galaxy without any large scale distortions which severely influence its kinematic behaviour. We used the $H\alpha$ rotation curve for the inner 2.1 kpc, which is in good agreement with the velocity values of the HI curve. In comparison to the other three galaxies, both curves, HI and $H\alpha$, rise very slowly in the inner 2 kpc. Using the photometric data from the literature, it was impossible to derive a stellar rotation curve that lay below the total rotation curve, also not by assuming a stellar M/L ratio of 0.1, which is the lowest value before becoming unphysical. Again, we either underestimate the rotation in the inner part (remember that we estimated the $H\alpha$ curve from only two long-slit spectra) or the photometric data are not accurate enough. We therefore decided to not model the stellar component.

Figure 7.7 shows the resulting fits. Again, the χ^2 values are very high for the NFW halo and much smaller for the ISO halo. For this galaxy, the reduced rotation curve did not significantly improve the quality of the models, which is probably due to the fact that the repeated rising of the rotation curve beyond a radius of 7 kpc fits the first rise of the curve.

7.6 Summary

We used VLA and ATCA HI data of a sample of four nearby irregular dwarf galaxies in order to perform a mass decomposition of the derived rotation curves. In all galaxies except for NGC 2366, we replaced the inner parts of the HI rotation curves by $H\alpha$ velocities derived from FP data (NGC 4861) or long-slit spectra (IC 4662 and NGC 5408). We fitted a cuspy NFW halo and a cored pseudo-isothermal halo to the rotation curves and modelled the minimum-disk, the minimum-disk + gas, and the maximum-disk cases. The resulting model fits show that in all four galaxies, the observed rotation curves are better represented by the ISO halo, which is contradiction with CDM simulations (e.g., Navarro et al. 1996; Moore et al. 1998), but in good agreement with other observations (e.g., Kuzio de Naray et al. 2008; Spano et al. 2008).

We could significantly improve the quality of the NFW and ISO halo fits by restricting the radius to the rising part and neglecting the flat and sometimes even the declining part. The reduced χ^2 could also be lowered for both halo models by considering the gas and the stars. This means that the baryons cannot be neglected, at least not in the inner part of the galaxies.

TABLE 7.3: The basic parameters of the mass decomposition.

Parameter Unit	NFW full				NFW small				ISO full			ISO small		
	v_{200} [km s ⁻¹]	c	r_{200} [kpc]	χ^2	v_{200} [km s ⁻¹]	c	r_{200} [kpc]	χ^2	ρ_0 [10 ⁻³ M _⊙ pc ⁻³]	r_c [kpc]	χ^2	ρ_0 [10 ⁻³ M _⊙ pc ⁻³]	r_c [kpc]	χ^2
NGC 2366														
Min.-disk	50	9.4	114.42	46.32	50	9.4	95.08	21.96	48.59	1.05	28.38	32.93	1.52	4.92
Min.-disk + gas	50	9.4	170.23	46.05	50	9.4	130.26	13.53	43.80	0.95	27.92	28.15	1.45	3.82
Max.-disk	50	9.4	274.39	36.06	50	9.4	196.59	12.56	23.58	1.14	24.38	14.17	1.98	4.18
NGC 4861														
Min.-disk	46	9.5	133.89	14.51	46	9.5	113.84	13.91	27.40	1.34	6.51	19.34	1.89	0.56
Min.-disk + gas	46	9.5	182.83	10.62	46	9.5	148.41	8.49	22.03	1.37	3.72	16.83	1.80	0.88
Max.-disk	46	9.5	224.46	11.73	46	9.5	202.89	19.97	10.21	2.10	6.26	7.02	3.43	5.34
IC 4662														
Min.-disk	107	8.5	77.88	89.12	107	8.5	84.67	122.73	138.89	1.65	9.40	119.85	1.96	5.34
Min.-disk + gas	107	8.5	80.54	85.16	107	8.5	87.47	117.47	134.28	1.67	9.62	115.51	1.99	5.73
Max.-disk	107	8.5	84.39	127.10	107	8.5	93.45	178.94	107.85	1.95	23.10	84.99	2.70	18.17
NGC 5408														
Min.-disk	53	9.7	152.58	50.20	53	9.7	170.97	54.80	8.77	3.93	4.73	8.22	4.38	4.00
Min.-disk + gas	53	9.7	179.12	42.85	53	9.7	203.67	45.73	7.02	4.41	3.90	6.62	4.92	3.59

Summary and Outlook

8.1 Summary

In order to explain the enrichment of the intergalactic medium, it is important to understand outflow processes, to know what the drivers for an outflow are and what the fate of the outflowing gas is. Massive stars transfer kinetic energy and momentum into the interstellar medium through stellar winds and supernovae explosions, which leads to an expanding superbubble filled with hot gas and defined by cool dense gas shells in the outer parts. If the energy input is high enough, the shells can fragment and the hot gas is blown out from the disk into the halo of the galaxy (*chimney* model, Norman & Ikeuchi 1989). At this point, two developments are possible: either the hot gas cools down and eventually falls back onto the galactic disk or the gas is blown away and becomes a galactic wind, enriching the IGM with metals. The probability of a galactic wind is strongly increased in low mass galaxies where the gravitational potential is low (Mac Low & Ferrara 1999). Therefore, dwarf galaxies are best suited for this kind of study as they are sources of strong star formation (which means that the energy input is high), but generally have a low gravitational potential.

A sample of four nearby irregular dwarf galaxies was studied in this thesis (NGC 2366 in Chaps. 3 and 4, NGC 4861 in Chap. 5, IC 4662 and NGC 5408 in Chap. 6). Deep $H\alpha$ images of all four galaxies reveal numerous filaments up to kpc-size in and around the galactic plane, but also at kpc-distance away from star-forming regions. Therefore, the $H\alpha$ kinematics were studied by performing Fabry-Perot interferometry (NGC 2366 and NGC 4861) and medium-resolution long-slit spectroscopy (IC 4662 and NGC 5408). The optical data were complemented by H I synthesis observations from the VLA (NGC 2366 and NGC 4861) and the ATCA (IC 4662 and NGC 5408) and partly by 20 cm radio continuum observations from the ATCA (IC 4662 and NGC 5408). The morphology and especially the kinematics of both gas components were examined and compared with each other.

All four galaxies harbour small- and large-scale filaments and shells visible on our deep $H\alpha$ images. Especially NGC 4861 shows huge shells of kpc-size at a distance of several kpcs from the galactic disk. They are connected to the disk by long, narrow filaments, which indeed give the impression of material transported into the halo through chimneys. The kinematic analysis of the sample galaxies usually revealed outflowing ionised and most of the times also neutral gas at the positions of these filaments and shells. The lowest expansion velocities were measured in NGC 4861 (about 25 km s^{-1}), the highest in IC 4662 (up to 75 km s^{-1}). This is not surprising because NGC 4861 shows a fairly symmetric H I distribution as well as a regular H I velocity field, except for the distortion in the east due to the H I cloud. IC 4662, however, is far away from being symmetric or regular so that

turbulence and high velocity outflows are expected. In the following subsections, the main results for all galaxies are briefly summarised.

8.1.1 Outflows of neutral and ionised gas in dwarf galaxies

The regions of high H I velocity dispersion in NGC 4861 coincide well with the main outflows detected on the H α velocity field. A Gaussian decomposition of the H I line reveals that the outflows are also detectable in H I with the same expansion velocities, but extending over a larger area.

In NGC 2366, an outflow was detected with no counterpart in H I and an expansion velocity of 50 km s^{-1} that expands into an area of low H I column density indicating that the neutral gas is already fully ionised. Comparing NGC 2366 with NGC 4861, we saw that both galaxies are very similar concerning its optical morphology, its luminosity and its mass, and its H I properties like inclination and rotation velocity. Therefore, the results regarding the outflows lead to two possible conclusions: either the star formation in NGC 2366 is stronger and the gas was faster ionised than in NGC 4861 or the star clusters in NGC 2366 are older which means that the ionisation has lasted for a longer time than in NGC 4861. The suggestion that NGC 2366 has a higher kinetic luminosity is supported by the detection that NGC 2366 shows at several wavelengths (optical, radio, UV) evidence for two weak spiral arms emanating from the bar-like disk (see Chap. 3), which leads to a more disturbed medium and to triggered star formation. A second outflow was detected in NGC 2366 with $v_{\text{exp}} = 30 \text{ km s}^{-1}$ both in H α and H I.

In comparison to the other three galaxies, NGC 5408 only shows few small-scale ionised gas structures on the H α image. The H I intensity distribution is very symmetric, although on larger scales perpendicular to the stellar disk. The H I velocity field is fairly regular. Nevertheless, outflowing gas was detected all over the stellar disk with expansion velocities up to 60 km s^{-1} indicating strong star formation activity. One outflow was found in H I, but not in H α with an expansion velocity of 60 km s^{-1} , which is several kpc away from the dynamical centre of the galaxy.

Similar to NGC 5408, IC 4662 shows two systems with two different alignments in H I, one of them coinciding with the stellar disk, the other larger one embedding the first one and perpendicular to it. The H I velocity field is very disturbed and also seems to change its alignment by 90° in the centre of the H I distribution. Most of the outflows were detected in H α and H I, but the galaxy also shows one outflow only in H I, at a distance of 1.5 kpc from the dynamical centre. An often discussed peculiarity in this galaxy is the southern H II region, which has a different oxygen abundance than the northern H II region complex leading to the assumption that it is an own system (Hidalgo-Gómez et al. 2001). The observations show no distinctive features concerning its kinematics. Instead, the spectra reveal the same kinematic behaviour of the gas as in the main H II region complex. Outflowing gas was found with an expansion velocity of 40 km s^{-1} blue- and red-shifted (in H I only the blue-shifted component is visible). Additionally, the H II region is connected through diffuse filamentary ionised gas and smaller H II regions to the main optical part. It is embedded into the neutral gas and the 20 cm radio continuum. Altogether, this leads to the assumption that the southern H II region is a part of IC 4662.

Having found many outflowing gas structures in the sample galaxies with supersonic expansion velocities, the question rises what their fate is. Therefore, the escape velocities of the galaxies were calculated by taking the pseudo-isothermal halo model that well describes the observed rotation curves in the inner parts of dwarf galaxies (see below). In all cases, the expansion velocities of the outflows are only 30% to 50% of the escape velocities, derived under the assumption that the radius of the dark matter halo r_{max} equals to the H I radius. However, r_{max} is most probably much higher, which leads to even higher escape velocities further decreasing the probability of a galactic wind. At first

glance, this looks like a contradiction with theoretical models like, e.g., the superbubble model by Mac Low & Ferrara (1999). But note that outflowing gas was only detected close to the dynamical centre where the escape velocities are very high. Few kpcs away from the dynamical centre, the escape velocity drops significantly, increasing the probability of a galactic wind. This can, e.g., be seen in NGC 5408, which harbours an outflow in H I, 4.3 kpc away from the dynamical centre with an expansion velocity of 60 km s^{-1} . In this case, the expansion velocity is still below the escape velocity, but it only differs by 20 km s^{-1} , which corresponds to a factor of $v_{\text{exp}}/v_{\text{esc}} = 0.8$. Possibly, there are even more outflows at larger distances from the dynamical centre, but their column densities will be strongly decreased and therefore, the data used in this thesis are most probably not sensitive enough to detect this gas. On the other hand, assuming that the current star formation episode is the driver of the outflows and taking into account the simulations by Mac Low & Ferrara (1999), it becomes clear that all four galaxies, having dynamical masses of roughly $(4-16) \times 10^9 M_{\odot}$, are still at the beginning of the superbubble blowout process. As Fig. 1.2 shows, at total masses of $10^9 M_{\odot}$, most of the gas is still bound to the disk when the energy input stops. However, the star clusters in, e.g., NGC 2366 are only a few Myrs old (Drissen et al. 2001), which makes a superbubble blowout even more unlikely. The huge shells in NGC 4861 are therefore most probably the result of a former star formation event as they are located at several kpcs away from any place of current star formation activity.

Alltogether, this means that our observations are in good agreement with the simulations. All sample galaxies harbour filaments and shells that could be shown to expand, but the galaxy masses are too high and the galaxies not old enough to have experienced a significant mass loss.

8.1.2 The cusp-core discrepancy

As we needed to decide for a halo model in order to derive the escape velocities, a mass decomposition of the sample galaxies was performed. The H I rotation curves were complemented in the inner parts by H α velocities in order to improve the spatial resolution. The NFW halo and the pseudo-isothermal halo were used to model the derived rotation curves (see Chap. 7). The fits improved from the NFW to the ISO halo and from the minimum-disk to the maximum-disk case. This means that in contradiction to dark matter halo simulations (e.g., Navarro et al. 1996; Moore et al. 1998, 1999) and in agreement with many other observations (e.g., de Blok & Bosma 2002; Kuzio de Naray et al. 2008; Spano et al. 2008), the cored ISO halo describes the rotation curve of a dwarf galaxy much better than the NFW halo in the inner few kpcs. Additionally, the baryons cannot be neglected, at least not in the inner parts of the rotation curves.

8.1.3 H I cloud in NGC 4861 – did we find a dark galaxy?

A peculiar feature in NGC 4861 is the small H I cloud to the east, which is interacting with the main body of the galaxy because its rather symmetric H I distribution is extended to the east, the velocity field is disturbed and we found a high velocity dispersion. A 90 min V-band exposure obtained with the Calar Alto 2.2m telescope suggests that this cloud has no optical counterpart as we did not detect any star association down to a 3σ detection limit of 27.84 in V. Additionally, the cloud rotates, although only with 4.4 km s^{-1} , which is that low in comparison to an H I mass of $4 \times 10^6 M_{\odot}$ that it lies far above the Baryonic Tully-Fisher relation. However, the inclination of this object was difficult to measure and could be much lower than the 65° we finally assumed, which would then move the cloud onto the BTF correlation. Despite this uncertainty, the missing stellar component as well as the regular rotation pattern are two strong arguments that lead to the result that an interpretation of this cloud as a dark galaxy cannot be ruled out.

8.2 Outlook

A direct conclusion from the summary is that the study of the fate of the outflows has to be extended to galaxies of lower mass. With a total mass of $(4-16) \times 10^9 M_{\odot}$ the sample galaxies lie at the higher end of the mass range modeled by Mac Low & Ferrara (1999) where the probability of a galactic wind is close to or even is zero.

Furthermore, in this thesis, the main emphasis lies on the kinematics of the neutral and ionised gas. Concerning the detected expanding gas structures, only their fate was analysed, which is a late state in the evolution of these structures. What has to be addressed in future studies are the ionisation or excitation mechanisms, i.e., the history of the ionised gas. How does the neutral gas get its kinetic energy, how is it ionised? And what are the drivers for a superbubble blowout? What is the energy source for all structures found at a distance of several kpcs away from ionising star clusters? For all four galaxies, long-slit spectra are available that cover the whole red wavelength range including the critical diagnostic lines of [OI], [NII] and [SII]. Studies of emission line ratios such as [NII]/H α and [SII]/H α provide information about the physical conditions of the gas. Photoionisation models like CLOUDY can then be used to examine the trends of the observed emission line ratios and therefore, to constrain the ionisation processes (Elwert & Dettmar 2005).

An important aim of this thesis was to perform a multi-wavelengths study. Only in comparison with other components, a component in a galaxy can properly be analysed. Here, the neutral and ionised gas component were compared and partly also the 20 cm radio continuum, at least in the case of IC 4662 and NGC 5408. The radio continuum is a tracer for star formation, and observations at several cm wavelengths would allow to distinguish radio continuum emission from HII regions from radio continuum emission from supernovae (Condon 1992), which means to distinguish younger from older star formation regions. This analysis would make it possible to define a star cluster as an ionising source for an outflow or to rule it out. CO observations as a tracer for the molecular gas as well as X-ray observations could complement this multi-wavelengths study.

Although fibre spectrographs are the more popular instruments at the moment, Fabry-Perot interferometers are still powerful tools to study galaxies in detail. Several observatories scattered over the whole world offer the opportunity to attach a FP to their telescopes. However, only few people know how to handle these data. The GHASP survey (see Chap. 2) is the only survey that includes a larger number of galaxies observed with a FP. One important result of this thesis is that the FP data with their high spatial and spectral resolution are well-suited for a kinematic analysis of the ionised gas component. Therefore, a large survey of nearby gas-rich galaxies, preferable on the southern hemisphere, could help to deepen our knowledge about the ionised gas component. This survey could also be used as a complement to HI surveys like, e.g., LVHIS on the southern hemisphere or THINGS on the northern hemisphere.

Appendix A

The Gaussian decomposition

The velocity maps that are created from 3d data cubes containing two spatial axes and one spectral axis usually show the intensity weighted mean velocity values. This means that the splitting of an emission line into several components can only be detected on the velocity dispersion map with a high velocity dispersion as an indicator. In this thesis, however, we were especially interested in searching for outflowing gas structures, i.e., gas structures whose velocities differ from the main velocity component. Therefore, the spectra in every pixel, especially close to regions of high velocity dispersion, had to be examined in order to detect line-splitting. This was done with the IRAF routine *splot* which allows to interactively fit the emission lines.

As *splot* can only handle 2-dimensional data (intensity vs wavelength / velocity), the spectra had first to be extracted from the 3d H α and H I data cubes. The easiest way to do this was to extract diagonal lines from the cubes. One pixel had to be given as a start point as well as the number of steps which depended on the size of the galaxy and the spatial resolution. The spectrum of every pixel lying on this line was then extracted with the MIRIAD task *gaufit* into an ASCII-file containing intensity and wavelength information. We chose MIRIAD for this step as this software was designed to handle 3d data, whereas IRAF is mainly a 2d imaging and spectroscopy software.

Within IRAF, the ASCII-files needed to be converted into an STSDAS-table format as the IRAF tasks cannot handle ASCII-files. Afterwards, the STSDAS-tables were converted into single spectra. During this process, the header keywords describing the spectral axis were changed from wavelengths to heliocentric velocities.

In order to be within the spatial resolution, the spectra were summed up over roughly one beam size in x and y for the H I data and summed up over 3×3 pixels for the FP H α data. This also had the advantage of improving the signal. The spectra were then loaded into *splot* and the Gaussian decomposition was performed (see Fig. A.1). This task works in the following way: The user chooses the lines he wants to fit (small white vertical dashes in Fig. A.1) and *splot* fits Gaussian, Lorentzian or Voigt profiles to the original spectrum (long dashed line following the observed spectrum indicated by a solid line). The continuum is taken into account and subtracted before the fitting process (short dashed horizontal line). The parameters like peak velocity, integrated flux and Gaussian FWHM for every fit are written into a logfile. After that, the fitted components can be subtracted from the original spectrum in order to look for residuals. In case that a weak component is hidden in a broad component of high intensity, it will become visible after the subtraction of the fitted profile of the strong component. The fitting process is then repeated by forcing *splot* to additionally fit a profile for the weak component.

Following the above described method, the whole galaxy was scanned line after line and the parameters of all profiles were written into the logfile. A new file was created containing the final step of the process, which was putting the newly measured velocity values in the beforehand created empty image file. This file needed to have the same pixel size and numbers of pixels as the cube. The easiest way was to take one of the moment maps developed from the 3d data cube and replace all pixel values by zero. Choosing the desired velocity range, three different velocity maps were created, which are on the one hand the main velocity map that roughly corresponds to the 1st moment map – intensity weighted mean – created by tasks like *moment* in MIRIAD or *moments* in GISPY. On the other hand, two additional velocity maps were built, which contain the blue- and red-shifted components, respectively. As at most places along the galaxy the emission line is not split into several components, empty pixels in the blue- and red-shifted velocity maps were replaced by the value of the main velocity component.

The main script for the Gaussian decomposition (*gaufit_man.cl*, to be run within IRAF) is given here:

– extract spectra –

```

emacs initial          ← give start point in x and y
emacs steps.cl         ← insert number of steps
!rm gaufit.cl
cl < steps.cl          ← create for every step the gaufit command with all pa-
                        rameters set accurately, gives gaufit.cl

emacs gaufit.cl        ← execute gaufit
ls p*_* > profile.lst  ← write all profile-files into list
!perl edittab.pl       ← go to profile_atx_y, take column 2 and 3, store it in pro-
                        file_atx_y.dat

ls p*_*.dat >
profile1.lst
!perl irafcom.pl      ← write cl-script to convert ASCII via STSDAS-table into
                        image

cl < tab2im.cl

```

– combine spectra –

```

emacs initial
emacs steps1.cl        ← number of steps to run scombine
!rm scombine.cl
cl < steps1.cl         ← create cl-script for scombine
emacs scombine.cl
cl < scombine.cl      ← sum spectra over one beam size

```

– run *splot* –

```

ls s*.fits >
splot.dat
!rm splot.cl
!perl splot.pl        ← create cl-script for splot

```

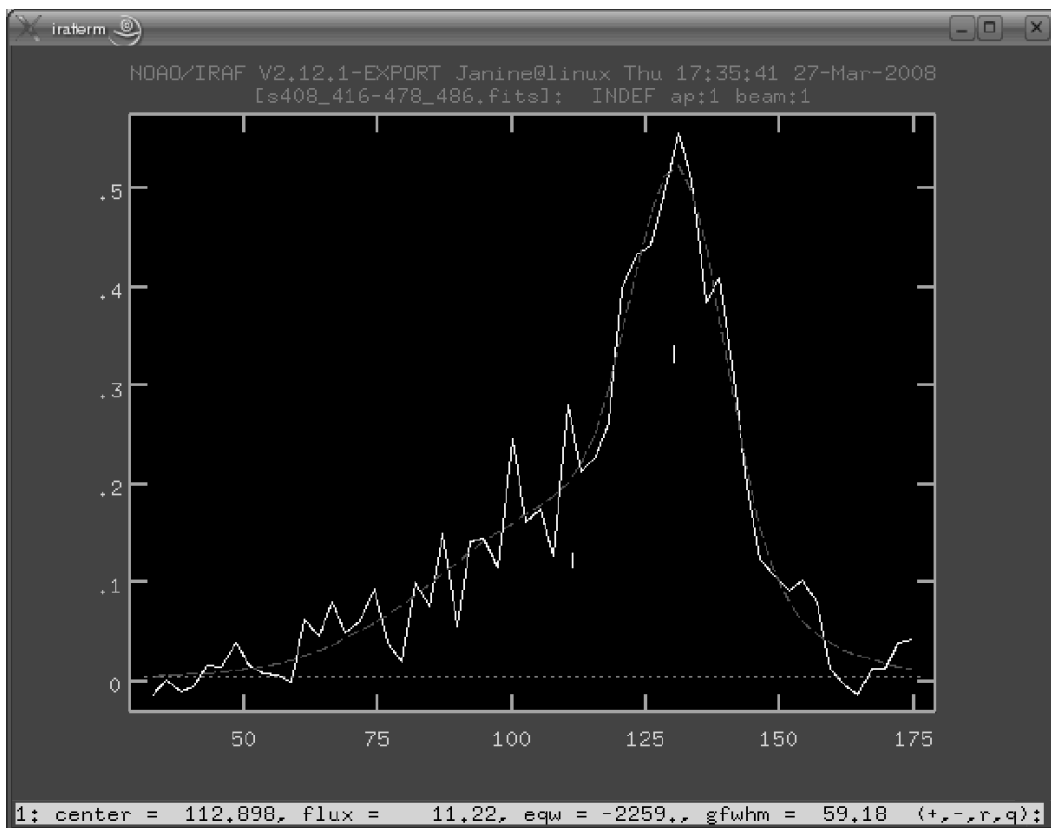


FIG. A.1: The interface of the Gaussian fitting routine *splot*. The user chooses the lines he wants to fit and *splot* gives different parameters of the fitted Gaussian (see lower edge of the interface), among them the peak velocity and the Gaussian FWHM.

```
!rm splot.log
cl < splot.cl           ← run splot
emacs splot.log

                                – create image –

!perl makexyv.pl       ← choose velocity range/ components which shall be plotted

!rm p*_*.dat
!rm p*_*.fits
!rm p*_*.txt
!rm p*_*
!rm s*.fits
!rm *.lst
emacs xyv.cl           ← check cl-script
cl < xyv.cl            ← put the velocity values into the 2d image using the IRAF
                        task imreplace
```


Adaptive filtering

The ionised filaments and shell- or bubble-like structures, which are all an indication for outflowing gas, usually have a very low surface brightness, especially in the outer parts of the optical galaxy. In order to emphasise these structures, an adaptive filter based on the H-transform algorithm (Richter et al. 1991) was applied to the $H\alpha$ images of all sample galaxies. In the following, its necessity and its functionality are explained in more detail.

The low surface brightness gas structures are often barely visible on the $H\alpha$ images. In order to differentiate signal from noise in the regions of low signal, it can be helpful to smooth an image, which is usually done with stationary filters. These filters are space-invariant, which means that they treat every feature in an image alike regardless of whether it is a strong point-like source like a star or a galaxy core, a bright extended object like a galaxy or faint extended emission close to the noise level. This leads to the result that, depending on the filter width, either the strong point-like sources in the image are degraded and smeared or the areas of low signal are not enough smoothed. The solution to this problem is therefore a space-variable filter which smoothes extensively in the background, less extensively in the outer parts of extended objects, and not at all in locations of strong point-like sources. This implies that the filter has to recognise the local resolution and adapt itself to it. It is therefore called adaptive filter. The orthogonal transform which is used for such a filter is called H-transform, which is based on the Haar-transform (Haar 1910). A mathematical description of how this algorithm works is given in Richter (1978).

In simple words, the filter compares the signal-to-noise (S/N) ratio of the objects in a given pixel area with the S/N in neighbouring areas. Bright point-like objects show a strong declining gradient, whereas areas of noise show almost no gradient in comparison to neighbouring areas. In order to make the filter recognise the local gradient, a threshold for the S/N ratio has to be defined. Gradients with absolute values smaller than the threshold are interpreted as noise and set to zero. Otherwise, they are taken as “significant” and stay unchanged. After an inverse transform, the image is smooth over wide regions in the background (all gradients are zero), the stars are unchanged (all gradients significant) and faint emission is smoothed moderately (small-scale gradients zero, large-scale gradients significant).

The adaptive filter is implemented in IRAF under the task *adaptive*. The user can choose the shape of the filter, its width and the S/N threshold. Figure B.1 shows as an example the continuum-subtracted $H\alpha$ image of NGC 2366 before (left panel) and after the adaptive filtering (right panel). A pyramid with a width of 5 and a threshold of 3σ was chosen. The very faint and diffuse emission on

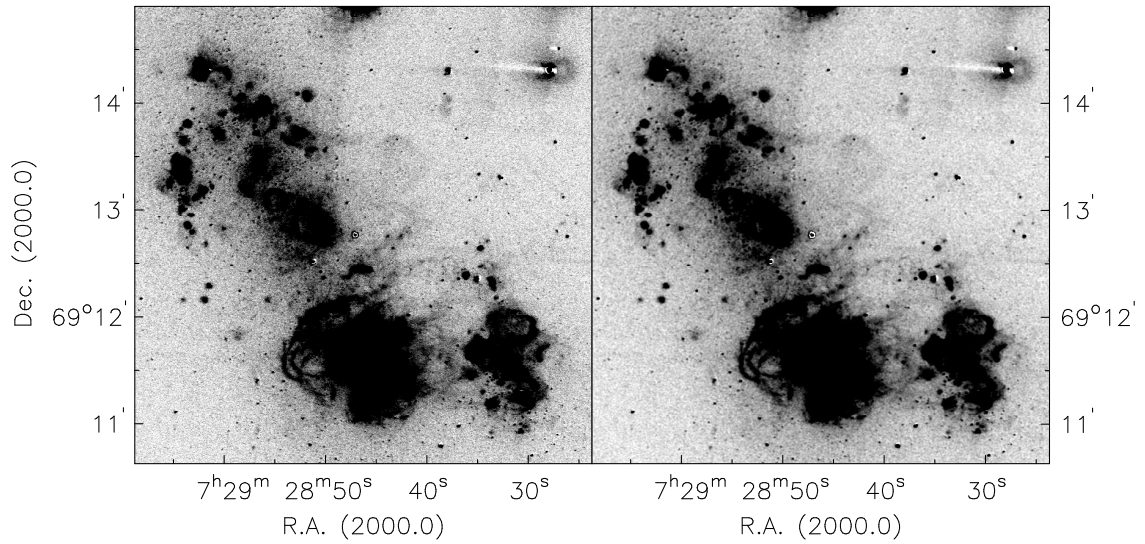


FIG. B.1: The adaptive filter technique in practice. The continuum-subtracted $H\alpha$ image of NGC 2366 is shown before applying the filter (left) and after the performing the H-transform algorithm (right). After applying the adaptive filter technique, the weak filamentary structure on the western side of the galaxy is better visible than before.

the western side of the galaxy is enhanced after the filtering. Small noisy blobs scattered along the disk can now be proved to be faint H II regions.

Deriving the rotation curves

C.1 HI rotation curves

In order to derive rotation curves of the sample galaxies, the moment maps (especially the 1st moment map) had to be extracted from the 3d data. First, the HI cubes were smoothed to distinguish signal from noise (GIPSY task *smooth*). A threshold limit of 2.5σ of the background was set, below which all emission points were transferred as blank pixels (GIPSY task *condit*). The remaining noise was manually removed by going through all channels and only choosing the regions of true emission (GIPSY task *blot*). Finally, the moment maps could be created by using the GIPSY task *moments*.

The rotation curves could then be derived by fitting a tilted-ring model to the velocity field (GIPSY task *rotcur*). In this model, every concentric ring has its own systemic velocity v_{sys} , its centre given by x_0 and y_0 , its inclination i , its position angle PA , its expansion velocity v_{exp} , and its rotation velocity v_{rot} . The *rotcur* routine performs a least squared fit for the function

$$v(x, y) = v_{\text{sys}} + v_{\text{rot}} \cos(\theta) \sin(i) + v_{\text{exp}} \sin(\theta) \sin(i) \quad (\text{C.1})$$

where θ is the azimuthal angle in the plane of the galaxy and is related to the known parameters through

$$\cos(\theta) = \frac{-(x - x_0) \sin(PA) + (y - y_0) \cos(PA)}{r} \quad (\text{C.2})$$

and

$$\sin(\theta) = \frac{-(x - x_0) \cos(PA) + (y - y_0) \sin(PA)}{r \cos(i)} \quad (\text{C.3})$$

The position angle PA is defined as the angle between the north direction on the sky and the major axis of the receding half of the galaxy.

Before running *rotcur*, the GIPSY ellipse fitting task *ellfit* was used to fit an ellipse to the HI velocity field by eye. This routine gave preliminary values for x_0 and y_0 , i , and PA . We took v_{sys} from the global profile plotted with the MIRIAD task *mbspect*, measured v_{rot} to be $(v_{\text{max}} - v_{\text{min}})/2$, and chose v_{exp} to be zero. The width of the rings was defined to be half the beam size and the maximum radius was given by the radius of the ellipse fitted with *ellfit*. With these initial estimates, *rotcur* was able to derive a rotation curve by looking at each ring separately. The side of the velocity field (receding, approaching or both) had also to be specified.

Three different approaches were chosen to derive a rotation curve:

- **Fixed approach:** a rotation curve combining receding and approaching side was fitted by taking the initial estimates and keeping them all fixed.
- **Iterative approach:** in an iterative procedure the best-fitting values were derived. Again, both sides were combined. In a first run, all parameters were kept fixed except for v_{sys} – and, of course, v_{rot} – so that v_{sys} was calculated for each ring. A median of all values was derived afterwards and *rotcur* was started again, this time with the median v_{sys} as a fixed parameter and the centre coordinates kept free. After calculating median values of x_0 and y_0 and giving them to *rotcur* as two fixed parameters, the inclination was kept free which was followed by the position angle as a free parameter. In a last run, the now best-fitting values of all parameters were kept fixed and the final rotation curve was derived. Using the same approach, receding and approaching side were treated separately by taking the already defined values for v_{sys} and the centre coordinates and calculating i and PA . The resulting rotation curves are presented in the diagrams as error bars.
- **Free approach:** the best-fitting values from the iterative approach were taken as initial estimates and all parameters were kept free. The idea of this approach was to prove the reliability of the best-fitting parameters by successfully reproducing the values calculated in the iterative approach for every single ring.

Figures C.1 and C.2 show the values for all parameters of NGC 5408 which are plotted against the radius of the rings. Additionally, the upper right panel displays the filling factor of the rings. The results of the iterative approach (Fig. C.1) show that as long as the filling factor is close to 1, i.e., in this case out to a radius of $300''$, the values of the parameters do not significantly change over the rings, except for the inclination (lower left panel) whose plot indicates two systems, one with an inclination of about 58° and a second one with an inclination of 76° . As a simplifying assumption, only one parameter was calculated for all radii. As already mentioned above, this was done by taking the median of each parameter, indicated by solid lines in Figs. C.1 and C.2. The dashed lines present the 25% and 75% levels. All values above a radius of $300''$ were not considered because of the lower filling factor. Figure C.2 shows the values for the free approach where simultaneously all parameters were kept free during a run of *rotcur*. Here, the scatter is much higher which is due to the increased number of free parameters.

Table C.1 shows the derived values for the different parameters of all three approaches. It can be noted that the initial estimates given by *ellfit* already describe the galaxy very well as they do not significantly differ from the best-fitting values of the iterative approach. The free approach also gives quite reasonable results despite the larger scatter over the rings. The resulting rotation curves for all three approaches are displayed in Figure C.3. The fixed approach is indicated by green symbols, the iterative approach by black symbols plus error bars, and the free approach by red symbols. As already seen in Figs. C.1 and C.2 and in Table C.1, all three approaches agree very well in the inner $300''$ where the filling factor is high.

The above described procedure was also used to derive the HI rotation curves of the other three galaxies.

C.2 $H\alpha$ rotation curves

In order to complement the HI rotation curves in the inner kpcs by higher resolution data, $H\alpha$ rotation curves were derived. In the cases of NGC 2366 and NGC 4861, the procedure was similar to the fixed

TABLE C.1: NGC 5408: Parameter sets for the three different approaches.

Parameters [Unit]	fixed approach	iterative approach	free approach
v_{sys} [km s^{-1}]	507.5	502.4	499.1
x_0 ["]	0.42	-3.18	-5.17
y_0 ["]	0.05	5.81	3.77
i [$^\circ$]	55.33	57.28	61.07
PA [$^\circ$]	299.21	302.61	305.79

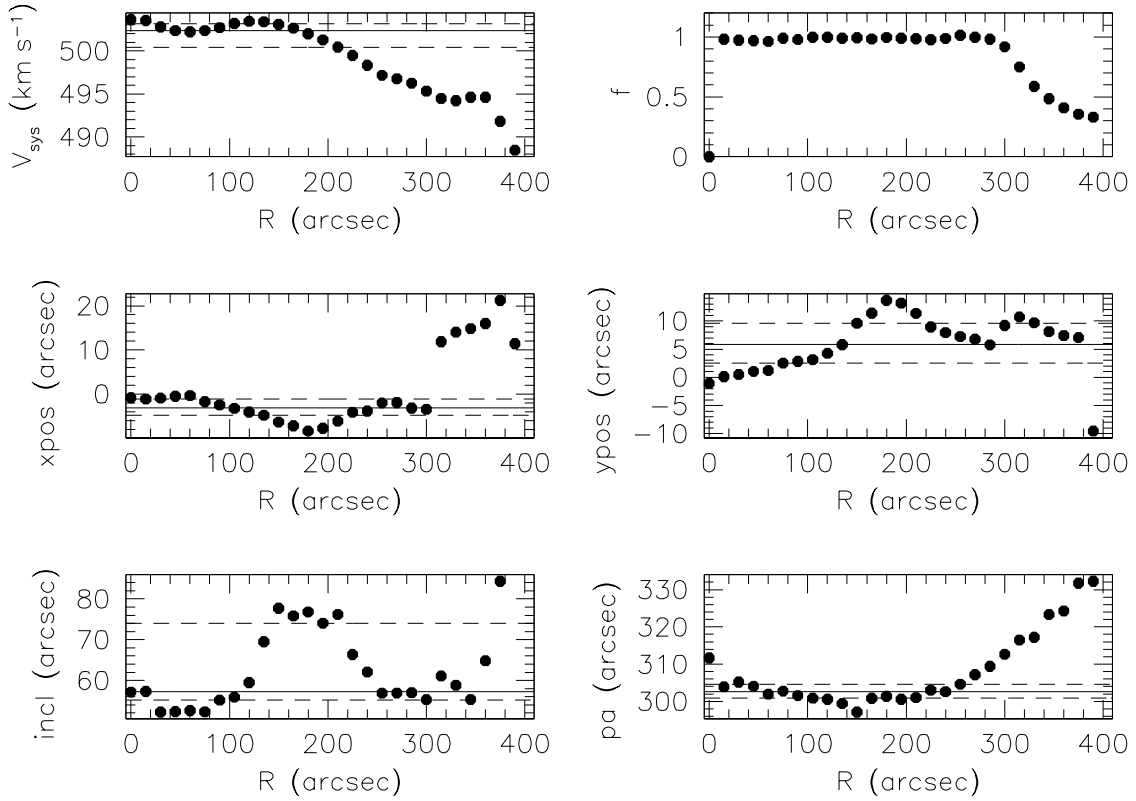


FIG. C.1: Deriving the rotation curve of NGC 5408: The iterative approach. All parameters are fitted against the radius of the rings. **Upper left:** v_{sys} . **Upper right:** Filling factor f . **Middle:** Centre position in x (left) and y (right). **Lower left:** Inclination. **Lower right:** Position angle. The solid line represents the median of each parameter, the dashed lines give the 25% and 75% levels.

approach: the best-fitting parameters from the HI rotation curve (iterative approach) were taken and kept fixed while deriving the rotation curve from the Fabry-Perot H α velocity field. In the cases of IC 4662 and NGC 5408, a rotation curve was estimated from the long-slit spectra and corrected for inclination.

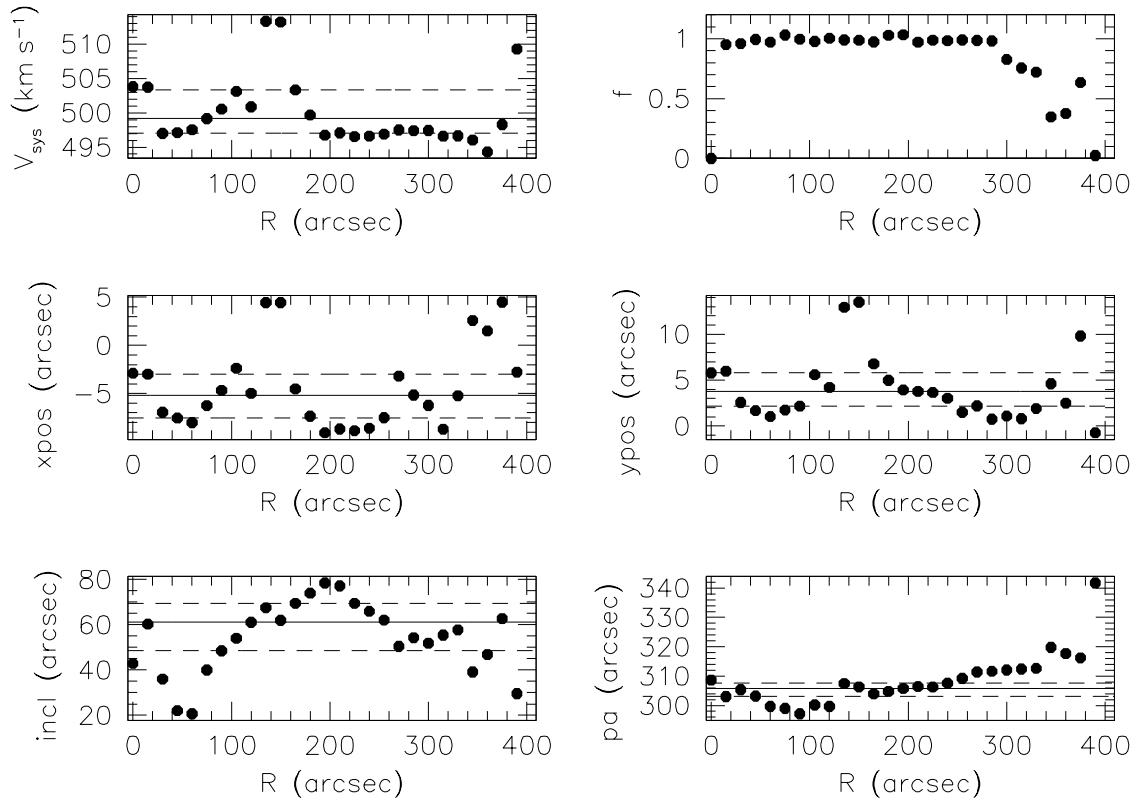


FIG. C.2: Deriving the rotation curve of NGC 5408: The free approach. The same as in Fig. C.1. The best-fitting parameters from the iterative approach were taken as initial estimates and kept free.

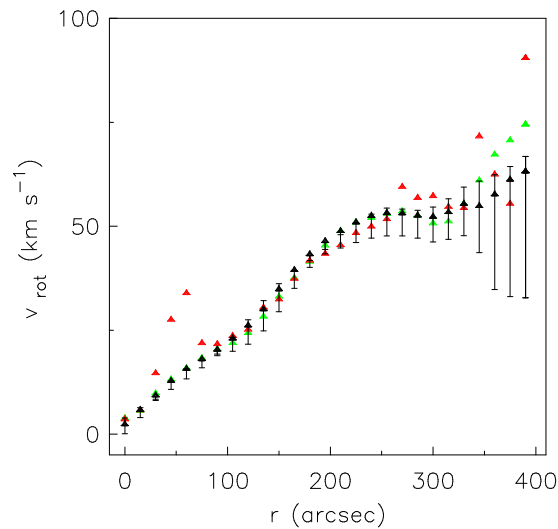


FIG. C.3: The resulting H I rotation curves of NGC 5408 created by fitting a tilted-ring model to the original H I velocity field. Different approaches for deriving the rotation curve are shown. The black symbols represent the iterative approach, the error bars indicate receding and approaching side. The green curve was derived by using the fixed approach, the red curve by using the free approach.

Bibliography

- Barazza, F. D., Binggeli, B., & Jerjen, H. 2002, *A&A*, 391, 823
- Begum, A., Chengalur, J. N., Karachentsev, I. D., Kaisin, S. S., & Sharina, M. E. 2006, *MNRAS*, 365, 1220
- Bekki, K., Koribalski, B. S., & Kilborn, V. A. 2005, *MNRAS*, 363, L21
- Bienayme, O., Robin, A. C., & Creze, M. 1987, *A&A*, 180, 94
- Binney, J. & Tremaine, S. 1987, *Galactic dynamics* (Princeton, NJ, Princeton University Press, 1987, 747 p.)
- Birk, G. T., Lesch, H., & Neukirch, T. 1998, *MNRAS*, 296, 165
- Bohuski, T. J., Burbidge, E. M., Burbidge, G. R., & Smith, M. G. 1972, *ApJ*, 175, 329
- Bomans, D. J. 2001, *ApSS*, 276, 783
- Bomans, D. J. 2005, in *AIP Conf. Proc. 783: The Evolution of Starbursts*, 98
- Bomans, D. J., Chu, Y., & Hopp, U. 1997, *AJ*, 113, 1678
- Born, M. & Wolf, E. 2000, *The Observatory*, 120, 149
- Bosma, A. 1978, PhD thesis, PhD Thesis, Groningen Univ., (1978)
- Braun, J. M., Bomans, D. J., Will, J.-M., & de Boer, K. S. 1997, *A&A*, 328, 167
- Chu, Y. & Kennicutt, R. C. 1994, *ApJ*, 425, 720
- Condon, J. J. 1992, *ARA&A*, 30, 575
- de Blok, W. J. G. 2004, in *IAU Symposium, Vol. 220, Dark Matter in Galaxies*, ed. S. Ryder, D. Pisano, M. Walker, & K. Freeman, 69
- de Blok, W. J. G. & Bosma, A. 2002, *A&A*, 385, 816
- de Blok, W. J. G., Bosma, A., & McGaugh, S. 2003, *MNRAS*, 340, 657

- de Blok, W. J. G., Walter, F., Brinks, E., Thornley, M. D., & Kennicutt, Jr., R. C. 2005, in *Astronomical Society of the Pacific Conference Series*, Vol. 329, *Nearby Large-Scale Structures and the Zone of Avoidance*, ed. A. P. Fairall & P. A. Woudt, 265
- de Vaucouleurs, G. 1975, *Nearby Groups of Galaxies (Galaxies and the Universe)*, 557
- de Vaucouleurs, G., de Vaucouleurs, A., Corwin, H. G., et al. 1991, *Third Reference Catalogue of Bright Galaxies (Volume 1-3, XII, 2069 pp. 7 figs.. Springer-Verlag Berlin Heidelberg New York)*
- Dettmar, R. J. 1992, *Fundamentals of Cosmic Physics*, 15, 143
- Drissen, L., Crowther, P. A., Smith, L. J., et al. 2001, *ApJ*, 546, 484
- Drissen, L., Roy, J.-R., Robert, C., Devost, D., & Doyon, R. 2000, *AJ*, 119, 688
- Elmegreen, B. G. & Efremov, Y. N. 1996, *ApJ*, 466, 802
- Elmegreen, B. G., Elmegreen, D. M., Salzer, J. J., & Mann, H. 1996, *ApJ*, 467, 579
- Elwert, T. & Dettmar, R.-J. 2005, *ApJ*, 632, 277
- Ferguson, H. C. & Sandage, A. 1991, *AJ*, 101, 765
- Gach, J.-L., Hernandez, O., Boulesteix, J., et al. 2002, *PASP*, 114, 1043
- Gallagher, J. S. & Hunter, D. A. 1984, *ARA&A*, 22, 37
- Gentile, G., Burkert, A., Salucci, P., Klein, U., & Walter, F. 2005, *ApJ*, 634, L145
- Georgelin, Y. P. 1970, *A&A*, 9, 441
- Gil de Paz, A., Boissier, S., Madore, B. F., et al. 2006, *ArXiv Astrophysics e-prints*
- Gil de Paz, A. & Madore, B. F. 2005, *ApJS*, 156, 345
- Graham, A. W., Jerjen, H., & Guzmán, R. 2003, *AJ*, 126, 1787
- Haar, A. 1910, *Math. Ann.*, 69, 331
- Haarsma, D. B., Partridge, R. B., Windhorst, R. A., & Richards, E. A. 2000, *ApJ*, 544, 641
- Helou, G., Soifer, B. T., & Rowan-Robinson, M. 1985, *ApJ*, 298, L7
- Hidalgo-Gómez, A. M., Masegosa, J., & Olofsson, K. 2001, *A&A*, 376, 386
- Hodge, P., Strobel, N. V., & Kennicutt, R. C. 1994, *PASP*, 106, 309
- Hunter, D. A. & Elmegreen, B. G. 2006, *ApJS*, 162, 49
- Hunter, D. A., Elmegreen, B. G., & van Woerden, H. 2001, *ApJ*, 556, 773
- Hunter, D. A. & Gallagher, J. S. 1997, *ApJ*, 475, 65
- Hunter, D. A., Hawley, W. N., & Gallagher, J. S. 1993, *AJ*, 106, 1797
- Jerjen, H., Kalnajs, A., & Binggeli, B. 2000, *A&A*, 358, 845

- Kaiser, N. 1991, *ApJ*, 383, 104
- Karachentsev, I. D., Dolphin, A., Tully, R. B., et al. 2006, *AJ*, 131, 1361
- Karachentsev, I. D., Karachentseva, V. E., Huchtmeier, W. K., & Makarov, D. I. 2004, *AJ*, 127, 2031
- Karachentsev, I. D., Sharina, M. E., Dolphin, A. E., et al. 2002, *A&A*, 385, 21
- Kennicutt, Jr., R. C. 1998, *ARA&A*, 36, 189
- Koribalski, B. S., Staveley-Smith, L., Kilborn, V. A., et al. 2004, *AJ*, 128, 16
- Kuzio de Naray, R., McGaugh, S. S., & de Blok, W. J. G. 2008, *ApJ*, 676, 920
- Lauberts, A. & Valentijn, E. A. 1989, *The surface photometry catalogue of the ESO-Uppsala galaxies* (Garching: European Southern Observatory, [c1989])
- Leroy, A., Bolatto, A. D., Simon, J. D., & Blitz, L. 2005, *ApJ*, 625, 763
- Łokas, E. L. & Mamon, G. A. 2003, *MNRAS*, 343, 401
- Mac Low, M. & Ferrara, A. 1999, *ApJ*, 513, 142
- Martin, C. L. 1998, *ApJ*, 506, 222
- McGaugh, S. S. 2005, *ApJ*, 632, 859
- Minchin, R., Davies, J., Disney, M., et al. 2005, *ApJ*, 622, L21
- Moore, B., Governato, F., Quinn, T., Stadel, J., & Lake, G. 1998, *ApJ*, 499, L5
- Moore, B., Quinn, T., Governato, F., Stadel, J., & Lake, G. 1999, *MNRAS*, 310, 1147
- Nail, V. M. & Shapley, H. 1953, *AJ*, 58, 45
- Navarro, J. F., Frenk, C. S., & White, S. D. M. 1996, *ApJ*, 462, 563
- Nilson, P. 1973, *Uppsala general catalogue of galaxies* (*Acta Universitatis Upsaliensis. Nova Acta Regiae Societatis Scientiarum Upsaliensis - Uppsala Astronomiska Observatoriums Annaler*, Uppsala: Astronomiska Observatorium, 1973)
- Noeske, K. G., Papaderos, P., Cairós, L. M., & Fricke, K. J. 2003, *A&A*, 410, 481
- Norman, C. A. & Ikeuchi, S. 1989, *ApJ*, 345, 372
- Oort, J. H. 1932, *Bull. Astron. Inst. Netherlands*, 6, 249
- Ponman, T. J., Cannon, D. B., & Navarro, J. F. 1999, *Nature*, 397, 135
- Portinari, L., Sommer-Larsen, J., & Tantalo, R. 2004, *MNRAS*, 347, 691
- Richter, G. M. 1978, *Astronomische Nachrichten*, 299, 283
- Richter, G. M., Lorenz, H., Bohm, P., & Priebe, A. 1991, *Astronomische Nachrichten*, 312, 345
- Roberts, W. W. 1969, *ApJ*, 158, 123

- Rood, H. J., Page, T. L., Kintner, E. C., & King, I. R. 1972, *ApJ*, 175, 627
- Roy, J., Boulesteix, J., Joncas, G., & Grundseth, B. 1991, *ApJ*, 367, 141
- Rubin, V. C., Thonnard, N., & Ford, Jr., W. K. 1978, *ApJ*, 225, L107
- Salucci, P. 2001, *MNRAS*, 320, L1
- Sanders, D. B. & Mirabel, I. F. 1996, *ARA&A*, 34, 749
- Schombert, J. M., Pildis, R. A., Eder, J. A., & Oemler, A. J. 1995, *AJ*, 110, 2067
- Shapiro, P. R. & Field, G. B. 1976, *ApJ*, 205, 762
- Slavin, J. D., Shull, J. M., & Begelman, M. C. 1993, *ApJ*, 407, 83
- Spano, M., Marcelin, M., Amram, P., et al. 2008, *MNRAS*, 383, 297
- Spergel, D. N., Bean, R., Doré, O., et al. 2007, *ApJS*, 170, 377
- Spergel, D. N., Verde, L., Peiris, H. V., et al. 2003, *ApJS*, 148, 175
- Springel, V., White, S. D. M., Jenkins, A., et al. 2005, *Nature*, 435, 629
- Stobbart, A.-M., Roberts, T. P., & Wilms, J. 2006, *MNRAS*, 368, 397
- Swaters, R. A., Madore, B. F., van den Bosch, F. C., & Balcells, M. 2003, *ApJ*, 583, 732
- Taylor, C., Brinks, E., & Skillman, E. D. 1993, *AJ*, 105, 128
- Taylor, C. L., Brinks, E., Grashuis, R. M., & Skillman, E. D. 1995, *ApJS*, 99, 427
- Taylor, C. L., Kobulnicky, H. A., & Skillman, E. D. 1998, *AJ*, 116, 2746
- Thuan, T. X., Hibbard, J. E., & Lévrier, F. 2004, *AJ*, 128, 617
- Tikhonov, N. A. & Galazutdinova, O. A. 2008, *Astronomy Reports*, 52, 19
- Tolstoy, E., Saha, A., Hoessel, J. G., & McQuade, K. 1995, *AJ*, 110, 1640
- Trachternach, C., de Blok, W. J. G., Brinks, E., Walter, F., & Kennicutt, Jr., R. C. 2008a, submitted to *AJ*
- Trachternach, C., de Blok, W. J. G., McGaugh, S. S., van der Hulst, J. M., & Dettmar, R.-J. 2008b, submitted to *A & A*
- van den Bosch, F. C., Robertson, B. E., Dalcanton, J. J., & de Blok, W. J. G. 2000, *AJ*, 119, 1579
- van Eymeren, J., Bomans, D. J., Weis, K., & Dettmar, R.-J. 2007, *A&A*, 474, 67
- Walter, F. & Brinks, E. 1999, *AJ*, 118, 273
- Walter, F., Brinks, E., de Blok, W. J. G., et al. 2008, submitted to *AJ*
- Walter, F., Brinks, E., de Blok, W. J. G., Thornley, M. D., & Kennicutt, R. C. 2005, in *Astronomical Society of the Pacific Conference Series*, Vol. 331, *Extra-Planar Gas*, ed. R. Braun, 269

Wilcots, E. M., Lehman, C., & Miller, B. 1996, *AJ*, 111, 1575

Wilcots, E. M. & Thurow, J. C. 2001, *ApJ*, 555, 758

Zwicky, F. 1933, *Helvetica Physica Acta*, 6, 110

Zwicky, F. 1937, *ApJ*, 86, 217

Acknowledgements

A PhD thesis is seldom the product of the author alone, but is supported in many different ways by many different people. Therefore, I would like to take the chance to thank the most important persons who were involved into my work at some points.

First of all, I would like to thank my supervisor and referee Ralf-Jürgen Dettmar who gave me the opportunity of writing my thesis at his institute. I also appreciate the support I got from my other two referees and co-supervisors, Dominik Bomans and Bärbel Koribalski.

Furthermore, I am very grateful for the wonderful collaboration I had with Bärbel Koribalski, Michel Marcelin, and Eric Wilcots. Bärbel, thanks a lot for inviting me to Sydney, for introducing me to radio astronomy, for giving me the chance to be a member of the LVHIS team, and for always motivating me. Michel, you invited me for a research stay to Marseille. Thanks a lot for introducing me to Fabry-Perot interferometry and for always being present when I needed your help. Eric, thanks for inviting me to Madison, for providing parts of the radio and optical data of NGC 4861, and for the scientific discussions we had. The H I data cube of NGC 2366 is part of the THINGS survey and was given to me in a fully-reduced version by Fabian Walter. Thanks for that, Fabian. In this context, I would also like to thank another member of the THINGS team, Erwin de Blok, who helped me with the mass decomposition.

Thanks to two other members of the LVHIS team, Ángel R. López-Sánchez and Nic Bonne, on the one hand for their scientific help and on the other hand also for the good companionship. My stays in Sydney would have been less fun if you two and Urvashi Rau (in 2006) and Carmen Sánchez-Gil (in 2007) have not been there. Thank you all for the nice weekends and evenings we spent together in Australia. Thanks also to all the people at the ATNF who made my two stays even more comfortable and enjoyable. A special thanks goes to you, Carmen, for inviting me to Granada, for showing me the best tapas, and for the Flamenco dance class.

What should have come first is a big “THANK YOU” to the Hoher List team, Nicola Bennert, Daniel Brown, Christian Leipski, and Olaf Schmithüsen. You gave me the feeling that astronomy is something special and exciting and needs to be studied. I also thank the other members of the AIRUB, especially Olaf Schmithüsen and Tim Falkenbach who helped me with computer or network problems. It was a pleasure to be a colleague of Giuseppe Aronica. Thank you, Giuseppe, for the numerous discussions we had and thanks for correcting parts of my thesis. Finally, I thank my best colleague of all, Clemens Trachternach, for his scientific support, but especially for being a good friend.

Sometimes, you need someone to talk to who works in a completely different area, but has experienced the same things. Therefore, I would like to thank my mentor, Silke Plumanns, who always gave me new motivation for my work.

Last but not least, I express my deepest gratitude to Jan Förster, my companion in life, who supported my numerous travels with the consequence of me being not at home for weeks or sometimes even for months, and always endured my bad moods if something did not work the way I wanted it to work. I love you!

Technical Acknowledgements

This work was partly supported by the Deutsche Forschungsgesellschaft (DFG) under the SFB 591, by the Research School of the Ruhr-Universität Bochum, by the Australia Telescope National Facility, CSIRO, and by the DAAD.

It is partly based on observations collected at the Centro Astronómico Hispano Alemán (CAHA) at Calar Alto, operated jointly by the Max-Planck Institut für Astronomie and the Instituto de Astrofísica de Andalucía (CSIC).

It is also partly based on observations collected at the Observatoire de Haute-Provence.

A different part is based on observations collected at the European Southern Observatory, Chile. Proposal-No.:077B.-0115(A)

It is also partly based on archival VLA data of the National Radio Astronomy Observatory. The NRAO is a facility of the National Science Foundation operated under cooperative agreement by Associated Universities, Inc.

Finally, it is partly based on observations with the Australia Telescope Compact Array. The ATCA is part of the Australia Telescope which is funded by the Commonwealth of Australia for operation as a National Facility managed by CSIRO.

This research has made use of NASA's Astrophysics Data System (ADS) Bibliographic Services and the NASA/IPAC Extragalactic Database (NED) which is operated by the Jet Propulsion Laboratory, California Institute of Technology, under contract with the National Aeronautics and Space Administration.

Curriculum Vitae

Personal Details

Name: Janine van Eymeren
Address: Schadowstr. 10
45147 Essen
Date/Place of birth: 07.10.1979 in Essen
Nationality: German

Education

1986-1990 Graf-Spee-Schule, Essen
1990-1999 Goetheschule, Essen
degree: Allgemeine Hochschulreife (university entrance qualification)
10/1999-12/2004 Study of Physics at the Ruhr-Universitaet Bochum
10/2003-09/2004 Diploma thesis at the Astronomisches Institut der Ruhr-Universitaet Bochum (AIRUB)
Title: Structure and Kinematics of Gas Filaments in Irregular Dwarf Galaxies
12/2004 Diploma in Physics, degree: 1 (very good)
since 03/2005 PhD thesis at the AIRUB
Title: Gas Kinematics in the Haloes of Nearby Irregular Dwarf Galaxies

Positions

09/2003-12/2004 Scientific assistant at the AIRUB
Coordination of the Graduate School 787
since 02/2005 Scientific staff member at the AIRUB

